STRUCTURAL IMPLICATIONS FOR OXYGEN ELECTROCATALYSIS IN EARTH-ABUNDANT TRANSITION METAL OXIDES

By

GRAEME PATRICK GARDNER

A dissertation submitted to the

Graduate School-New Brunswick

Rutgers, The State University of New Jersey

In partial fulfillment of the requirements

For the degree of

Doctor of Philosophy

Graduate Program in Chemistry and Chemical Biology

Written under the direction of

G. Charles Dismukes

And approved by

_____

_____

_____

_____

New Brunswick, NJ

OCTOBER, 2016

ABSTRACT FOR DISSERTATION:

"Structural Implications for Oxygen Electrocatalysis in Earth-Abundant Transition Metal Oxides"

By GRAEME PATRICK GARDNER

Dissertation Director:

Professor G. Charles Dismukes

Transition metal oxides and related nitrides/nitride-oxides represent a class of materials that have shown great promise as oxygen electrocatalysts to replace the otherwise non-scalable noble metal-based catalysts currently implemented in commercial technologies. That is, compounds in this class of materials have shown promise as electrocatalysts for both the oxygen evolution (OER) and oxygen reduction reactions (ORR). The two aforementioned half-reactions are at the cornerstone of most renewable energy transformations, as oxygen is an inherently practical and abundant source and sink for electrons. In water electrolysis to produce hydrogen, oxygen is inevitably formed, and in a fuel cell the driving force for extracting electrochemical energy from hydrogen is pairing it with the reduction of oxygen to water. If this can be accomplished reversibly, the problem of "transient" renewable energy and its storage can be mitigated.

We have examined many metal oxides and related compounds based upon Earth-abundant transition metals (primarily first row) that are crystalline, yet high surface area, for these important electrocatalytic reactions, and found that crystal structure plays a crucial role in determining activity. In fact, while most studies on heterogeneous catalysis focus on the synthesis of defect-rich, high surface area, practically amorphous materials

to elicit high activity, we have found that particular crystalline phases possess not only the appropriate activity, but to some degree more importantly, the stability to be named good catalysts.

In Chapter 2, we demonstrate that of the two structural types of lithium cobalt oxide ($LiCoO_2$) – layered (R-3m) and cubic (Fd-3m) – only the cubic phase is revealed to be an efficient and stable catalyst for OER. Whether water oxidation is driven photochemically, or electrochemically, the cubic phase $LiCoO_2$ possessing a spinel-like structure (AB_2O_4) with $[Co_4O_4]$ subunits within the crystal is more active. It is seen that electrochemically, both the cubic and layered phases transform to the spinel $LiCo_2O_4$ at surface and subsurface levels. This coincides with partial delithiation that is more extensive in layered $LiCoO_2$. It is revealed that the oxidation of Co^{3+} to Co^{4+} is accompanied by delithiation in aqueous electrolyte to form the active state of the $LiCoO_2$ catalyst. The electronic properties of the cubic spinel allow for localization of electron holes at cubic core active sites to effect water oxidation, whereas holes are more extensively delocalized in layered $LiCoO_2$ in concert with the Li^+ deintercalation reaction.

In Chapter 3, we investigate the influence of chemical composition on the catalytic water oxidation activity of Co-substituted spinel $LiMn_2O_4$ and Mn-substituted cubic $LiCoO_2$. We find that in the spinel $LiMn_2O_4$, Co^{3+} substitution occurs at the B-site for Mn^{3+}, and the solid solution limit for starts at 1:1 Co:Mn ratio, where Co begins to go into the A-site. The activity for OER increases with increasing Co, owing to the symmetrization of the M_4O_4 core structure (Jahn-Teller distortions suppressed), which allows for hole delocalization that enables $Co^{3+/4+}$ oxidation. The more positive redox

potential of Co^{4+} makes for facile water oxidation. Substituting Mn for Co in cubic $LiCoO_2$ allows for retention of Mn^{3+}, which has been correlated with water oxidation activity in many catalysts. The solid solution limit in this series is also near 1:1 at the B-site. However, the increase in Mn content corresponds to decreasing activity in both water oxidation and oxygen reduction, which correlates well with decreases in pre-catalytic oxidation and reduction peak yields. The results show replacement of Co^{3+} with Mn^{3+} effectively eliminates active sites. Therefore, Mn^{3+} in this electronic and structural environment is not active, which agrees well with a recent literature report on corner-shared Mn^{3+} octahedral being necessary to produce OER activity in Mn oxides.

Finally, in chapter 4, bifunctional oxygen electrocatalysts are explored in depth with a series of cobalt-molybdenum oxides/nitrides. We demonstrate that $CoMoN_2$, with relatively strong M-N interactions, has ideal electronic properties for ORR, and upon oxidation of the surface, yields an active OER catalyst. However, the surface oxidation is found to be irreversible and once oxidized, the activity for ORR significantly decreases. The surface both before and after catalysis was analyzed by XPS, which showed the suppression of Mo and N signals after exposure to OER conditions, meaning the active catalyst is a Co oxide of high valency (3/4+). The results from this study suggests truly reversible, bifunctional oxygen electrocatalysis may be obtained by designing a catalyst whose surface is only partly oxidized and/or can be reversibly reduced in the potential window relevant to OER and ORR.

Dedication

For my Mother, Kim

Acknowledgements:

This thesis contains the work behind the following publications (in whole or part)

1. Gardner, Graeme P.; Go, Yong Bok; Robinson, David M.; Smith, Paul F.; Hadermann, Joke; Abakumov, A.; Greenblatt, Martha; Dismukes, G. Charles, "Structural Requirements in Lithium Cobalt Oxides for the Catalytic Oxidation of Water". *Angewandte Chemie International Edition*, 2012, 51, 1616-1619.

2. Gardner, Graeme; Al-Sharab, Jafar; Danilovic, Nemanja; Go, Yong Bok; Ayers, Katherine; Greenblatt, Martha; Dismukes, G. Charles, "Structural Basis for differing electrocatalytic water oxidation by the cubic, layered and spinel forms of lithium cobalt oxides". *Energy and Environmental Science*, 2015, 9, 184-192.

3. Cady, Clyde W.; Gardner, Graeme; Maron, Z.M.; Retuerto, M.; Go, Y.B.; Segan, S.; Greenblatt, M.; Dismukes, G.C. "Tuning the Electrocatalytic Water Oxidation Properties of AB_2O_4 Spinel Nanocrystals: A (Li, Mg, Zn) and B (Mn, Co) Site Variants of $LiMn_2O_4$". *ACS Catalysis*, 2015, 5, 3403-3410.

4. Gardner, Graeme; Hwang, Shinjae; Porter, Spencer; Greenblatt, Martha; Dismukes, G. Charles, "Cobalt Molybdenum Nitride as Bifunctional Oxygen Electrocatalyst: Role of Nitride in Catalyst Activity and Stability", *in prep.*

First and Foremost, I would like to acknowledge my advisor, Professor G. Charles Dismukes (Chuck), for about as many reasons as anyone could think. He has provided intellectual support, mentorship, friendship, financial support, and scientific motivation. I say scientific motivation because of his ability to make his students/post docs/colleagues think about their science in new ways, focusing on hypothesis-driven research ideas and making sound scientific conclusions. In addition, he pushes his students to always be sharing their work, at any level, with the greater research community – conferences, symposia, group meeting presentations. Working in his lab has given me immense experience with presenting our science to others. Without his advisement, I do not know how I would have fared as a scientist.

Secondly, I could not have conducted a very fruitful graduate career without the advisement of Professor Martha Greenblatt. She has an unmatched expertise in solid-state chemistry, and an unmatched intellect and personality that one cannot help but admire. Her advice and consultation has helped myself and countless others in the Dismukes' group grow as scientists, and our ability to operate successfully in the field of heterogeneous catalysis would not be possible without her.

In the process of obtaining a PhD, the educational environment is of critical importance in shaping future scientists. I had the pleasure of a being in a very collaborative and talented educational garden. I have to thank the research scientists around me – Dr. Gennady Ananyev, Dr. John Sheats, Dr. Tom Emge, and Dr. Jafar Al-Sharab. I have to thank post-doc fellows Dr. Clyde Cady, Dr. Maria Retuerto, Dr. Kenchappa Kumaraswamy (Kumar) and Dr. Spencer Porter. I would like to thank in particular two post docs I have had the pleasure of working with. Dr. Anders Laursen has been my teacher as much as he has been a colleague, and Dr. Yong Bok Go has been a guiding light for me in chemistry and has become a dear friend. My early days in the lab would not have been as easy had he not been open and willing to work with me.

My fellow graduate students and undergraduate lab-mates deserve a lot of credit. They were not only the colleagues I shared my learning experience with, they became my friends as well. There are perhaps too many to name, but I will try to list as many as I can: David Robinson, Bin Liu, Nick Skizim, Nick McCool, Chris Kaplan, Zach Maron, Yifan Wang, David Vinyard, Tiago Guerra, Anagha Krishnan, Xiao Qian, Colin Gates, Karin Calvinho, Shinjae Hwang, Jessia Gonzalez, Monica Navarreto.

I have to give special thanks to my dear friend and colleague Paul Smith, who a served as a sort of complement to me in the Dismukes group for the entirety of my graduate career. It has been an absolute joy sharing this experience with him, and I hope he learned as much from me as I have from him. It is a truly interesting thing to see the development of a mature scientist while one is maturing himself. I am very appreciative of the differences between the two of us, and I believe that served us well as collaborators, rather than detract in any way. I wish him the best, and I believe he will make for a spectacular scientist in whatever pursuit he chooses.

Finally, I would like to thank my family. I believe in putting family above all else in life, and my family truly makes it worth it. Josh, Meg, Bill, Tara, Jack, Derek, Andrew, Jeanmarie, Jamie, Chuck, Grandma Pat, Grandma Gardner, and the many dozens of others that make up our beautiful family. Thank You.

Table of Contents

List of Tables

List of Figures

Chapter 1

1. Introduction and Background

1.1 Energy Crisis

It is often stated that the world is in the midst of a serious crossroads that involves the choice to address a crisis of proportions that civilization(s) have not yet faced. That crisis is one that involves energy, both in the context of what the term used to mean – i.e. access to food – and one that has been specifically ushered in because of the industrialization and globalization of our society. We have an *internal* energy crisis, where more than $1/10^{th}$ of the world's population is starving or malnourished(*1*), and we are facing a serious *external* energy crisis, where the foundation for our society's enormous growth is the use of an energy source that is finite, polluting, and leading to serious international conflicts(*2*). The energy resources in forms outside of our own bodies are being consumed at a rate that by any account does not seem sustainable, and the consumption of said resources is leading to a destruction of the environment in which humans need to maintain to survive. Global catastrophic events related to increasing atmospheric CO_2, and subsequently rising temperatures are already becoming apparent. A recent report from Scientists at Rutgers has verified that indeed global sea-level rise in the last century can be attributed to climate change, and we should probably be expecting another 4 feet by the end of this century(*3*), something that will drown some island nations, and modify coastlines of developed countries causing severe economic disasters. Coral reef decline in the Great Barrier Reef has extended to 50% of its original cover, an effect that owes much of the blame to climate change(*4*), which damages a market with an economic value estimated at close to $6 billion(*5*). Finally, increasing droughts in

places normally thought of as agricultural havens spell disaster for both residents and farms. California's recent drought problems – although tenuously linked to overall climate change – have totaled a $2.7 billion economic loss(*6*). The consequences of climate change are upon us and no longer a skeptical prediction. At the same time, there are drastic disparities in terms of means and opportunity in the United States, and the world, which, if addressed, would mean an even larger energetic demand possibly leading to heightened CO_2 emissions compared to the base case, thus the origin of the 30 TW by 2050 challenge(*7*–*9*).

The scale of the world's energy crisis is often overlooked because fossil fuels have been so far available in such large quantities, relatively easy-to-use forms, and at hugely discounted rates, as the governments of any powerful developed country will subsidize energy. In order to solve these problems, a diverse portfolio of new energy technologies and sound political policies(*10*) needs rolling out, as there will not be any one-size fits all solution. In addition, there needs to be a shift from policy-making purely based upon energy security, affordability, and job creation, to policies that in particular target global climate change, as the first 3 can clearly be captured using domestic fossil fuel resources (which only seem to be getting more abundant)(*11*, *12*). Indeed, when the world's leading religious institution hosts a climate change summit(*13*) aimed at influencing policy-making in countries where the discussion on its validity is still being questioned, there seems to be something wrong. Renewable energy solutions are necessary to combat these problems and to shed light on a gray future, which is what motivates us scientists to toil away in the fields that we do.

In the following sections, I will give a brief introduction to some of the basic fundamentals behind one possible solution in a renewable energy future, namely the use of hydrogen (H_2) as an energy carrier to store, transport, and utilize forms of energy that may otherwise be transient and localized (solar, wind, etc…). A brief background on photosynthesis, both natural and artificial will be presented to give context to the work in the chapters that follow. Finally, a more specific introduction to the materials that are utilized for the purposes of energy conversion in electrolyzers, fuel cells, and lithium ion batteries will be presented.

1.2 The Hydrogen Economy and Water Splitting

1.2.1 Why Hydrogen?

The Director for R&D for General has been quoted saying the following: "General Motors absolutely sees the long-term future of the world being based upon a hydrogen economy." CEO's and top leaders in businesses ranging from energy to computer technology have been known to issue similar statements. We are at the precipice of a very technology-driven era, and the elegant simplicity of a closed fuel cycle (involving water, oxygen, and hydrogen) is incredibly enticing, even being dubbed one of the "Holy Grails" of chemistry(*14*).

Most scientists now realize and many have reiterated over decades that a path to a sustainable renewable energy future must involve electricity storage from renewables in chemical bonds, the most readily accessible being hydrogen(*15–17*). Other forms of alternative energy generation/storage to replace fossil fuels have their advantages, and have been absolutely necessary in the short-term (dams, nuclear power, biomass,

batteries), but the energy density capable of being stored and released through chemical bonds (hydrogen, 142 MJ/kg, methane 55 MJ/kg, Ni-Cd battery 0.3 MJ/kg) seems to be the undisputed winner for the future of our world. Currently, hydrogen is mostly being produced by steam reforming, with the end use mainly geared toward ammonia and methanol synthesis (via Haber-Bosch process), and industrial refining(*18*). The annual global production reaches close to 50 M metric tons worldwide(*19*), but if the total energy demand in were to met in 2050 (~30 TW) with hydrogen exclusively, production would need to be approximately 7,000 M metric tons per year, a deficit of 2 orders of magnitude without accounting for efficiency of combustion (or electrochemical efficiency in a fuel cell). In only counting the U.S. car fleet by that same time, we would still need on the order of 150 M metric tons, still 3x world production(*20*). The use of hydrogen to power fuel cells is not quite registering today as a significant consumption sector, but even if CO_2 emitting sources of H_2 like steam reforming of natural gas are used to create the hydrogen to run fuel cells, there is a significant deficit if the entirety of the U.S. auto fleet were to be fuel cell electric vehicles (FCEV's). If we are to cover the gap, even the purported endless supply of natural gas coming out of the ground now will not be enough. Thus, water splitting, coupled with renewable energy sources must be seriously considered for making up that difference(*17*, *19*, *20*), for reasons of scale and CO_2 emissions. However, it would be foolish to introduce the concept of water splitting without first going over some details on the natural inspiration for such a technology (that in a sense, involves no actual H_2 production whatsoever), and that is photosynthesis.

1.2.2 Photosynthesis, Natural Inspiration

Photosynthesis, the process by which cyanobacteria, algae, and plants convert carbon dioxide and water to energy rich organic molecules (sugars) and molecular oxygen, is predicated on a series of reactions catalyzed by enzymes designed to oxidize water (light-dependent reactions) and enzymes designed to take those high-energy electrons and protons to reduce carbon dioxide (carbon fixation, Calvin cycle). This process is the ultimate source of historically all sources of energy used by humans on earth, and the source of the most utilized form of energy currently, which are fossil fuels. Amazingly, the three most common forms of this type of energy, oil, coal, and gas, come from only a few types of organisms that lived in a (relatively speaking) small amount of time in planet's geologic history(*21*). The conditions to convert biomass into high-density fuel precursors as opposed to the normal decomposition are incredibly specific (geologically-speaking). In addition, the amount of energy in the form of fossil fuels that humans use in just one year ends up being greater than 2 orders of magnitude more than the net productivity of the planet's current biota(*22*).

Perhaps the most amazing fact is the fundamental components of photosynthesis likely evolved once over 2 billion years ago and have been conserved throughout all the oxygenic autotrophic organisms on the planet(*23*). It is kick-started by light-dependent reactions driven by the enzymes photosystem I and II embedded in thylakoid membranes. Photosystem two (PSII, because it was discovered after PSI), is the starting point in the electron transport chain that catalyzes the oxidation of water to dioxygen, in the meantime releasing protons into the lumen (interior space of thylakoid), and electrons that are key to the autotrophic processes needed to produce sugars to sustain the organism(*24*). The process is cyclic, and requires 4 single-turnover flashes,

corresponding to the 4 electrons taken from 2 waters (also 4 protons), to progress through the cycle of 5 "S-states" (the fourth of which being transient in combination with O_2 release)(*25*). The enzyme itself is extremely large (~500 kDa), and the bulk of the enzyme is supporting a network of light-harvesting molecules (chlorophylls) that can absorb light and can act as antennae that channel the energy to a "special pair" of chlorophylls (P_{680}) that can affect a charge separated state, perhaps the first p-n junction, where an electron and hole are separated from one another(*26*, *27*). The hole oxidizes a tyrosine Z to form a radical that will accept an electron from the water-oxidizing complex (WOC), and the electron travels through a series of intermediate states (reduce plastoquinone pool ➔ PSI), eventually reducing $NAD(P)^+$ to make the biological equivalent of H_2, NAD(P)H (**Figure 1.1**). The WOC, or oxygen-evolving complex (OEC), is a cluster of 4 manganese atoms and one calcium atom held in place by specific amino acid residues and linked together by various u-oxo type bridges. It is a spontaneously forming (under illumination) inorganic complex held in place by a special manganese binding protein(*28*). The specific structure has been a topic of immense debate, and the its precise unveiling has come from decades of incredible scientific research, using EPR spectroscopy(*29–31*), X-ray absorption techniques(*32*, *33*), and crystallography(*34–36*). It is now known definitively that the structure of the cluster is a heterocubane-like structure where 3 Mn and the one Ca form the central cube and the fourth Mn is dangling via a μ-oxo bridge through O4 and (partly) O5 (see **Figure 1.2a,b**). It is suggested that the unusual coordination environment around O5 make it likely one of the substrate binding sites(*24*, *37*).

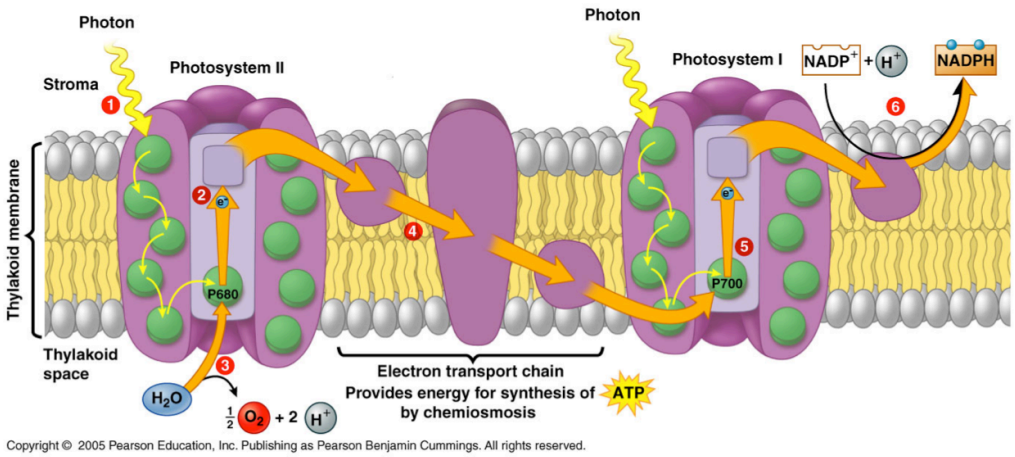

Figure 1.1 Light-dependent reactions of photosynthesis taking place in the thylakoid membrane of the cell. In PS II, (1) excitation of chlorophyll is channeled to P680 where (2) charge separation takes place to reduce the primary electron acceptor pheophytin along with (3) oxidation of the $CaMn_4O_5$ cluster, then (4) reduction of plastoquinone (PQ) pool. After (5) additional excitation and charge separation in PS I, the electron is used to (6) reduce $NAD(P)^+$. Figure is from Pearson Education, Copyright © 2005.

Capturing the essence of this enzyme, and more specifically the $CaMn_5O_x$ complex bound within it has been the ultimate goal of much of the research in water oxidation catalysis and artificial photosynthesis (AP) research in general(*38*). What makes the cluster so special that it can turnover (make 1 molecule of O_2) at a rate of 25-88s^{-1}(*24*)? How does it conduct efficient multi-electron redox chemistry at an overpotential of only ~300 mV(*39*)? In designing a biomimetic catalyst, or perhaps more appropriately, a bioinspired catalyst, it is often not possible to impart some of the extensive functionality that the bulk of the enzyme provides. Nature had 2.5 billion years to develop that. Indeed, the role of a single chloride atom located specifically more than 6 Å away from the Mn cluster seems to be crucial for turnover (**Figure 1.2b**), perhaps providing a distinct proton relay away from the core(*40*), but how do we accomplish that specific task in artificial systems? The manganese cluster also has quite sophisticated chemistry that does not just allow for someone to put calcium and manganese together in a molecule or oxide and produce an active catalyst(*41*, *42*). Finally, photosystem II is constructed actively in the cell and can be rebuilt, every 30 minutes if need be(*43*), to

keep the photosynthetic process stably chugging away. Is it possible to make a "self-healing" catalyst that can accomplish this task artificially(*44*)? The fundamental principles that have been elucidated thus far as key to the development of artificial catalysts will be discussed in context in the chapters on artificial heterogeneous water oxidation catalysts to follow.

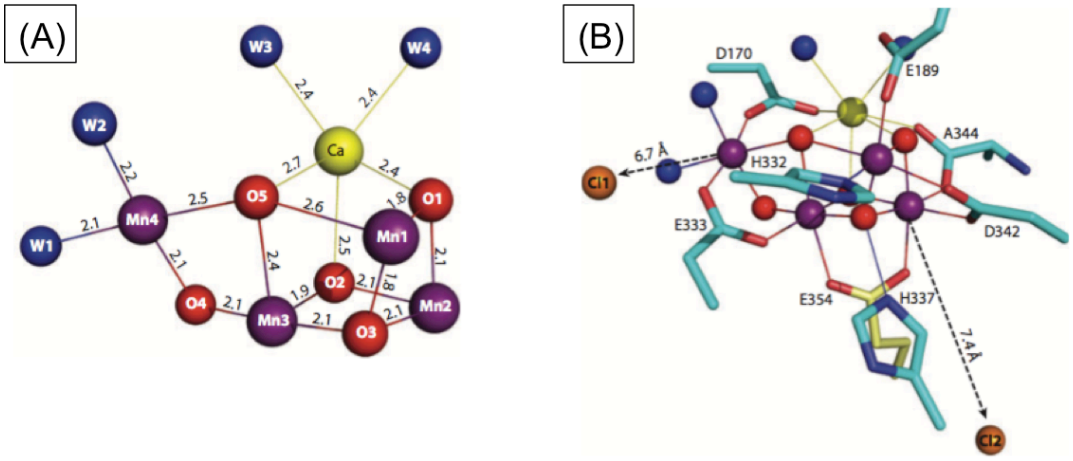

Figure 1.2 Crystal structure of the inorganic cluster of photosystem II from 1.9 Å resolution X-ray structure determined by Umena et al., reference (*35*). (a) Isolated core $CaMn_4O_5(H_2O)_4$ unit showing bond lengths and coordination geometry of oxo and aquo ligands in the S_1 state. (b) The first coordination sphere of amino acids bound to the water-oxidizing complex, along with the positions of the two Cl atoms near the cluster. Figure from Vinyard et al., reference (*24*).

1.3 Materials for Electrochemical Energy Storage

1.3.1 Materials for Lithium Ion Batteries

It would be prudent at this time to briefly introduce some of the concepts pertaining to lithium ion batteries (LIB) and the materials used for those applications, as many of the compounds discussed in the following chapters are used as the active component of LIB electrodes. Rechargeable LIB's have garnered serious attention in the research community over the past few decades with the rise of their commercial success, beginning in 1991 with the introduction of the first successful secondary (rechargeable)

battery from Sony(*45*). Prior to that point, there was a significant amount of work on primary batteries, such as those based upon silver vanadium oxide(*46*), and some work on the layered TiS_2 as a reversible cathode material(*47*), but the serious boom in research came when it was predicted and found that layered lithium cobalt oxide ($LiCoO_2$) could reversibly intercalate Li into the structure over multiple cycles without significant capacity loss(*48*, *49*).

Research in the LIB field has seen a heavy focus on developing materials for the cathode, where Li is extracted during the charging process, and is reintroduced during discharge (See **Figure 1.3a** for layout of battery). The most important properties to keep in mind for these compounds are the following: cell energy (voltage range which charge/discharge occurs), capacity (or total Li stored), and discharge rate (C, how fast can cell be charged or discharged reversibly within the voltage range) and specific energy (effectively the voltage X capacity).

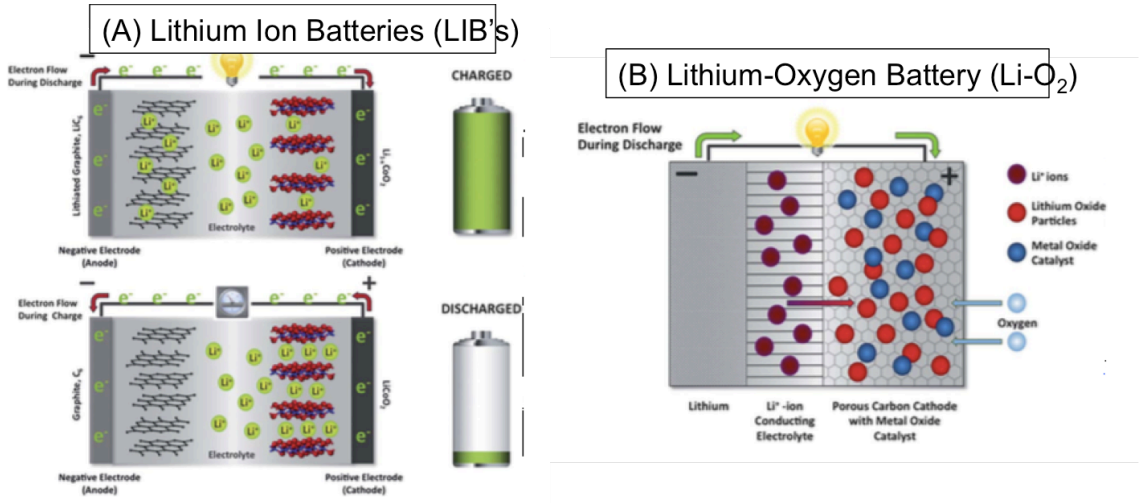

Figure 1.3 (a) Illustration of lithium ion battery (LIB) operation in (top) charge and (bottom) discharge modes. The Li ions are shuttled between the graphitic LiC_6 anode through non-aqueous electrolyte to the layered $LiMO_2$ cathode, which intercalates Li ions reversibly. (b) The lithium oxygen ($Li\text{-}O_2$) or air battery, in which Li^+ is combined with oxygen to form Li_2O or Li_2O_2 products at the cathode during discharge. Images from reference (*49*).

Interestingly enough, many of the properties that qualify materials as good compounds for use in LIB's also happen to be important when considering catalysts for water oxidation/oxygen reduction. The cell voltage is derived in part from the redox potential of the transition metal $M^{(n/n+1)}$(*50*), which also holds value as a descriptor for electrocatalyst activity, as discussed below. This is at the heart of the research on Li-O_2 batteries(*51*, *52*), which have the potential to bring the energy density of LIB's to the level needed for automotive applications (**Figure 1.3b**). Insomuch as the water splitting reaction is a "holy grail" of chemistry, so too has the lithium-oxygen battery system been considered in that research community, because of the enormous specific energy possible (1700-2600 Wh kg^{-1})(*49*). The crossover is not coincidental, as the reactions involved are closely related. The charging of Li-O_2 batteries involves oxygen evolution from deposits of either Li_2O or Li_2O_2 on the electrode surface formed during discharge. Improvements in cell capacity and reversibility have been made when adding electrocatalysts of like MnO_2, Mn_3O_4, and Co_3O_4, and other first-row transition metals/metal oxides to the cathode electrode which would otherwise be only carbon(*53–55*). The O_2 electrodes in these batteries have to be bifunctional, catalyzing both oxygen evolution and reduction. Therefore, many of the materials studied for Li-O_2 batteries are also promising candidates for unitized regenerative fuel cells (URFC) that operate both as electrolyzers and fuel cells reversibly in one system(*56–59*), which will be discussed more in chapter 4.

1.3.2 Electrolysis of Water

The electrocatalysis of water splitting is broken down to 2 half-reactions: the hydrogen evolution reaction (HER) and the oxygen evolution reation (OER). The

thermodynamic voltage required to split water is 1.23 V, normally requiring in excess of 1.8-2.2 V to drive the reaction at any meaningful rate (current). The origin for this excess voltage, or overpotential, is because the HER and OER have significant kinetic limitations, or activation barriers, meaning catalysts are necessary.

There are several configurations that are commercially available or technologically relevant for conducting water splitting to hydrogen and oxygen, basically breaking down into 3 major categories (for non-biological): electrolyzers(*60–62*), photoelectrochemical cells(*63*, *64*), and solar thermochemical cells(*65*, *66*). Since the studies presented in this thesis concern mostly catalysis 'in the dark' on nanoscopic powders, the relevant configuration to introduce in more detail is the water electrolyzer (**Figure 1.4**).

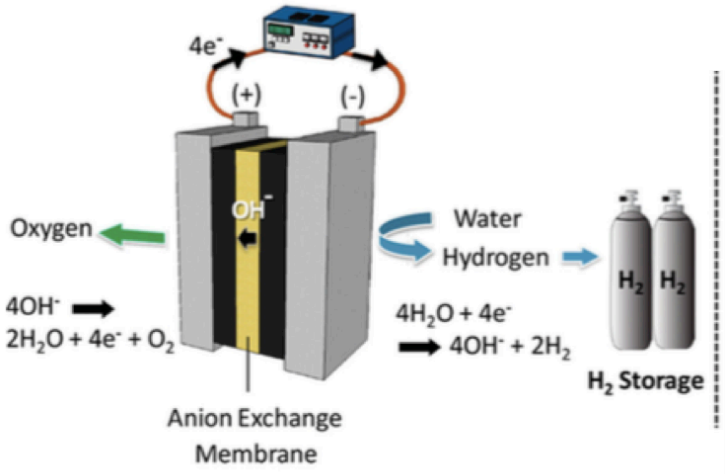

Figure 1.4 Schematic of an anion exchange membrane (AEM) electrolyzer, where O_2 is generated at the anode, H_2 at the cathode, and OH^- provides the ionic conduction through the membrane as opposed to H^+ in the standard PEM electrolyzer.

Different types of electrolyzers exist, with a wide range of appropriate applications, but the most relevant to introduce here is the membrane-based electrolyzer. The membrane-based water electrolyzer can function under acidic conditions, employing to a proton exchange membrane (PEMWE), or can utilize an anion (alkaline) exchange

membrane (AEMWE), where hydroxide serves as the ionic conuctor. The latter has been developed more recently, and holds great promise because it opens up the door for using less expensive corrosive-tolerant materials, and catalysts based upon Earth-abundant elements(*67*). It also opens the door for reversible fuel cells using only catalysts made from cheap, widely available elements(*68*).

Membrane-based electrolysis was heavily researched and developed initially for NASA's space program(*69*), providing ultra-pure oxygen to be used in the cabin's atmosphere, but was subsequently re-evaluated as an incredibly efficient (and low-temperature) way of producing hydrogen from water electrolysis with a focus on new applications (including renewable energy storage), with efficiencies for PEMWE reaching 80% (@ 1 A/cm^{-2})(*70*, *71*) today. AEMWE's lag behind that target(*72*, *73*), and much of the testing has been performed on noble-metal catalysts still, but it is very likely that they will constitute a major portion of the electrolyzer market in the near future.

1.3.3 Electrocatalysts for the Oxygen Evolution and Reduction Reactions

The electrocatalysis of OER and ORR is a broad field that encompasses the study of materials ranging from noble metals to transition metal oxides and nitrides to amorphous high-surface area pyrolyzed carbons containing no metals. The quest to find the best catalyst for these reactions either by high-throughput screening methods(*74–77*), or by carefully selecting materials using bioinspired principles of catalysis(*78–81*), has been an ongoing challenge for the research and industrial community. The end goal is of course a material that is highly active, stable (thousands of hours), and cost-effective, which are competing criteria as very frequently the most active catalysts are either made

of expensive platinum-group metals (PGM's) or if composed of only Earth-abundant elements, are unstable long-term.

The study of crystalline oxides for example of the spinel, perovskite, pyrochlore, and bixbyite mineral classes for the catalysis of water oxidation has now been long established. These classes of materials constitute the most studied electrocatalysts for these reactions to date (outside of noble metals) because they are relatively easy to make, there are wide-ranging compositional spaces possible, and structural and electronic correlations can be made with activity.

In particular, the spinel crystal structure, AB_2X_4 – where A = alkali(ne) or low oxidation state transition metal, B = T.M. of high O.S., and X = O, S – offers a very fruitful opportunity for understanding structural and electronic contributions to catalytic activity because there are a number of different compositional variants that will maintain the same core structure or slight variations of it. The B-site transition metals are coordinated into a M_4O_4 cube reminiscent of some examples of multinuclear molecular water oxidation catalysts(*82–84*) as well as the oxygen-evolving complex (OEC) of photosystem two (PSII). Therefore, this structure type offers an opportunity to study artificial heterogeneous catalysts that have many of the features that have been implicated for water oxidation activity in the molecular and natural systems that tend to be easier to study from a mechanistic point-of-view.

In the Chapters that follow, we examine water oxidation catalysis emergent from heterogeneous compounds that have the spinel or similar structure type, and elucidate the reasons for their enhanced activity or stability. In addition, the study of bifunctional catalysis for oxygen evolution/reduction is presented, and the effect one reaction has on

the other. We offer rational explanations based upon the fundamental principles learned from the natural system, as well as inorganic chemical principles and trends observed in the literature.

1.4 References

1. "The State of Food Insecurity in the World 2015. Meeting the 2015 international hunger targets: taking stock of uneven progress" (Food and Agricultural Organization of the United Nations, 2015).

2. T. F. Stocker *et al.*, "Climate Change 2013: The Physical Science Basis" (Intergovernmental Panel on Climate Change, 2013), (available at http://www.ipcc.ch/report/ar5/wg1/).

3. R. E. Kopp *et al.*, Temperature-driven global sea-level variability in the Common Era. *Proc. Natl. Acad. Sci.* **113**, E1434–E1441.

4. G. De'ath, K. E. Fabricius, H. Sweatman, M. Puotinen, The 27–year decline of coral cover on the Great Barrier Reef and its causes. *Proc. Natl. Acad. Sci.* **109**, 17995–17999 (2012).

5. "Economic contribution of the Great Barrier Reef March 2013" (Great Barrier Reef Marine Park Authority 2013, 2013), (available at http://www.environment.gov.au/system/files/resources/a3ef2e3f-37fc-4c6f-ab1b-3b54ffc3f449/files/gbr-economic-contribution.pdf).

6. R. Howitt, D. MacEwan, J. Medellin-Azuara, J. Lund, D. Sumner, Economic Analysis of the 2015 Drought For California Agriculture (2015).

7. N. S. Lewis, D. G. Nocera, Powering the planet: chemical challenges in solar energy utilization. *Proc Natl Acad Sci U A*. **103**, 15729–35 (2006).

8. J. Tsao, N. Lewis, G. Crabtree, Solar FAQs (2006), (available at http://www.sandia.gov/~jytsao/Solar%20FAQs.pdf).

9. "InternationalEnergy Outlook 2014: World Petroleum and Other Liquid Fuels" (U.S. Energy Information Administration, 2014), (available at https://www.eia.gov/forecasts/ieo/pdf/0484(2014).pdf).

10. G. Morgan, J. Apt, L. Lave, "The U.S. Electric Power Sector and Climate Change Mitigation" (Carnegie Mellon University, 2005).

11. S. Borenstein, Making the Wrong Case for Renewable Energy. *BloombergView* (2012).

12. "Short-Term Energy and Summer Fuels Outlook" (U.S. Energy Information Administration, 2016), (available at http://www.eia.gov/forecasts/steo/pdf/steo_full.pdf).

13. C. Mooney, 2015 the "last effective opportunity" to safely limit warming, says Vatican conference statement. *Wash. Post* (2015).

14. A. J. Bard, M. A. Fox, Artificial photosynthesis: solar splitting of water to hydrogen and oxygen. *Acc. Chem. Res.* **28**, 141–145 (1995).

15. J. A. Turner, A realizable renewable energy future. *Science*. **285**, 687–689 (1999).

16. H. B. Gray, Powering the planet with solar fuel. *Nat. Chem.* **1**, 7–7 (2009).

17. J. BOCKRIS, B. Dandapani, D. Cocke, J. GHOROGHCHIAN, On the splitting of water. *Int. J. Hydrog. Energy*. **10**, 179–201 (1985).

18. J. R. Rostrup-Nielsen, T. Rostrup-Nielson, Large-scale Hydrogen Production (2001), (available at http://www.topsoe.com/sites/default/files/topsoe_large_scale_hydrogen_produc.pdf) .

19. M. Melaina, M. Penev, D. Heimiller, "Resource Assessment for Hydrogen Production: Hydrogen Production Potential from Fossil and Renewable Energy Resources" (NREL/TP-5400–55626, NREL, 2013).

20. G. W. Crabtree, M. S. Dresselhaus, The hydrogen economy. *Phys. Today* (2004).

21. H. D. Hedberg, Geologic Aspects of Origin of Petroleum. *Am. Assoc. Pet. Geol. Bull.* **48**, 1755–1803 (1964).

22. J. S. Dukes, Burning Buried Sunshine: Human Consumption of Ancient Solar Energy. *Clim. Change*. **61**, 31–44 (2003).

23. R. E. Blankenship, Molecular evidence for the evolution of photosynthesis. *Trends Plant Sci.* **6**, 4–6 (2001).

24. D. J. Vinyard, G. M. Ananyev, G. C. Dismukes, Photosystem II: The Reaction Center of Oxygenic Photosynthesis. *Annu. Rev. Biochem.* (2013), doi:10.1146/annurev-biochem-070511-100425.

25. B. KOK, B. FORBUSH, M. McGLOIN, COOPERATION OF CHARGES IN PHOTOSYNTHETIC O2 EVOLUTION–I. A LINEAR FOUR STEP MECHANISM. *Photochem. Photobiol.* **11**, 457–475 (1970).

26. G. Renger, Light induced oxidative water splitting in photosynthesis: Energetics, kinetics and mechanism. *J. Photochem. Amp Photobiol. B Biol.* **104**, 35–43 (2011).

27. J. P. Dekker, R. V. Grondelle, Primary charge separation in Photosystem II. *Photosynth. Res.* **63**, 195–208 (2000).

28. D. J. K. N. C. G. A. R. P. G. nbspCharles Dismukes, N. Cox, G. M. Ananyev, R. J. Pace, G. C. Dismukes, What Are the Oxidation States of Manganese Required To Catalyze Photosynthetic Water Oxidation? *Biophysj*. **103**, 313–322 (2012).

29. G. C. Dismukes, Y. Siderer, EPR spectroscopic observations of a manganese center associated with water oxidation in spinach chloroplasts. *FEBS Lett.* **121**, 78–80 (1980).

30. G. C. Dismukes, Y. Siderer, Intermediates of a polynuclear manganese center involved in photosynthetic oxidation of water. *Proc. Natl. Acad. Sci.* **78**, 274–278 (1981).

31. L. Rapatskiy *et al.*, Detection of the Water-Binding Sites of the Oxygen-Evolving Complex of Photosystem II Using W-Band 17O Electron–Electron Double Resonance-Detected NMR Spectroscopy. *J. Am. Chem. Soc.* **134**, 16619–16634 (2012).

32. J. Yano *et al.*, Where water is oxidized to dioxygen: structure of the photosynthetic Mn4Ca cluster. *Science*. **314**, 821–825 (2006).

33. A. R. Jaszewski, S. Petrie, R. J. Pace, R. Stranger, Toward the Assignment of the Manganese Oxidation Pattern in the Water-Oxidizing Complex of Photosystem II: A Time-Dependent DFT Study of XANES Energies. *Chem. - Eur. J.* **17**, 5699–5713 (2011).

34. A. Guskov *et al.*, Cyanobacterial photosystem II at 2.9-Å resolution and the role of quinones, lipids, channels and chloride. *Nat. Struct. Amp38 Mol. Biol.* **16**, 334–342 (2009).

35. Y. Umena, K. Kawakami, J.-R. Shen, N. Kamiya, Crystal structure of oxygen-evolving photosystem II at a resolution of 1.9 Å. *Nature*. **473**, 55–60 (2011).

36. M. Suga *et al.*, Native structure of photosystem II at 1.95 A resolution viewed by femtosecond X-ray pulses. *Nature*. **517**, 99–103 (2015).

37. J.-R. Shen, The Structure of Photosystem II and the Mechanism of Water Oxidation in Photosynthesis. *Annu. Rev. Plant Biol.* **66**, 23–48 (2015).

38. R. J. Pace, R. Stranger, S. Petrie, Why nature chose Mn for the water oxidase in Photosystem II. *Dalton Trans.* **41**, 7179 (2012).

39. M. Grabolle, H. Dau, Energetics of primary and secondary electron transfer in Photosystem II membrane particles of spinach revisited on basis of recombination-fluorescence measurements. *Biochim. Biophys. Acta BBA - Bioenerg.* **1708**, 209–218 (2005).

40. C. Yocum, The calcium and chloride requirements of the O2 evolving complex. *Coord. Chem. Rev.* **252**, 296–305 (2008).

41. S. Mukherjee *et al.*, Synthetic model of the asymmetric [Mn3CaO4] cubane core of the oxygen-evolving complex of photosystem II. *Proc. Natl. Acad. Sci. U. S. A.* **109**, 2257–2262 (2012).

42. A. Indra, P. W. Menezes, M. Driess, Uncovering Structure-Activity Relationships in Manganese-Oxide-Based Heterogeneous Catalysts for Efficient Water Oxidation. *ChemSusChem*. **8**, 776–785 (2015).

43. N. Keren, A. Berg, P. J. M. van Kan, H. Levanon, I. Ohad, Mechanism of photosystem II photoinactivation and D1 protein degradation at low light: the role of back electron flow. *Proc. Natl. Acad. Sci.* **94**, 1579–1584 (1997).

44. Y. Surendranath, D. G. Nocera, A Self-Healing Oxygen-Evolving Catalyst - Journal of the American Chemical Society (ACS Publications). *J. Am. ...* (2009).

45. Y. Nishi, Lithium ion secondary batteries; past 10 years and the future. *J. Power Sources*. **100**, 101–106 (2001).

46. D. C. Bock, A. C. Marschilok, K. J. Takeuchi, E. S. Takeuchi, Batteries used to Power Implantable Biomedical Devices. *Electrochimica Acta*. **84**, 155–164 (2012).

47. M. S. Whittingham, Lithium batteries and cathode materials. *Chem. Rev.-Columb.* (2004).

48. K. Mizushima, P. C. Jones, P. J. Wiseman, J. B. Goodenough, LixCoO2 (0<x≤1): A New Cathode Material for Batteries of High Energy Density. *Mater. Res. Bull.* **15**, 783–789 (1980).

49. M. M. Thackeray, C. Wolverton, E. D. Isaacs, Electrical energy storage for transportation—approaching the limits of, and going beyond, lithium-ion batteries. *Energy Amp Environ. Sci.* **5**, 7854 (2012).

50. M. Winter, R. J. Brodd, What are batteries, fuel cells, and supercapacitors? *Chem. Rev.* (2004).

51. F. Cheng, J. Chen, Metal-air batteries: from oxygen reduction electrochemistry to cathode catalysts. *Chem. Soc. Rev.* **41**, 2172–2192 (2012).

52. G. Girishkumar, B. McCloskey, A. C. Luntz, S. Swanson, W. Wilcke, Lithium−Air Battery: Promise and Challenges. *J. ...* (2010) (available at http://pubs.acs.org/doi/abs/10.1021/jz1005384).

53. L. Trahey *et al.*, Synthesis, Characterization, and Structural Modeling of High-Capacity, Dual Functioning MnO2 Electrode/Electrocatalysts for Li-O2 Cells. *Adv. Energy Mater.* **3**, 75–84 (2013).

54. X. Han, F. Cheng, C. Chen, Y. Hu, J. Chen, Uniform MnO2 nanostructures supported on hierarchically porous carbon as efficient electrocatalysts for rechargeable Li-O2 batteries. *Nano Res.* **8**, 156–164 (2014).

55. W. Yang *et al.*, Perovskite Sr 0.95 Ce 0.05 CoO 3−δ loaded with copper nanoparticles as a bifunctional catalyst for lithium-air batteries. *J. Mater. Chem.* **22**, 18902–18907 (2012).

56. B. M. Gallant *et al.*, Chemical and Morphological Changes of Li–O 2Battery Electrodes upon Cycling. *J. Phys. Chem. C*. **116**, 20800–20805 (2012).

57. A. Grimaud, J. Suntivich, Y. Shao-Horn, Toward the rational design of non-precious transition metal oxides for oxygen electrocatalysis - Energy & Environmental Science (RSC Publishing) DOI:10.1039/C4EE03869J. *... Amp Environ. ...* (2015).

58. J. Suntivich *et al.*, Design principles for oxygen-reduction activity on perovskite oxide catalysts for fuel cells and metal–air batteries. *Nat. Chem.* **3**, 546–550 (2011).

59. K. Zhang *et al.*, Mesoporous Cobalt Molybdenum Nitride: A Highly Active Bifunctional Electrocatalyst and Its Application in Lithium–O2 Batteries. *J. ...* (2013).

60. J. O. Jensen *et al.*, PRE-INVESTIGATION OF WATER ELECTROLYSIS (2008).

61. Z. Abdin, C. J. Webb, E. M. Gray, Modelling and simulation of a proton exchange membrane (PEM) electrolyser cell. *Int. J. Hydrog. Energy*. **40**, 13243–13257 (2015).

62. S. A. Grigoriev, V. I. Porembsky, V. N. Fateev, Pure hydrogen production by PEM electrolysis for hydrogen energy. *Int. J. Hydrog. ...* (2006) (available at http://www.sciencedirect.com/science/article/pii/S036031990500145X).

63. A. J. Bard, Photoelectrochemistry. *Science*. **207**, 139–144 (1980).

64. H. Wang, T. Deutsch, J. A. Turner, Direct Water Splitting under Visible Light with Nanostructured Hematite and WO3 Photoanodes and a GaInP2 Photocathode. *J. Electrochem. Soc.* (2008).

65. R. Michalsky, V. Botu, C. M. Hargus, A. A. Peterson, A. Steinfeld, Design Principles for Metal Oxide Redox Materials for Solar-Driven Isothermal Fuel Production. *Adv. Energy Mater.* **5**, 1401082 (2015).

66. J. E. Funk, Thermochemical hydrogen production: past and present. *Int. J. Hydrog. Energy*. **26**, 185–190 (2001).

67. J. R. Varcoe *et al.*, Anion-exchange membranes in electrochemical energy systems. *Energy Environ. Sci.* **7**, 3135–3191 (2014).

68. J. W. Desmond Ng, Y. Gorlin, T. Hatsukade, T. F. Jaramillo, A Precious‐Metal‐Free Regenerative Fuel Cell for Storing Renewable Electricity. *Adv. Energy Mater.* **3**, 1545–1550 (2013).

69. D. Stolten, B. Emonts, *Fuel Cell Science and Engineering: Materials, Processes, Systems and Technology* (Wiley, Weinheim, Germany, 2012), vol. 1.

70. K. E. Ayers *et al.*, Research Advances towards Low Cost, High Efficiency PEM Electrolysis (2010).

71. K. E. Ayers, C. Capuano, E. B. Anderson, Recent Advances in Cell Cost and Efficiency for PEM-Based Water Electrolysis (2012).

72. J. D. Joe, D. B. S. Kumar, P. Sivakumar, Production Of Hydrogen By Anion Exchange Membrane Using AWE. *ijstr.org* (2014).

73. J. Parrondo *et al.*, Degradation of anion exchange membranes used for hydrogen production by ultrapure water electrolysis. *RSC Adv.* **4**, 9875–9879 (2014).

74. J. A. Haber *et al.*, High‐Throughput Mapping of the Electrochemical Properties of (Ni‐Fe‐Co‐Ce) Ox Oxygen‐Evolution Catalysts. *ChemElectroChem*. **1**, 524–528 (2014).

75. J. B. Gerken, J. Y. C. Chen, R. C. Massé, A. B. Powell, S. S. Stahl, Development of an O2-Sensitive Fluorescence-Quenching Assay for the Combinatorial Discovery of Electrocatalysts for Water Oxidation. *Angew. Chem. Int. Ed.* **51**, 6676–6680 (2012).

76. J. Koh *et al.*, Combinatorial high-throughput optical screening for optimum composition of highly active ruthenium based ternary catalysts in oxygen reduction reaction. *Int. J. Hydrog. Energy*. **40**, 11615–11624 (2015).

77. D. Seley, K. Ayers, B. A. Parkinson, Combinatorial Search for Improved Metal Oxide Oxygen Evolution Electrocatalysts in Acidic Electrolytes. *ACS Comb. Sci.* **15**, 82–89 (2013).

78. G. C. Dismukes *et al.*, Development of Bioinspired Mn 4O 4−Cubane Water Oxidation Catalysts: Lessons from Photosynthesis. *Acc. Chem. Res.* **42**, 1935–1943 (2009).

79. R. Brimblecombe, A. Koo, G. C. Dismukes, G. F. Swiegers, L. Spiccia, Solar Driven Water Oxidation by a Bioinspired Manganese Molecular Catalyst. *J. Am. Chem. Soc.* **132**, 2892–2894 (2010).

80. S. Chatterjee, K. Sengupta, S. Hematian, K. D. Karlin, A. Dey, Electrocatalytic O2-Reduction by Synthetic Cytochrome c Oxidase Mimics: Identification of a "Bridging Peroxo" Intermediate Involved in Facile 4e(-)/4H(+) O2-Reduction. *J. Am. Chem. Soc.* **137**, 12897–12905 (2015).

81. K. Sengupta, S. Chatterjee, A. Dey, Catalytic H 2O 2Disproportionation and Electrocatalytic O 2Reduction by a Functional Mimic of Heme Catalase: Direct Observation of Compound 0 and Compound I in Situ. *ACS Catal.*, 1382–1388 (2016).

82. R. Brimblecombe *et al.*, Sustained Water Oxidation by [Mn 4O 4] 7+Core Complexes Inspired by Oxygenic Photosynthesis. *Inorg. Chem.* **48**, 7269–7279 (2009).

83. P. F. Smith *et al.*, Water Oxidation by the [Co4O4(OAc)4(py)4]+ Cubium is Initiated by OH– Addition. *J. Am. Chem. Soc.* **137**, 15460–15468 (2015).

84. S. Berardi *et al.*, Photocatalytic Water Oxidation: Tuning Light-Induced Electron Transfer by Molecular Co 4O 4Cores. *J. Am. Chem. Soc.* **134**, 11104–11107 (2012).

Chapter 2, Section 1 and 2 are adapted from the following publications:

(1) Gardner, Graeme P.; Go, Yong Bok; Robinson, David M.; Smith, Paul F.; Hadermann, Joke; Abakumov, A.; Greenblatt, Martha; Dismukes, G. Charles, "Structural Requirements in Lithium Cobalt Oxides for the Catalytic Oxidation of Water". *Angewandte Chemie International Edition*, 2012, 51, 1616-1619.

(2) Gardner, Graeme; Al-Sharab, Jafar; Danilovic, Nemanja; Go, Yong Bok; Ayers, Katherine; Greenblatt, Martha; Dismukes, G. Charles, "Structural Basis for differing electrocatalytic water oxidation by the cubic, layered and spinel forms of lithium cobalt oxides". *Energy and Environmental Science*, 2015, 9, 184-192.

Chapter 2. Structural Requirements for Catalysis: Crystalline Polymorphs of Lithium Cobalt Oxide Behavior Under Photochemical and Electrolytic Water Oxidation

2.1 Photochemical Water Oxidation

2.1.1 Introduction

Development of water oxidation catalysts (WOCs) to replace costly noble metals in commercial electrolyzers and solar fuel cells has been an unmet need preventing global development of hydrogen fuel technologies. Two of the main challenges in realizing catalytic water splitting are: 1) lowering the substantial overpotential to achieve practical operating current densities at the anodic O_2-evolving half-reaction, and 2) use of earth-abundant elements for fabrication of inexpensive electrodes free from noble metals. To meet these challenges, molecular catalysts based upon the cubical $CaMn_4O_x$ core within Photosystem II (PSII) of photosynthetic organisms, the gold standard of catalytic efficiency, have begun to appear(*1–4*).

Among solid state materials, several noble metal oxides including IrO_2 and RuO_2 are already in use in industrial electrolyzers, but are not globally scalable(*5–8*). Aqueous cobalt phosphate solutions form water oxidation catalysts under electrolysis(*9–12*) and photolysis(*13*) suitable for fabrication of noncrystalline electrode materials.

Nanocrystalline spinel phase metal oxides (AB_2O_4), comprised of B_4O_4 cubical subunits (B = transition metals), have been developed that are active water oxidation catalysts.(*14–17*) Catalytic activity of the spinel Co_3O_4 has been reported for nanorods incorporated in SBA-15 silica(*18*) and Co_3O_4 nanoparticles on Ni electrodes(*19*). $NiCo_2O_4$ spinel has also exhibited water oxidation when the nanoparticles were electrophoretically deposited onto a Ni electrode(*20*, *21*). Reports examining the effect of lithium doping on the surface of Co_3O_4 electrodes in alkaline KOH solutions attributed the higher O_2 evolution rate to better electrical conductivity(*22–24*). However, water oxidation activity by Co_3O_4 exhibited a strong dependence on crystallite size and surface area, frequently necessitating high overpotentials and alkaline conditions to accelerate the rate(*20*, *25*, *26*).

In contrast, we recently reported that the catalytically inert spinel $LiMn_2O_4$, upon topotactic delithiation yields spinel λ-MnO_2, which is an active water oxidation catalyst, thus revealing the importance of removing the A site lithium for catalysis by the cubical Mn_4O_4 core of spinels(*14*).

Lithium-containing metal oxides are well-researched cathode materials for lithium-ion batteries. In particular, lithium cobalt oxide has been implemented extensively in those applications, and its electrochemical properties have been examined thoroughly. It occurs as two crystalline polymorphs of identical composition (**Figure 2.1**): cubic spinel-like $Li_{1+y}Co_2O_4$ (*Fd*-3*m*; $y \leq 1$), simplified as $Li_2Co_2O_4$ and rhombohedral layered $LiCoO_2$(*27*, *28*). Layered lithium cobalt oxide is an effective cathode material for lithium batteries with a higher energy density and better stability than the corresponding cubic phase(*29*). Herein, we show that of the two, only the cubic phase $Li_2Co_2O_4$ is active in catalyzing

water oxidation, when driven either electrolytically or with a photochemically generated oxidant.

We investigated these materials to test the bio-inspired hypothesis(*30*), namely, whether the cubical B_4O_4 core is a general feature for efficient catalysis of water oxidation(*14*). Comparison of the atomic structures of cubic $Li_2Co_2O_4$ and layered $LiCoO_2$ (**Figure 2.1a**, and **b** respectively) reveals that only the former possesses cubical Co_4O_4 units within the lattice, while layered $LiCoO_2$ is comprised of alternating layers of Co-O and Li-O octahedra that form $LiCo_3O_4$ units and no cubical Co_4O_4 subunits.

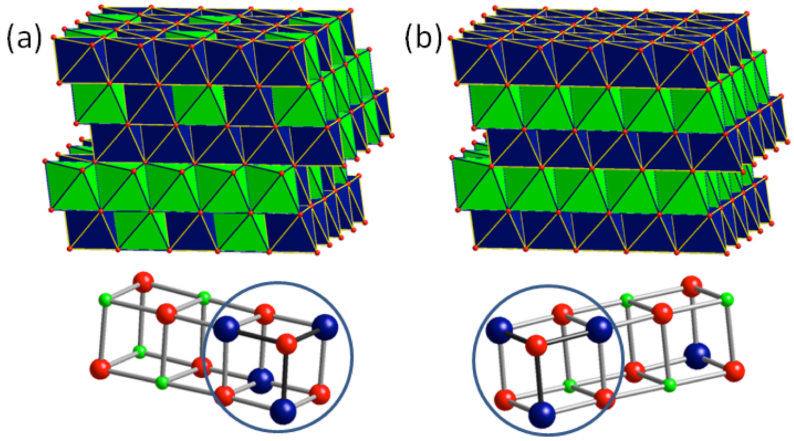

Figure 2.1 Polyhedral (top) and ball-and-stick (bottom) representations of (a) the cubic $LiCoO_2$ crystal structure with Co_4O_4 cubic units and (b) the layered $LiCoO_2$ structure containing $LiCo_3O_4$ incomplete cubes. Li, Co, and O spheres are green, clue, and red, respectively.

2.1.2 Experimental

A sol-gel method, as previously described(*31*, *32*), was adapted to prepare nanocrystalline powders of both the cubic $Li_2Co_2O_4$ and layered $LiCoO_2$. Briefly, an aqueous solution of 4 mmol of $LiNO_3$, $Co(NO_3)_2{\cdot}6H_2O$, citric acid and urea (molar Li:Co:C:U was 1:1:2:2) was evaporated at 80 °C for 4–6 h. The gel that was formed was dried to completeness overnight at 170 °C. The sponge-like xerogel was crushed to form

a powder and subjected to various calcination temperatures. The precursor powder was decomposed at different temperatures (400, 500, 600, and 700 °C) for 1–2 h.

The products were characterized structurally by powder X-ray diffraction (PXRD), on a Bruker D8 Advance Diffractometer (Cu Kα) in the 2θ range 10-80°, and precession electron diffraction (PED), on a Philips CM20 equipped with a Spinning Star precession instrument. PED patterns were recorded on a CCD camera, and line profile was extracted using the commercial software ELD, which was treated using JANA2006. Scanning electron microscopy (SEM), was performed on a Zeiss Sigma field emission SEM equipped with Oxford EDSLEO. BET surface area analysis was determined by a Quantachrome Autosorb porosity analyzer. Thermogravimetric analysis (TGA), and differential scanning calorimetry (DSC) was performed on a TA Instrument 2050 from room temperature to 700 °C with a heating rate of 5 °C/min in nitrogen and air. Elemental composition (Li:Co ratios) was determined by inductively-coupled-plasma optical emission spectroscopy (ICP-OES) on a Vista-PRO simultaneous CCD with continuous wavelength coverage of 167-785 nm.

Oxygen evolution data were collected on the Clark type oxygen electrode thermostatted at 23 °C (Hansatek Ltd), which was calibrated at air saturation and anoxic with both sodium dithionate and N_2 purged solutions. The assay used for water oxidation experiments was a solution of $1x10^{-3}$ M $Ru(bpy)_3Cl_2 \bullet 6H_2O$ and $2.0x10^{-2}$ M $Na_2S_2O_8$ in a bicarbonate and sodium hexafluorosilicate buffer poised at pH 5.8, a commonly used photo-oxidant system(*6*). $LiCoO_2$ powders were washed in neutral water and dried fully @ 100 °C before testing. The total experimental volume was 2 mL in all cases. Catalyst suspensions tested were about 200 ppm and were sonicated for 5 – 10 min before

measurements. The chamber was illuminated with a mercury arc lamp with filters for UV (395 nm cut-off filter) and IR (aqueous $CuSO_4$ solution) at a light intensity of 4.3 mW/cm^2 measured by a Newport power meter. Oxygen yield was confirmed on a GOW MAC Series 350 Gas Chromatograph with a thermal conductivity detector.

Electrochemical data presented in this study (2.1) were collected on a CH Instruments Electrochemical Workstation using CHI version 7.21 (copyright © 1994-2007) software. Bulk electrolysis was performed at 1.2 V vs Ag/AgCl in pH 7.2, 0.1 M phosphate buffer at room temperature, with constant stirring. Cyclic voltammograms (CV's) were recorded for all samples with 50 mV/sec scan rate to determine the catalytic wave onset potential. Electrode membranes were fabricated by spin coating 15 μL of 9 mg/mL lithium cobalt oxide suspensions (400-$Li_2Co_2O_4$ or 700-$LiCoO_2$) in Nafion® neutralized with NaOH (in alcohols, 3.3% by weight)(*33*) onto ITO glass slides approximately 2.5 cm^2 in area. The membranes were cured at 120 °C for at least 15 min to dry off any remaining solvent. During experiments, only a small circle of diameter 0.65 cm on the working electrode was exposed to solution using a custom-made glass electrochemical cell.

2.1.3 Results

The PXRD patterns in **Figure 2.2a-d** show a structural transformation with increasing temperature of synthesis from cubic at 400 °C to the thermodynamically favored layered phase above 600 °C. A mixture of these two phases appears at 500 °C. The splitting of peaks 222 and 440, as well as the shift of 111 peak to the corresponding 003 peak, indicate the formation of layered $LiCoO_2$(*34*, *35*). Co_3O_4 as an impurity was not observed. Heating can be accompanied by a substantial increase in crystallinity and

particle size, when the samples are synthesized by solid-state reactions. The average particle size of layered $LiCoO_2$ prepared at 800 °C via a solid-state reaction was 1~2 μm and yielded sharper PXRD reflections (**Figure 2.3**). In contrast, with sol-gel synthesis, the crystallite size was controlled to nano-dimensions. SEM images of the products reveal average particle sizes of ~50 nm for the low temperature materials (**Figure 2.4a-c**) and 100 nm for the highest temperature material (**Figure 2.4d**). BET measurements of the 400 °C sol-gel material (56.19 m^2g^{-1}) reveal that the surface area is four times that of the 700 °C material (**Table 2.1**), consistent with the doubling of particle size seen by SEM (**Fig. 2.4**). The lithium to cobalt ratios (1:1 by ICP-ES) were independent of synthesis temperature for all samples (**Table 2.1**).

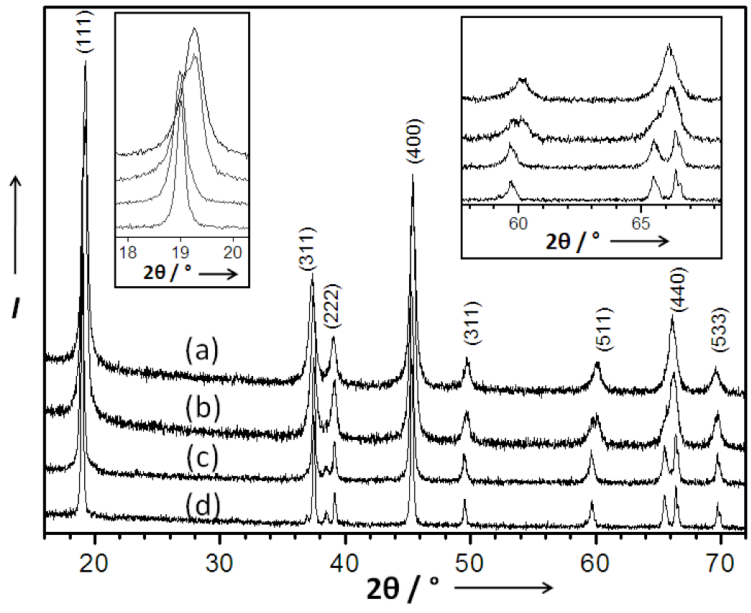

Figure 2.2 PXRD patterns of $LiCoO_2$ calcined at (a) 400 °C (b) 500 °C (c) 600 °C and (d) 700 °C. The insets show the structural evolution from cubic to layered, notably the shift of the 111 peak (2θ = ~19°) to lower angle 003 peak, and the splitting of the 440 peak (2 θ = ~66°) to 018 and 110 peaks.

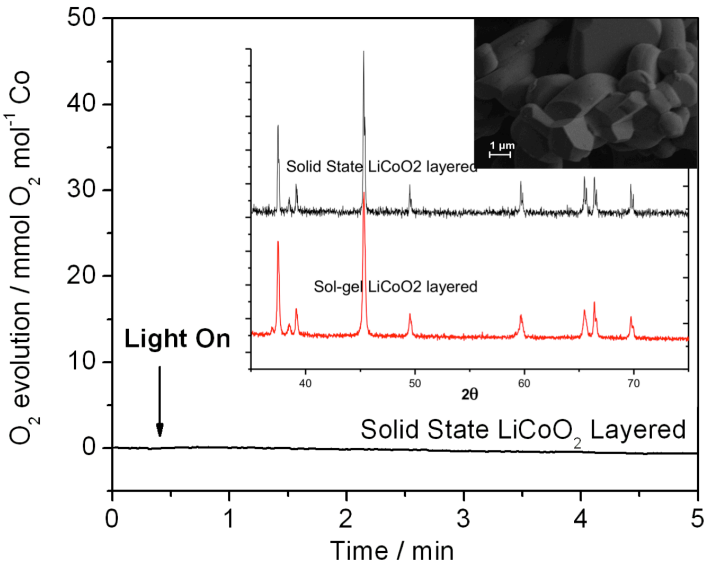

Figure 2.3 PXRD patternds as well as SEM image and O_2 evolution trace of layered $LiCoO_2$ prepared by solid-state methods. The SS-$LiCoO_2$ has sharper reflections in the PXRD (first inset) and very large crystallite size (second inset). The result is completely dead catalyst for oxygen evolution as measured by Clark electrode.

Table 2.1 List of surface areas determined using the BET method and Li:Co ratio as a function of calcination temperature

Calcination Temperature (°C)	BET Surface Area (m^2 g^{-1})	Li:Co Ratio	Co from sample washes (mass %)
400	56.19	0.911	<0.1
500	26.30	1.04	N/A
600	21.83	0.961	N/A
700	14.24	0.924	<0.1

Thermogravimetric analysis (TGA) and differential scanning calorimetry (DSC) of the sol-gel precursor were done in parallel to continuously follow mass loss and the heat capacity during synthesis of the product. The TGA and DSC curves shown in **Figure 2.5** indicate two mass losses, corresponding to the decomposition of ammonium citrate and ammonium nitrate from 200°C to 300°C, and decomposition of remaining primarily polymeric carbon LiCo(citrate) to $Li_2Co_2O_4$ from 300°C to 430°C, which also corresponds to the sharp heat transfer peak in the DSC graph(*36*). Above this temperature to 700°C there is no further mass loss and only a slow conversion to the more stable

layered $LiCoO_2$. These data demonstrate that above 430 °C, there are no residual organics or water.

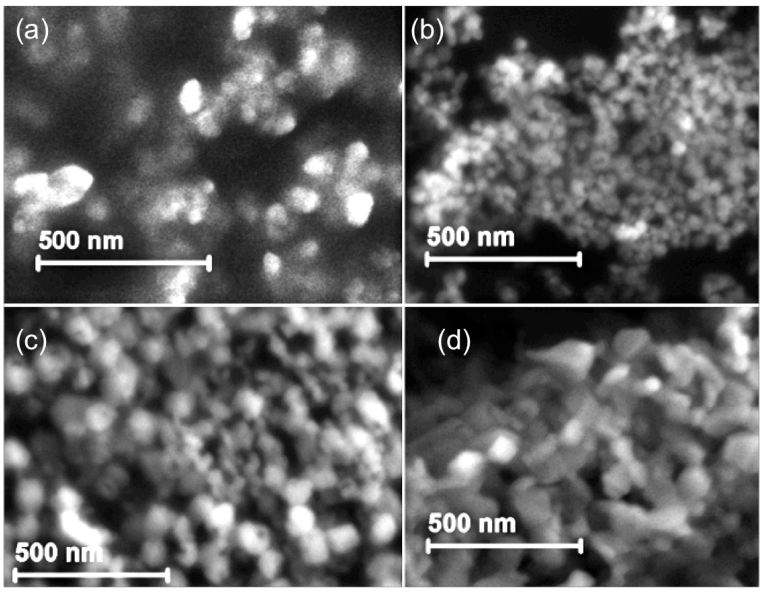

Figure 2.4 SEM images of LiCoO2 calcined at (a) 400 °C, (b) 500 °C, (c) 600 °C, and (d) 700 °C.

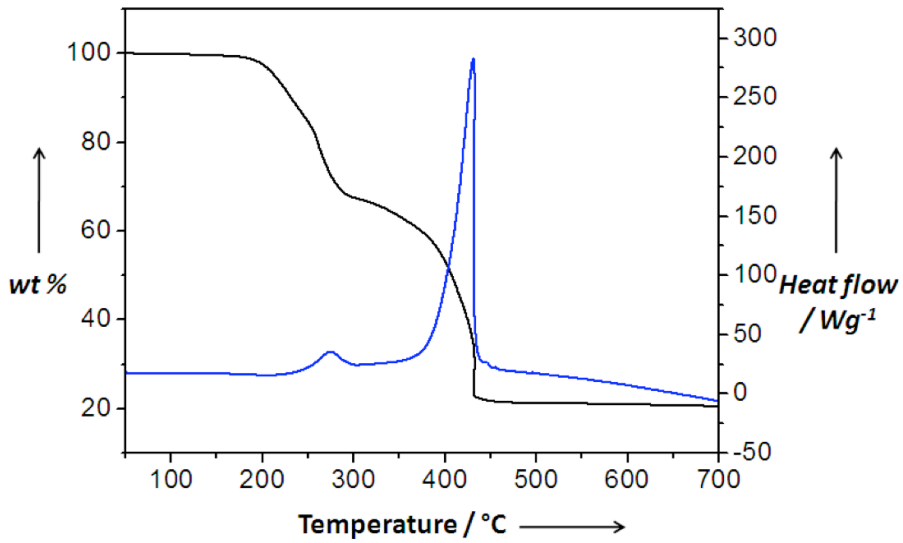

Figure 2.5 TGA (black) and DSC (blue) curves of the xerogel decomposition to form crystalline $LiCoO_2$. The first weight loss corresponds to the formation of the polymeric intermediate, followed by the combustion of citrate above 350 °C forming crystalline $LiCoO_2$.

Photocatalytic water oxidation was monitored in solution through detection of dissolved O_2 by Clarke-type electrode. The potential needed to drive water oxidation was

provided by a commonly used photosensitizer assay ($Ru(bpy)_3^{2+}/Na_2S_2O_8$) in a pH 5.8 sodium hexafluorosilicate buffer(*6*) adjusted with $NaHCO_3$(*3*, *14*). Visible light-driven O_2 evolution, normalized to the total number of moles of cobalt in solution and to the surface area, are shown in **Figure 2.6**, top and bottom, respectively. O_2 evolution was independently determined by GC of solution headspace (**Figure 2.7**).

The catalyst turnover frequency (TOF) determined from the initial slope of the dissolved O_2 concentration (**Figure 2.6**, top) is 1.0 x 10^{-3} s^{-1} for pure cubic (400 °C) $Li_2Co_2O_4$ per bulk cobalt atom, 10-fold greater than for λ-MnO_2 prepared from the analogous $LiMn_2O_4$ spinel(*14*). However, since only surfaces sites are known to be active in catalysis(*18*, *19*), this rate is considered a conservative, lower bound estimate. When normalized to the surface accessible cobalt (calculated from BET surface area and crystal lattice parameters), the TOF is 1.9 x 10^{-2} s^{-1}. The catalytic activity per surface area decreases with increased calcination temperature and corresponding change in crystal structure (**Fig. 2.6a to 2.6c**). Finally, pure layered $LiCoO_2$ exhibits no activity (**Fig. 2.6d**). Although the 600 °C material is primarily layered based on the PXRD pattern (**Fig. 2.2c**), the presence of some residual cubic phase was established by precession electron diffraction (PED). PED ring patterns of the sets of nanoparticles were taken, after which a line profile was extracted radially through the pattern. This line profile was analyzed with a Le Bail-fit in JANA2006(*37*). As shown in **Figure 2.8**, the profile agrees well with the layered phase, except for the presence of a peak around d = 0.54 Å (indicated with a rectangle in the top figure). The presence of the peak agrees with the cubic phase (**Figure 2.8b**), whereas the overall agreement of the whole pattern is less than with the layered phase. The combination of both phases (**Figure 2.8c**) gives the best agreement. Hence,

we conclude that the small amount of cubic lithium cobalt oxide present in the 600 °C material is likely responsible for the residual O_2 evolution activity in **Figure 2.6c**.

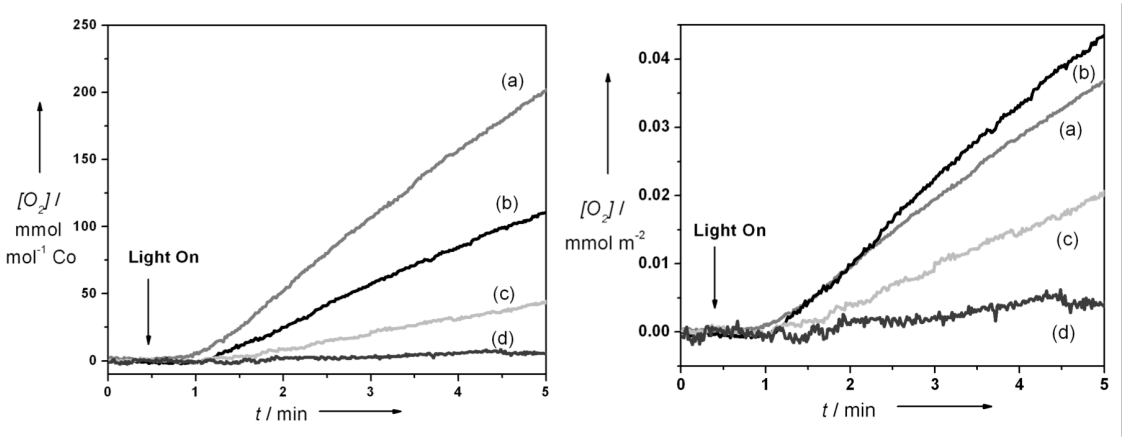

Figure 2.6 Oxygen evolution rate measured by Clark electrode (dissolved O_2 concentration) for $LiCoO_2$ prepared at (a) 400 °C, (b) 500 °C, (c) 600 °C, and (d) 700 °C. The concentration of O_2 is normalized to total moles of Co (left) and to total surface area (right). The rate is extracted from the initial slope (linear regression, first 2 minutes). Conditions: 23 °C, pH 5.8, 1mM $[Ru(bpy)_3]^{2-}$, 20 mM $Na_2S_2O_8$, and 200 ppm catalyst.

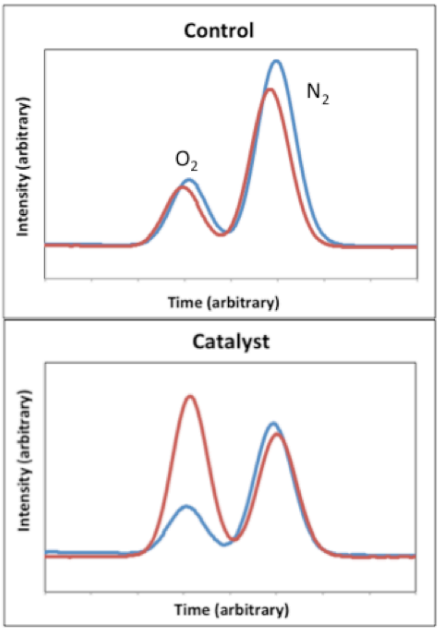

Figure 2.7 Headspace O_2 (and N_2) as measured by gas chromatograph before (blue) and after (red) 1 hour of illumination in the photochemically-driven water oxidation assay

The structural and chemical integrity of cubic $Li_2Co_2O_4$ before and after photocatalysis was monitored by PXRD and ICP-ES, which demonstrated no change in crystal structure

(**Figure 2.9**) and absence of dissolution of cobalt in sample washes (less than 0.1% dissolved cobalt in both low and high temperature materials, **Table 2.1**). Additionally, greater than 97% of the material can be reclaimed after the experiment, with 3% being attributable to mass transfer loss.

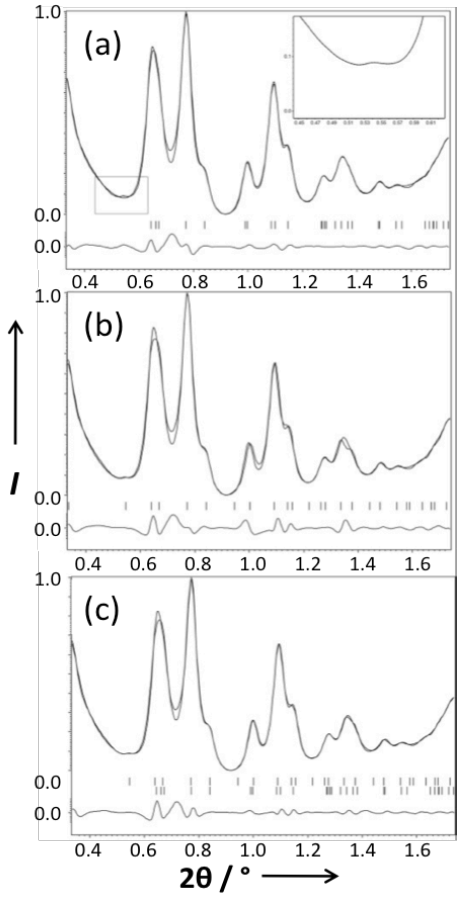

Figure 2.8 Precession electron diffraction (PED) patterns along with Le Bail fits to the experimental profiles for 600 °C $LiCoO_2$ using (a) layered, (b) cubic, and (c) both phases together. Best fit is obtained by using both phases.

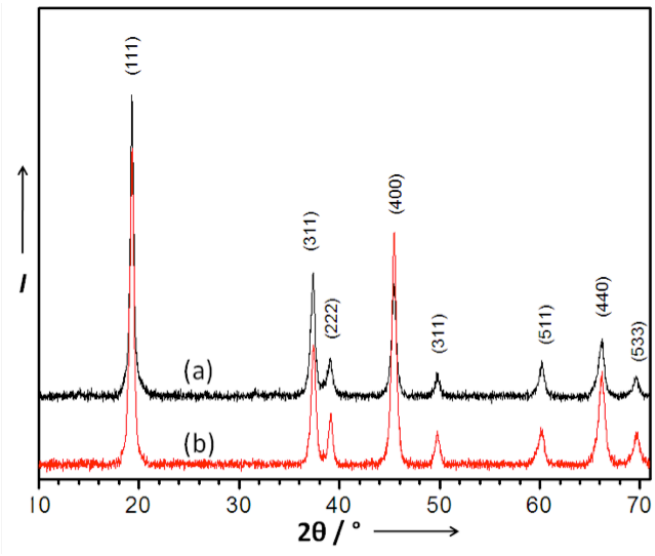

Figure 2.9 PXRD patterns of cubic $Li_2Co_2O_4$ prepared at (a) 400 °C, and (b) after 1 hour of photochemically-driven water oxidation.

Electrochemical measurements were performed on membrane electrode assemblies (MEA) prepared by spin-coating ITO electrodes with a controlled amount of a suspension containing neutralized Nafion® (in MeOH, 4 % by weight) and lithium cobalt oxide powders(*33*). Bulk electrolysis data at 1.2 V (vs Ag/AgCl) in pH 7.2 phosphate buffer, shown in **Figure 2.10**, provide clear evidence that the MEA containing cubic 400-$Li_2Co_2O_4$ exhibits 50-fold greater current density (> 250 μA/cm^2), resulting from water oxidation, than the MEA containing layered 700-$LiCoO_2$ with equal loading (< 10 μA/cm^2). The latter is only slightly above the background current (Nafion-only MEA). The consistent trend in catalytic turnover seen for the results from both the solution assay (**Figures 2.6a-d**) and the electrolytic MEAs (**Figure 2.10**), establishes unequivocally the determining role of crystal structure and the major advantage that the M_4O_4 cubical core provides for water oxidation.

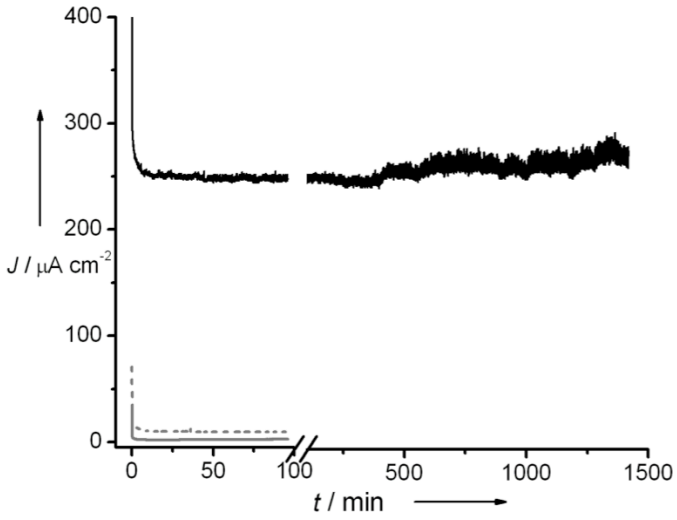

Figure 2.10 Bulk electrolysis (chronoamperometry) performed in 0.1 M phosphate buffer (pH 7.2) at 1.2 V vs Ag/AgCl of 400°C-$Li_2Co_2O_4$ (solid black line), 700°C-$LiCoO_2$ (dashed gray line) and control (solid gray line). Electrodes were prepared by spin-coating inks containing catalyst and Nafion onto ITO substrates.

2.1.4 Discussion

Previously, a dependence on the surface area of a catalyst for water electrolysis was demonstrated with Co_3O_4 nanospinel (with A = Co not Li) loaded on Ni foam electrode, with smaller particles yielding higher catalytic activity(*19*). In the photochemical and electrochemical systems of this study, it is seen that decreasing surface area clearly decreases activity of the same phase. Similar dependence was seen for λ-MnO_2(*14*). By contrast, neither surface area nor particle size was found to activate catalytic water oxidation by the layered polymorph of $LiCoO_2$.

With identical stoichiometries and coordination numbers for all metal centers in two polymorphs of lithium cobalt oxide, a comparison can be made isolating atomic arrangement as the major determinant of catalytic activity. The bioinspired hypothesis tested herein(*30*), posits that the oxo-metallic M_4O_4 cubes of cobalt present in the cubic $Li_2Co_2O_4$ may function analogously to both the $CaMn_4O_x$ core of the photosynthetic WOC, and the molecular cubane catalysts of manganese(*1*) and cobalt(*3*) reported

previously. There is no direct evidence, as of yet, which identifies exactly what is responsible for the activity of cubical oxo-metallic cores for water oxidation in any of these systems. Although the nanocrystalline component is a significant factor in eliciting higher catalytic activity in heterogeneous catalysis, across the board, it is not singularly, nor primarily responsible in the case of lithium cobalt oxides. Given the high natural abundance, ease of synthesis, high thermal and redox cycling stability, intrinsic high TOF, and stable current density, cubic $Li_2Co_2O_4$ holds promise for applications in electrolyzers and solar-driven fuel cells.

2.1.5 Acknowledgements

This work was supported by Rutgers University AFOSR-FA9550-05-1 and FA9550-11-1 (G.C.D.). We aknowledge partial support by NSF-DMR-0966829 (M.G. and Y.B.G.) and an NSF predoctoral fellowship (D.M.R.). We thank Paul Field for help with elemental analysis, Zhijuan Zhang for BET measurements, and Jun Chen and Gerry Swiegers for help with electrochemical measurements. This paper honors the memory of our teacher, Peter Gabriel.

2.2 Origins of Activity and Stability in Cubic, Spinel, and Layered $LiCoO_2$ for Electrochemical Water Oxidation

2.2.1 Introduction

Electrolytic storage of solar energy through water splitting chemistry, eqs. 1 & 2, is recognized as indispensable for achieving widespread adoption of photovoltaic and wind

electrical sources that displace fossil energy.(*38*, *39*) The energy storage density of chemical bonds exceeds that of any battery yet conceived by 100 fold or more, is long-term stable, more scalable, and can be used for other applications (e.g. hydrogen)(*40*). If done efficiently, it would transform both the electrical power and fuel industries. Presently, electrolyzer stacks operate at best case efficiencies of 74% (proton exchange membrane, PEM(*41*) and 68% (alkaline)(*42*) due in part to fundamental limitations in the catalysts. The O_2 evolution (OER) and H_2 evolution (HER) half-reactions require catalysts at the respective electrodes to lower the intrinsic barriers to these multi-electron/proton reactions. Electrocatalysts allow reactions to proceed faster by lowering activation energy barriers and thus save energy otherwise wasted as heat.

anode: $2H_2O \rightarrow O_2 + 4H^+$ and $4e^-$ (1a)

$4OH^- \rightarrow O_2 + 2H_2O + 4e^-$ (1b)

cathode: $2H_2O + 2e^- \rightarrow 2H_2 + 2OH^-$ (2a)

$2H^+ + 2e^- \rightarrow H_2$ (2b)

The main kinetic bottleneck for water splitting occurs at the anode in which the endothermic oxidation process that produces O_2 has an additional activation energy barrier (energy above the thermodynamic potential energy) that depends on the reaction pathway taken. The mechanism may entail sequential or concerted four electron/proton removal steps each with different barriers. The most efficient OER catalysts to date in solid acid electrolyte are ruthenium (RuO_2) and iridium oxide (IrO_2), which generally have overpotentials of ~300 mV at pH 14 and pH 0, respectively, at 10 mA cm^{-2} current density.(*43–45*) However, owing to their low natural abundances and high costs, RuO_2 and IrO_2 are not suitable for large-scale use(*8*). For these reasons there is intense interest

in developing comparably efficient catalysts for the OER reaction that use earth-abundant elements and have low processing cost.

It has been known for more than 30 years that first-row transition metal oxides, particularly the perovskite, spinel and pyrochlore structure types, can catalyze oxygen evolution from strongly alkaline solutions(*43*, *46*, *47*, *13*, *23*, *22*). However, the oxides of first-row transition metals have so far been relatively unsuitable because of two limitations: instability due to corrosion in acids - conditions used in present day PEM electrolyzers(*44*, *45*, *48*) - and inability to generate the necessary current densities at low overpotentials (inefficiency). Commercial alkaline electrolyzers can use low-cost Ni electrodes as catalysts, but these require 30% KOH electrolyte and elevated temperature to achieve competitive efficiencies below PEM electrolyzers(*49*, *50*). This combination of high corrosion and need for thermal management is dangerous and costly. Commercial electrolyzers employing alkaline exchange membranes (AEM) do not yet exist. OER and HER catalysts can also be prepared as amorphous oxide coatings generated *in situ* by controlled electrolysis of non-noble metal electrodes, or by electrodeposition of soluble precursors(*9*, *51–58*). Some films exhibit high initial activity, but typically are unstable over time at high current densities owing to dissolution and passivation of the surface(*59–61*). The amorphous forms have a high degree of defects.(*10*, *13*, *62*, *63*) Overcoming these limitations is a challenge due to the lack of structural knowledge for films.

Of the first-row transition metals selected for the OER, nickel, iron, and especially cobalt have been front-runners as both homogeneous and heterogeneous catalysts due to low overpotentials, approaching those of the noble metal analogues. In contrast to noble

metals however, not all such materials are stable as high surface area nanoparticles. The crystalline oxides tend to be spinel-type: Co_3O_4(*64*, *65*), $NiCo_2O_4$(*66*, *67*), $LiCoO_2$(*68*, *69*), perovskite-type: $LaCoO_3$(*60*, *70*), $SrCoO_3$(*43*, *71*), or layered oxy-hydroxides(*72*, *73*). In particular, exceptional activity has been observed in mixed nickel and iron hydroxide/oxide catalysts(*74*). Under acidic electrolysis conditions, such as used in proton exchange membranes (PEM's), materials containing cobalt or nickel are highly susceptible to dissolution.

Since the discovery of lithium cobalt oxide as a highly active catalyst for water oxidation[31], there have been subsequent reports that have sought to further explain the nature of the apparent crystal structure dependence on catalysis(*69*, *75–78*). Our group was the first to report that cubic $LiCoO_2$ (Fd-3m, also called lithiated spinel) can catalyze water oxidation near neutral pH using a photochemically driven-system, while the layered polymorph (trigonal space group, R-3m) cannot, even after accounting for the effects of surface area. It has been reported that layered $LiCoO_2$ is unstable after repeated electrochemical cycling in neutral and basic conditions and that this instability is linked to surface structural changes(*75*). In Ref. 36, it was suggested that the active phase for catalysis is an amorphous surface similar to the CoO_x of electrodeposited materials, and that a crystalline spinel phase only serves to passivate the catalyst. A separate study also found that the layered $LiCoO_2$ is unstable (current decays) in long-term (~20 hours) studies, but in contrast to the aforementioned study, they found both cubic $LiCoO_2$ and chemically delithiated $Li_{1-x}CoO_2$ ($0 \leq x \leq 1$) are electocatalytically active and stable(*69*). Before any studies of water oxidation electrocatalysis with $LiCoO_2$ were reported, the relative activity and stability of the two polymorphs had been a source of active

discussion in the battery literature. The structural dynamics of the system in non-aqueous electrochemistry has been elucidated(*29*, *79*, *80*). The layered $LiCoO_2$, which is superior for Li secondary battery applications, undergoes surface and sub-surface reconstruction to cubic and spinel phases after repeated charge/discharge cycles and at intermediate and low values of Li stoichiometry that results in reduced performance(*29*, *79*). This transformation can also be induced thermally above 1000 °C, where Li starts to evaporate, leaving behind a solid solution of cubic and layered phase $LiCoO_2$ and Co_3O_4 as surface nodules(*81*). It has been suggested that the stability of the spinel-type structure ($LiCo_2O_4$) with Li occupying 8a tetrahedral sites, is actually greater than either cubic or layered forms in the intermediate Li content range, and the kinetic barrier for Li and Co migration between octahedral sites is a small penalty for enhanced stability(*82*). The connection between the electrochemistry of $LiCoO_2$ in non-aqueous battery electrolytes versus oxygen evolution catalysis in aqueous electrolyte will be discussed in more detail below, as the subject of this study.

The origin and nature of the structural transformation of the layered $LiCoO_2$ and the absence of it for cubic $LiCoO_2$ during electrocatalysis in aqueous electrolyte is described herein. The outcome is the formation of a highly active catalytic phase present in both materials, namely, spinel $LiCo_2O_4$. The spinel $LiCo_2O_4$ and cubic $LiCoO_2$ retain the same cubic space group built upon $[Co_4O_4]^{n+}$ cubane subunits, unlike layered $LiCoO_2$. We report different intrinsic electrocatalytic water oxidation activities of the two polymorphs of $LiCoO_2$, and demonstrate performance approaching that of Iridium nanoparticles, the best membrane-based OER catalyst to date.

2.2.2 Experimental

Synthesis of lithium cobalt oxide nanoparticles: Both cubic and layered-rhombohedral lithium cobalt oxides were synthesized via a previously reported sol-gel procedure (summarized in section 2.1.2 above)(*31*, *68*). Briefly, nitrate salts of the metals were mixed in stoichiometric amounts and dissolved in an aqueous solution with citric acid and urea. The solution was stirred and evaporated to form a gel at 80 °C, dried overnight at 170 °C to form the xerogel polymerized intermediate, and then crushed and calcined at 400 °C (denoted **LT**) or 700 °C (denoted **HT**) for 4 hours to form the final crystalline products. These are designated as LT-$LiCoO_2$ and HT-$LiCoO_2$. Co_3O_4 was also synthesized as a control with the same method, but leaving out the $LiNO_3$. The product morphology and crystallinity were confirmed by powder X-ray diffraction (PXRD) and scanning electron microscopy (SEM). We purchased 20% Ir@C (vulcanized carbon) from Premetek.

Electrochemical Measurements: The electrode configuration used for studying the electrochemistry of $LiCoO_2$ and 20% Ir@C was a film formed by drop-casting an ink of catalyst and conductive carbon suspended with Nafion® polymer as binder onto a homemade glassy carbon electrode (5 mm diameter, custom made, HTW SIGRADUR G GC rod affixed in a G-10 Garolite Rod). The inks were 12 mg/mL catalyst for LT-$LiCoO_2$, 42 mg/mL for HT-$LiCoO_2$, 25% by mass conductive carbon (acetylene black, STREM Chemicals), and 0.67% by mass neutral Nafion. The Nafion was cation exchanged with 0.1 M NaOH to neutralize the acid functional groups as described in earlier work(*33*, *83*). Catalyst loading was between 0.2-1.2 mg/cm^2 for electrochemical measurements. Higher loading was used for HT-$LiCoO_2$, as it was determined to have ~3

fold lower surface area than LT-$LiCoO_2$ based on BET N_2 adsorption(*68*). A cross-sectional view of the catalyst films was prepared by drop-casting the ink used to make working electrodes onto an ITO-coated glass slide. The slide was scored and snapped across the film to create a cross-sectional view, which was examined by SEM. For long-term stability measurements, electrode pellets made of catalyst, carbon, and PVDF were constructed, as the Nafion-based film is unstable to bubble degradation over time. The pellet composition was 75% catalyst, 7.5%` acetylene black, 7.5% graphite, and 10% polyvinylidene fluoride (PVDF) – average pellet weight was 6 mg. Pellets were pressed at 100,000 psi for 30 min and vacuum dried at 140 °C overnight(*84*). A back contact to a Ti foil was made with a small amount of silver paint, and the whole electrode was sealed with epoxy. We tested activity in both neutral (1 M Phosphate buffer, NaH_2PO_4 and K_2HPO_4 Sigma-Aldrich, ACS reagent, ≥98%), and basic (1 M NaOH, pellets, Sigma-Aldrich, reagent grade, ≥98%) conditions. Experiments were typically performed in a two-chamber cell separated by a glass frit with vigorous stirring. The reference electrode used in alkaline electrolyte was Hg/HgO (1 M NaOH, 0.140 V vs NHE) from CHI, and in neutral electrolyte a homemade Ag/AgCl (sat'd KCl, 0.200-0.235 V vs NHE) calibrated against NHE. Counter electrodes were either boron-doped diamond or titanium mesh. Cyclic voltammetry (CV's) were performed at varying scan rates (between 5-200 mV/sec) to generate the various curves shown below – either polarization curves for catalyst activity, or scan-rate dependence scans to obtain double-layer capacitance values. In addition, chronopotentiometry was performed at 1 and 10 mA/cm^2. The long-term stability was examined for the pellet electrodes by conducting chronopotentiometric experiments over 14 hours at 10 mA cm^{-2}.

Faradaic efficiency in basic solution was measured for each catalyst by gas chromatography (Perkin Elmer Clarus 680 GC with TCD detector, Ar carrier gas, operating at 40ºC). We used a two-electrode setup sealed in a custom made multiport electrochemical cell with a known headspace and electrolyte volume, as previously described(*85*). Cells were purged with Ar for 30 minutes, followed by a chronopotentiometric experiment at 10 mA cm^{-2} in 1 M NaOH for 2 hours. All 3 samples were performed in triplicate, with 200 μL samples taken from the headspace.

Transmission electron microscopy: Samples used for high-resolution transmission electron microscopy (HRTEM) were pristine powders of cubic and layered $LiCoO_2$ synthesized by the aforementioned sol-gel method. For HRTEM analysis of "post-catalysis" samples, a modified procedure for electrochemical tests had to be used to avoid interference in the analysis by carbon and Nafion. These samples were prepared by dispersing only the catalyst onto a titanium grid with which we conducted chronopotentiometry at 1 mA cm^{-2} for 1 hour in 1 M NaOH. The Ti meshes were then sonicated in a small amount of ethanol and the suspensions were dispersed onto lacey carbon TEM grids. A JOEL 2010F TEM/STEM with EDS and EELS attachments was used for the high-resolution (HRTEM) and selected area electron diffraction (SAED) microscopy observations. The scope is operating at 200 KeV with resolution better than 1.5 Angstrom in both imaging and scanning modes. Analysis of images was performed with Gatan Digital Micrograph, accompanied by the Difftools package(*86*).

Corrosion Analysis: The (electro)chemical leaching of lithium was monitored by inductively-coupled plasma optical emission spectroscopy, on a Perkin Elmer Optima 7300 ICP-OES. Chronopotentiometry at 10 mA cm^{-2} was performed with drop-casted

film electrodes for 2 hours, and the resulting electrolyte was analyzed for trace metals (e.g. Li, Co, Ni, Mn). The electrolyte volume was kept small (8 mL), and 1 mL aliquots were pulled through syringe filters at 30 minute intervals during the course of the experiment, and acidified with HNO_3. Standard series (250 ppb, 500 ppb… 5 ppm 10 ppm) were prepared from standards purchased from SPEX Certiprep for Mn, Co, Ni, and Li.

Catalyst Performance in AEMWE: The performance of cubic $LiCoO_2$ as an anode catalyst for alkaline exchange membrane water electrolysis was tested in a single stack configuration and compared to a benchmark PGM AEM cell. A non-proprietary 25cm^2, non-pressurized stack was used for short term testing and a proprietary 28cm^2 differential pressure capable cell stack (previously reported(*87*)) for long term unattended operation. The anode (IrO_x baseline or $LiCoO_2$) or cathode (Pt black) catalysts were airbrushed onto a stainless steel (anode) or carbon (cathode) Gas-Diffusion Layers (GDLs) at a loading of 2-3 mg/cm^2 in a polymeric ink vehicle. The operating conditions for the 25cm^2 tests were 50 °C, with 0 psi H_2 back pressure with DIW feed on the anode side (polarization curve). The operating conditions for the 28cm^2 tests were 35-50 °C, with 50 psi H_2 back pressure, the stack was fed deionized water with 1% $KHCO_3$ (for long-term stability).

2.2.3 Results

Morphology and Crystallinity: The morphology and crystallinity of the metal oxides were examined by SEM/TEM, and powder x-ray diffraction (PXRD), respectively. It was confirmed that the as-synthesized materials had nanoparticulate morphology, with a range of particle sizes (**Figure 2.11 and 2.12**). The PXRD patterns for each catalyst

match well with the standards, with the expected splittings at 38 and 65° 2θ at higher temperatures, signifying the formation of layered $LiCoO_2$. Low-temperature $LiCoO_2$, synthesized at 400 °C, crystallizes in a cubic phase (Fd-3m) where Co and Li are at octahedral 16d and 16c sites, respectively. The particles were generally spherical with diameters between 20-100 nm. High-temperature $LiCoO_2$, synthesized at 700°C, crystallizes in a layered rhombohedral form (R-3m) with alternating octahedral layers of Li-O and Co-O. Co and Li occupy 3a and 3b sites, respectively. The particle size was noticeably larger, but still nanoscopic, with generally more flattened crystallites ranging between 50-150 nm. Both phases have the same oxide sublattice and differ only in cation ordering. These morphological and structural properties are consistent with our previous work using the same synthetic procedure(*68*).

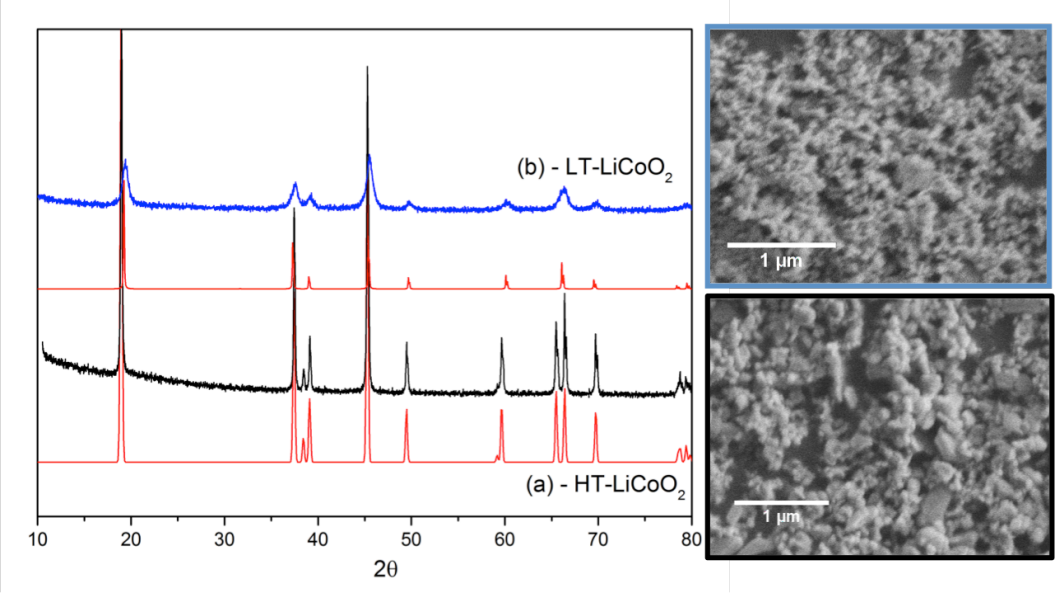

Figure 2.11 PXRD patterns (with standards) of low-temperature cubic LT-$LiCoO_2$ (blue), and high-temperature layered HT-$LiCoO_2$ (black), with SEM images of particle morphology to the right.

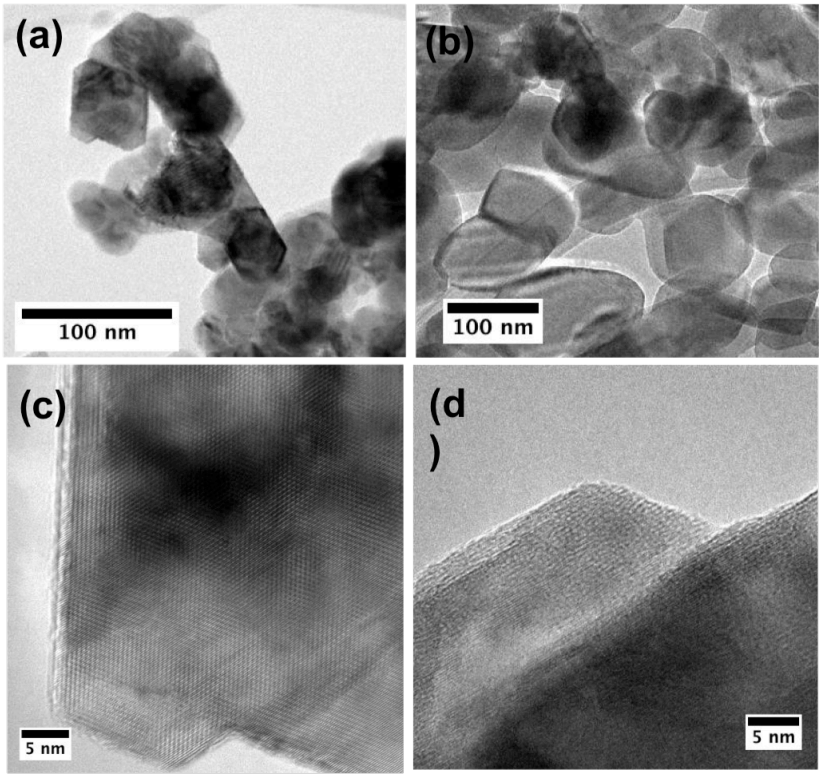

Figure 2.12 TEM and high-resolution images of as-prepared (a and c) LT-$LiCoO_2$ and (b and d) HT-$LiCoO_2$.

Because PXRD reflects bulk composition and the patterns are so similar to one another, some layered phase may begin to form and be present in the low-temperature sample (<2% limit of detection). TEM performed on pristine samples of both low- and high-temperature synthesized $LiCoO_2$ demonstrates a highly crystalline single phase product extending from the interior to the surface of all nanoparticles. There are well-faceted crystallites that are generally smaller and more spherically symmetric in cubic, than in layered $LiCoO_2$, which are more elongated. Additional HRTEM studies corroborated the phase purity of the as-prepared sample (**Figure 2.12 and 2.13**). The lattice fringes are clearly visible and continuous from the interior of the particles to the edge. The reflections seen in the fast-fourier transforms (FFT) correspond to the 111 and 003 planes of LT and HT-$LiCoO_2$, respectively. We designate these two samples by their synthesis temperatures, as *LT* and *HT* $LiCoO_2$, respectively.

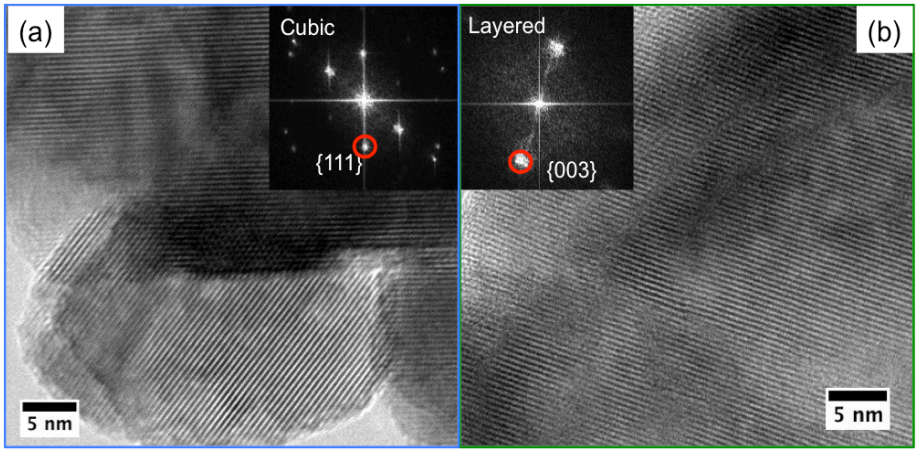

Figure 2.13 HRTEM images of pristing (a) LT-$LiCoO_2$ and (b) HT-$LiCoO_2$. The lattice fringes match those of the 111 (4.6 Å) and 003 (4.7 Å) planes respectively.

OER Electrocatalytic Activity: The electrochemical activity of cubic and layered $LiCoO_2$ is illustrated for both basic and neutral conditions. The figures of merit important for OER catalysis are given in **Table 2.2**. We normalized the loading of electrocatalyst to the surface area obtained from N_2 gas absorption (BET) as this eliminated possible artifacts from diffusion limitation of reactants and products. For control, the electrocatalytic activity of 5 nm iridium nanoparticles on Vulcan carbon (20%) (Premetek) is reported as well.

The working electrode film containing catalyst was characterized by cross-sectional SEM (**Figure 2.14**), and it was determined to be 5-10 μm thick. There is substantial porosity, but also very uniform dispersion of catalyst, binder, and carbon, with no distinguishable segregation of any component. The average polarization curves for each sample are shown in **Figure 2.15**. They were generated by averaging the forward and reverse sweeps of slow scan rate cyclic voltammograms (iR corrected, 10 mV sec^{-1}). 20% Ir on carbon performed the best in both neutral and basic conditions, with specific activity and Tafel slope values matching closely those reported in the literature(*43*, *88*)

(**Table 2.2**). Both phases of $LiCoO_2$ show highest activity in alkaline solution, and substantial decreases in activity in phosphate buffer at pH 7. This non-Nernstian behavior is typical of first-row transition metal oxide catalysts, and indicates a larger activation energy at pH 7 relative to alkaline pH. In base, LT-$LiCoO_2$ exhibits mass specific activity of ~5 A g^{-1} (η = 400 mV), with a Tafel slope of ~48 mV dec^{-1}. **Figure 2.16** shows that HT-$LiCoO_2$ deactivates from its initial state in ~200 s. Once in steady state it has a Tafel slope value ~49 mV dec^{-1} and mass activity of ~2 A g^{-1}.

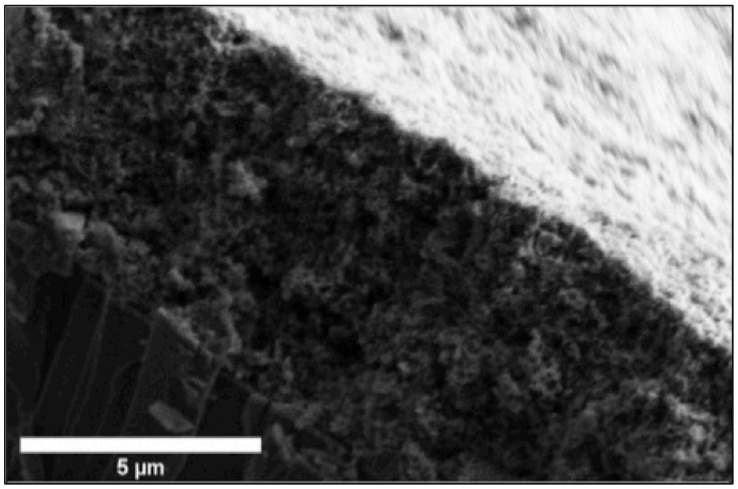

Figure 2.14 Cross-sectional SEM of catalyst composite films (on ITO glass) used to test electrochemical activity. The view is tilted slightly, with the bottom left-hand corner showing the underlying glass substrate, the dark rough portion illustrating the cross-section, and the lighter portion being the top of the film. Film thickness is ~5-10 µm.

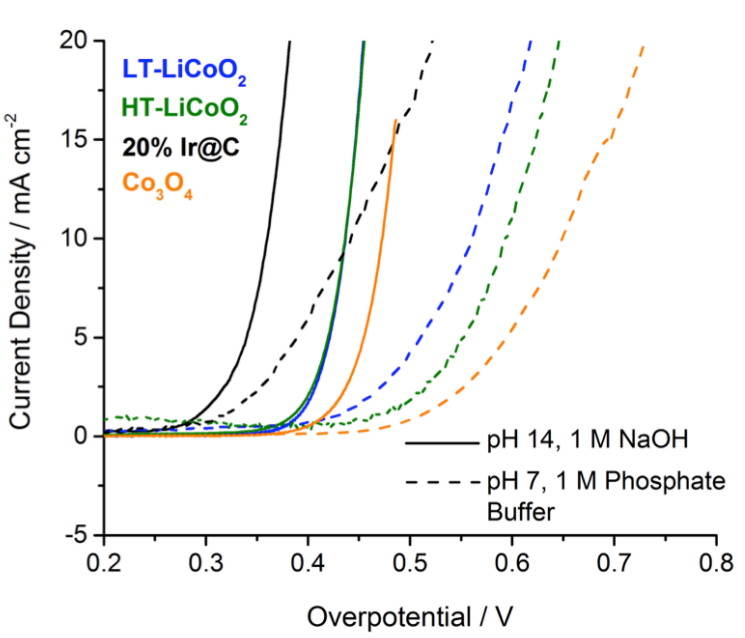

Figure 2.15 Averaged cyclic voltammograms of electrocatalysts in this study in pH14 (1 M NaOH), and pH 7 (1 M NaH_2PO_4/K_2HPO_4). Curves are capacitance corrected by averaging the forward and reverse sweeps, as well as iR-corrected. The HT- and LT-$LiCoO_2$ curves are almost superimposed in alkaline solution.

The cyclic voltammograms (CV) of pristine LT- and HT-$LiCoO_2$ electrodes are presented in **Figure 2.17**, which highlights their different redox features below the water oxidation wave. The layered HT-$LiCoO_2$ CV shows more complex features and a much higher yield for the $Co^{3/4+}$ peak in both neutral and alkaline conditions. This has been previously ascribed to both lithium removal into electrolyte and Li reordering within the surface/bulk(*89*). However, both materials show marked decreases in the non-OER redox peaks after only one cycle, indicating some irreversible process occurring upon oxidation.

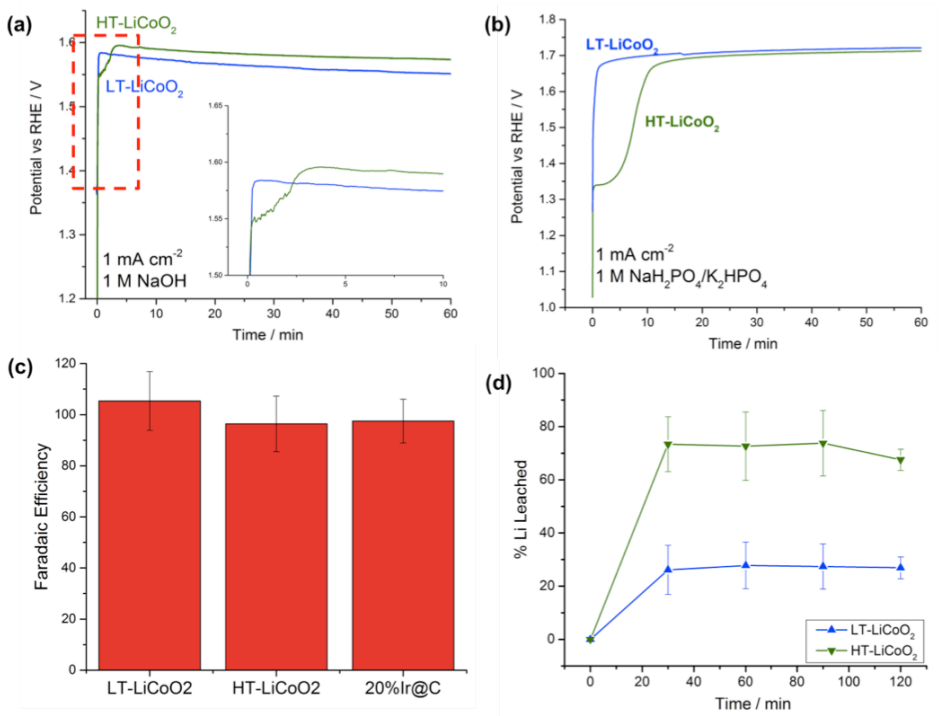

Figure 2.16 Comparison of the operating potential at 1 mA cm^{-2} for HT- and LT-$LiCoO_2$ at pH 14 (a) and at pH 7 (b). Inset in (a) shows initial inflection showing potential change associated with Li deintercalation/water oxidation for HT-$LiCoO_2$. (c) Faradaic efficiency (O_2 yield) measured from 2 hour experiments at 10 mA cm^{-2} (**Figure 2.19**). (d) Li leaching data over the course of 2 hour 10 mA cm^{-2} experiments plotted as % of starting Li.

To quantify this electrochemical/charging effect, we measured the scan rate dependence of the double layer capacitance (C_{dl}) for both materials below the OER potential (**Figure 2.18**). The values obtained are 2.5 mF for LT, and 11 mF for HT-$LiCoO_2$. These values reflect differences in access to the electrochemically active material. The greater capacitance of layered $LiCoO_2$ is known to be due to its larger accessible volume for Co oxidation and Li deintercalation(*90*, *91*). This outcome is also consistent with the larger pre-OER peaks in the CV's. This will be discussed further with respect to the Li leaching data presented below.

In order to understand how the catalytic activity changes over time we performed chronopotentiometric experiments at 1 and 10 mA cm^{-2}. The 1 mA cm^{-2} traces for both LT- and HT-$LiCoO_2$ in alkaline and neutral solution are shown in **Figure 2.16a,b**. Most

visibly, in the 1 mA cm^{-2} trace, pristine electrodes of HT-$LiCoO_2$ undergo a ~3 minute activation process. Instead of the typical logarithmic potential rise to steady-state expected for chronopotentiometry, there is an inflection indicative of another possible reaction taking place. After this time point it starts to drop, and very nearly approaches the same overpotential as for LT-$LiCoO_2$. At pH 7, the same behavior is seen; LT-$LiCoO_2$ is immediately active compared to an even longer (10 min) lag phase for HT-$LiCoO_2$ **(Figure 2.16b)**. This activation phenomenon is also observed on the 10 mA cm^{-2} traces over a much shorter time scale and, at that current density, the two polymorphs maintain the same overpotential (within error) over the 2-hour time scale (**Figure 2.19**). Attempts to separate the intrinsic O_2 evolution activity of nascent HT-$LiCoO_2$ from the electrolytically driven capacitive charging before appreciable Li^+ deintercalation and phase change were unsuccessful.

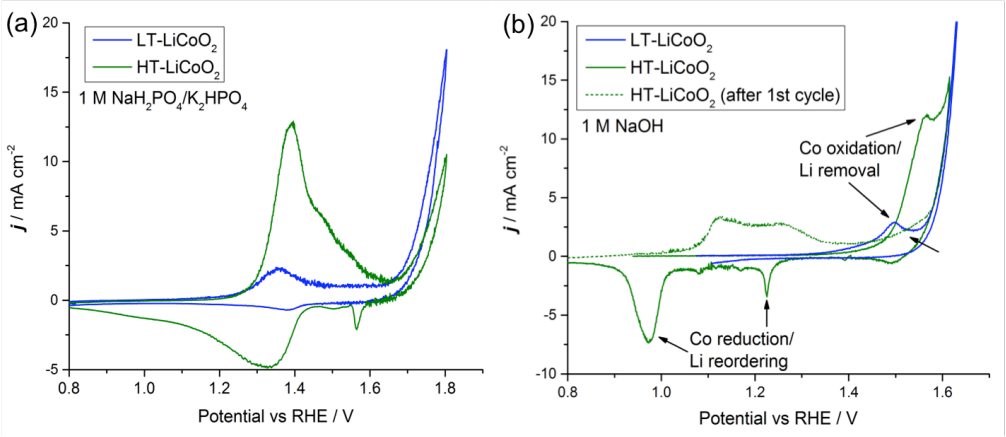

Figure 2.17 Cyclic voltammograms (10 mV sec^{-1}) of LT and HT-$LiCoO_2$ in (a) pH 7 and (b) pH 14. Both illustrate distinct redox features before the onset of OER associated with $Co^{3+/4+}$ oxidation and lithium removal/ordering, and in both cases the features diminish in yield on the cathodic sweep, suggesting irreversible chemical change.

Figure 2.19 also shows a comparison to the control, 5 nm particles of Ir@C, which exhibits a 100 mV lower overpotential at 10 mA cm^{-2}. As the overpotential can be particle size dependent, we compared the specific activity normalized to catalyst surface

area in **Table 2.2**. This shows that following restructuring HT- and LT-$LiCoO_2$ (100 nm and 50 nm, respectively) have the same specific activity and this is about 10-20 fold lower than 5 nm Ir@C.

Table 2.2 Summary of OER catalyst metrics for $LiCoO_2$ catalyst/ionomer films and AEM electrolyzer. The numbers for Ir are given for comparison.

Sample (particle size)	BET surface area, $m^2 g^{-1}$	Cat. Loading mg/cm^2 electrode	pH[a]	Tafel Slope, $mV\ dec^{-1}$	η @ 10 $mA\ cm^{-2}$	Mass Activity, $A\ g^{-1}$ (η=400 mV)	Surface Activity $A\ m^{-2}$ (η=400 mV)	% O_2 Faradaic Efficiency, pH 14	AEMWE Cell Potential (400 $mA\ cm^{-2}$)[d]
LT-$LiCoO_2$ 20-100 nm	56	0.32	7	75 ± 11	570 ± 12	2.32	0.041[b]	105 ± 11	1.91 V
			14	48 ± 3	430 ± 14	5.24	0.094		
HT-$LiCoO_2$ 50-150nm	14	1.2	7	81 ± 6	588 ± 27	0.39	0.028[b]	96 ± 11	n/a
			14	49 ± 3	430 ± 8	1.71	0.12		
20% Ir @C 5 nm	80[c]	0.21	7	61 ± 9	460 ± 13	29.1	0.36	98 ± 9	2.22 V
			14	40 ± 8	330 ± 4	151.2	1.89		

(a) Electrolytes: pH 7 = NaH_2PO_4/K_2PO_4, pH 14 = 1 M NaOH
(b) Amps (Cat surface area)$^{-1}$ following surface reconstruction.
(c) 5 nm Ir specific surface area (Premetek)
(d) Values obtained from Polarization Curve (Figure 2.25a), Pt cathode catalyst

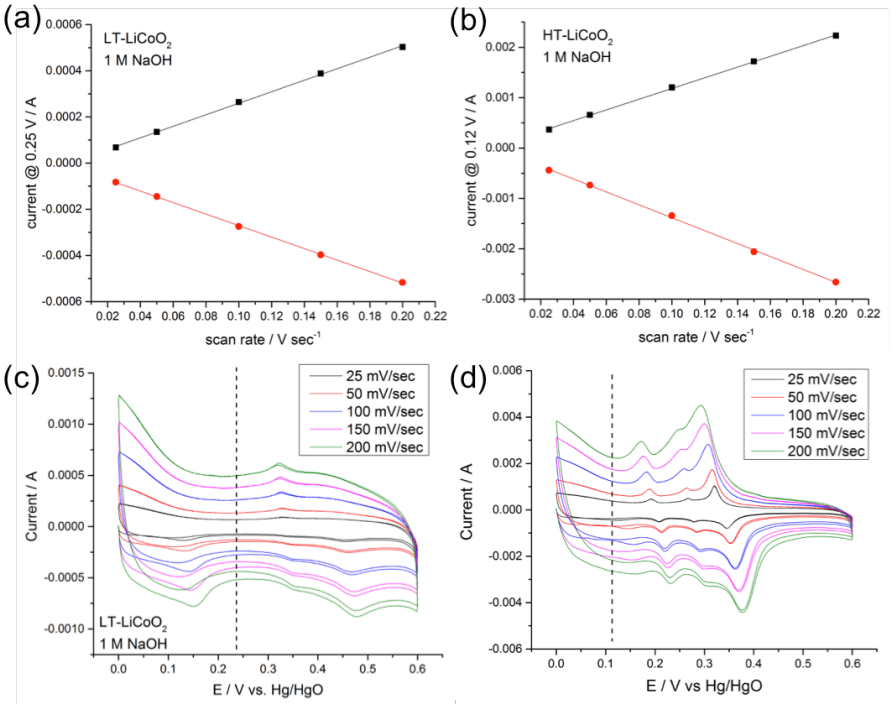

Figure 2.18 Scan rate dependence of capacitive current for (a and c) LT and (b and d) HT-$LiCoO_2$ in base. The C_{dl} values extracted from the slopes of the lines in (a) and (b) are 2.5 and 11 mF for LT and HT, respectively. Dotted line indicates region where non-Faradaic current is used for scan-rate dependence plots above.

Faradaic efficiency: Important to any catalysis is the measurement of products, and we have measured the Faradaic yield of oxygen using gas chromatography (See **Figure 2.16c** and **Table 2.2**). Within expected error due to crossover reduction of O_2 and the inherent sensitivity limits for the technique, the samples all yield high, nearly 100% Faradaic efficiency over the course of two hour 10 mA cm^{-2} experiments.

Corrosion analysis: Since both polymorphs of lithium cobalt oxide have been established as intercalation compounds, we decided to analyze the electrolyte solutions of the chronopotentiometric experiments. We used ICP-OES to quantify lithium or cobalt ions that may have leached during the electrolysis. The results are presented in **Figure 2.16d**. Although we did not see any Co in the electrolyte, we did see significant amounts of Li. We found that ~30% of the original Li content in the LT sample had been removed and ~70% of that in HT-$LiCoO_2$. The results are consistent with the observed larger measured C_{dl} for HT-$LiCoO_2$. The layered phase is the more easily delithiated compound, because of the lability of Li. For both materials, after an initial period of activation, no further Li removal is observed, indicative of a stable endpoint for catalyst composition.

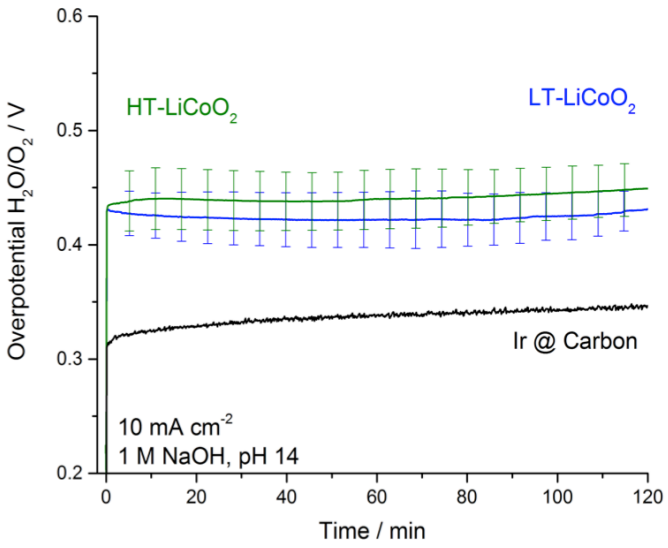

Figure 2.19 Chronopotentiometry of HT and LT-$LiCoO_2$ at 10 mA cm^{-2} in 1 M NaOH as compared to Ir nanoparticles. Experiments used for Faradaic efficiency and Li corrosion.

Surface analysis by HRTEM: To monitor atomic structure following catalysis, we performed HRTEM analysis on the two $LiCoO_2$ polymorphs before and after being subjected to prolonged electrolysis at 1 mA cm^{-2}. Because the layered polymorph of lithium cobalt oxide has previously been shown to undergo surface restructuring during charge/discharge cycling in battery applications, we decided to conduct this type of analysis for both LT and HT-$LiCoO_2$ samples in OER electrolytic conditions. The results for the high-resolution images are shown in **Figure 2.20** and the selected area electron diffraction patterns (SAED) are shown in **Figure 2.21**.

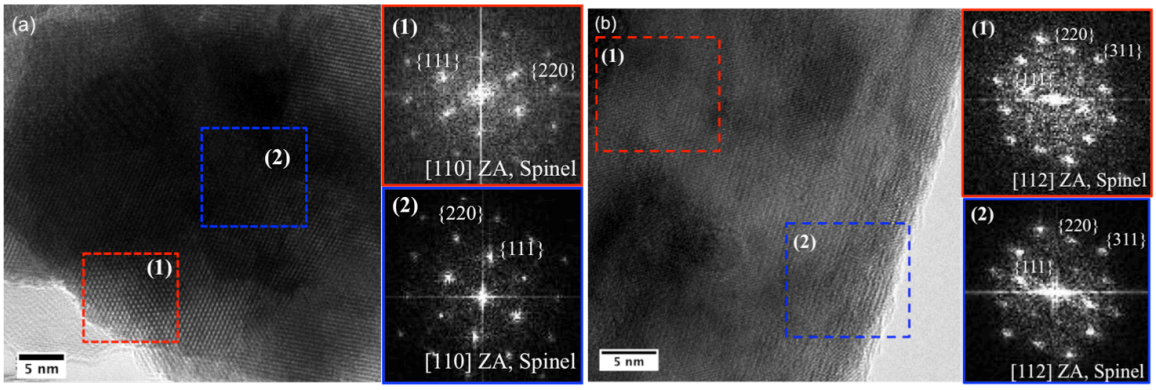

Figure 2.20 HRTEM images of (a) LT-$LiCoO_2$ and (b) HT-$LiCoO_2$ after electrolysis in 1 M NaOH at 1 mA cm^{-2}. The FFT patterns from both the interior and edges of the particles indicate presence of spinel $LiCo_2O_4$ phase. The 220, 111, and 311 peaks of Fd-3m cubic spinel phase are indicated. Interior of HT-$LiCoO_2$ (region 1) also has some reflections attributable to remaining layered phase.

Both "post-catalysis" $LiCoO_2$ samples have nanocrystallite morphology, exhibiting well-defined lattice fringes in both the bulk and surface of the particles examined. LT-$LiCoO_2$ has smaller crystallite domains, as indicated by the difference in SAED patterns – rings, as opposed to spots seen in the HT-$LiCoO_2$ pattern (**Figure 2.21**). In the analysis of the HRTEM images, we took the Fast-Fourier Transform (FFT) from different regions of the post-catalysis particles. We found that for both samples, the patterns are best ascribed to a cubic phase of $LiCoO_2$ (**Figure 2.20**), specifically viewed along the [110] and [112] zone axes (ZA). Importantly, we see reflections originating from the 220 plane for both materials, indicative of Li occupancy at tetrahedral sites(*29*). The peak was not assignable to Co tetrahedral site occupancy (Co_3O_4 spinel) based upon the d-spacings and the generally weaker intensity. In addition, XPS of the post-catalysis samples reveals broadening of the $Co2p_{3/2}$ peak to higher binding energy, consistent with the increased oxidation state expected for a delithiated sample (**Figure 2.22a**)(*92*). It is also apparent that the phase transformation in the case of HT-$LiCoO_2$ extends beyond just the first few layers since the FFT pattern from the interior matches well that from the surface. Even

particles that had obvious phase transitions show thick (>5 nm) layers of reconstructions (**Figure 2.23**).

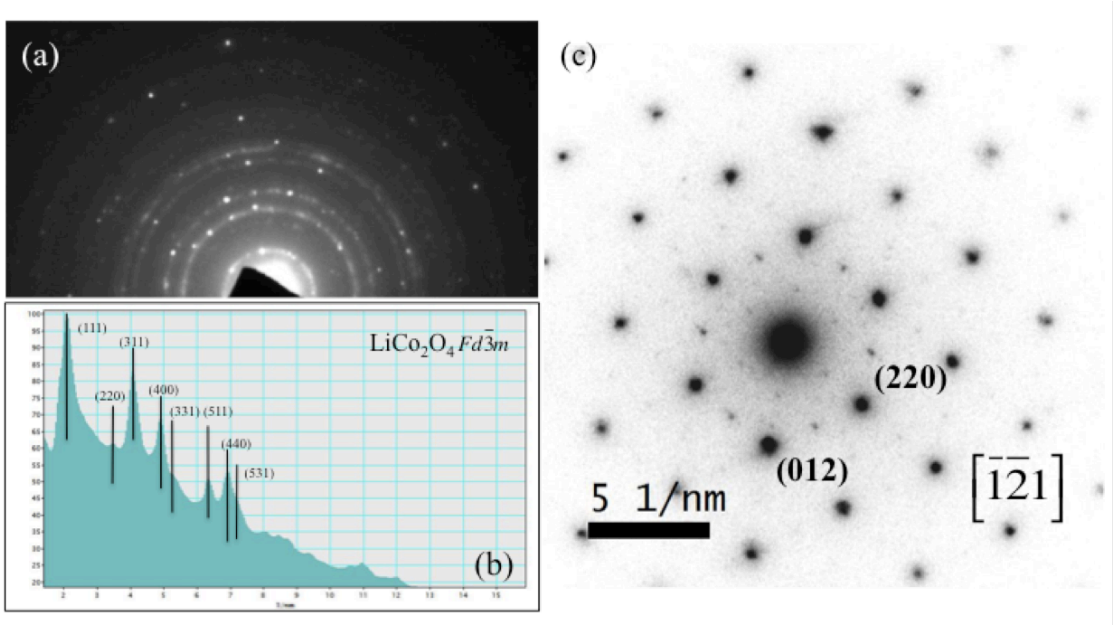

Figure 2.21 Selected area electron diffraction (SAED) analysis of (a) and (b) LT- and (c) HT-$LiCoO_2$ after electrolysis @ 10 mA cm^{-2} for 2 hours. The more nanoscrystalline LT-$LiCoO_2$ shows rings which can be rotationally averaged to yield the pattern in panel (b) that is indexed to spinel $LiCo_2O_4$ in cubic space group. In the case of HT-$LiCoO_2$, the main pattern is indexed to hexagonal $LiCoO_2$ ZA [-1-21], but faint reflections from the cubic spinel phase, including the 220 reflection are observed. (labels are on the lower right side of reflections).

For long-term electrolysis stability tests, a different electrode configuration was employed to avoid failure due to film instability. The drop-cast films are only transiently stable, and can peel off or oxygen bubbles can block the surface, leading to false indications of catalyst instability during cycling or fixed electrolysis experiments (**Figure 2.24**). Instead, we used a pellet electrode made from the catalyst embedded in epoxy to conduct 14-hour experiments at 10 mA cm^{-2}. The results, given in **Figure 2.24**, show that both HT and LT-$LiCoO_2$ are long-term stable in basic and neutral electrolyte.

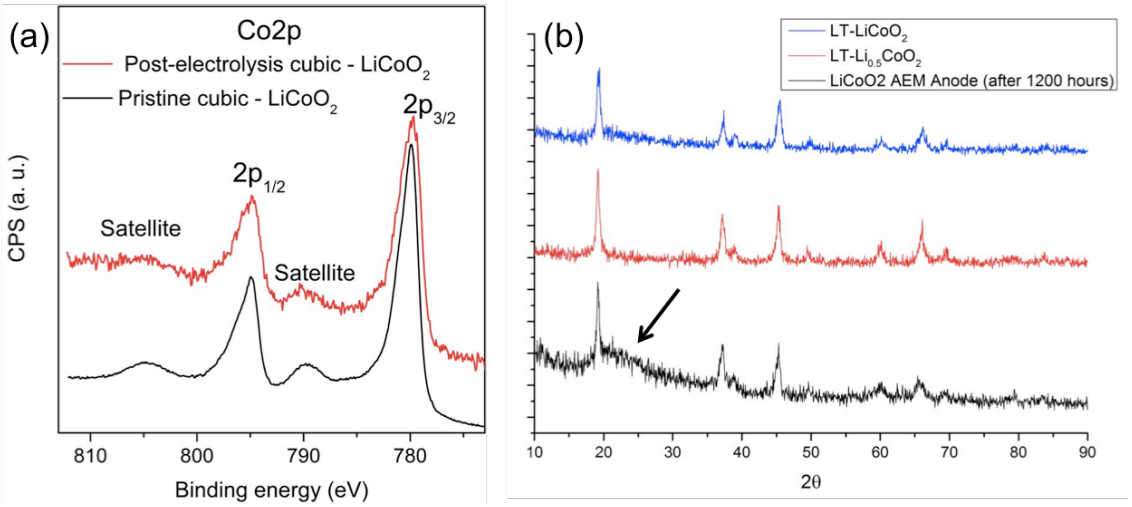

Figure 2.22 (a) Co 2p XPS spectra of cubic $LiCoO_2$ and (b) PXRD patterns of LT-$LiCoO_2$ (along with pristine sample and chemically-delithiated spinel $LiCo_2O_4$) before and after anodic electrolysis in the alkaline MEA electrolyzer that had been running for >1000 hours

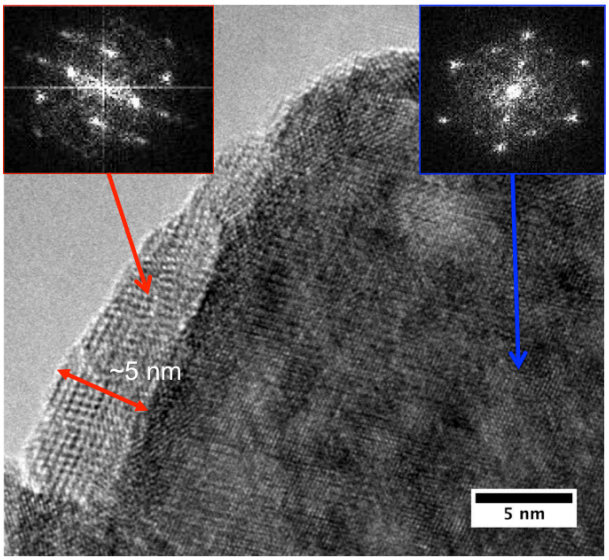

Figure 2.23 HT-$LiCoO_2$ particle post reaction. The interior particle shows layered phase still intact, but exterior edge has thick (5 nm) zone of reconstruction (insets show FFT patterns)

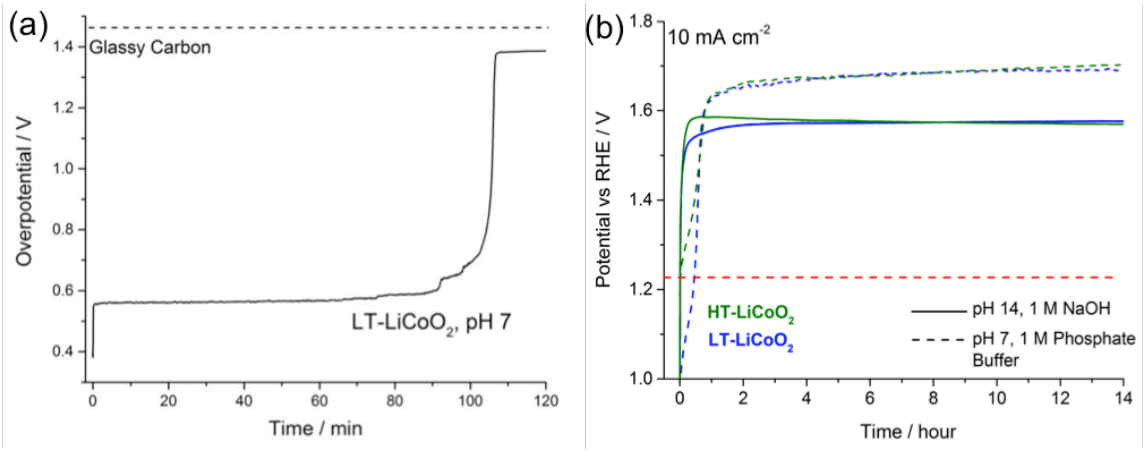

Figure 2.24 (a) Chronopotentiometry of LT-$LiCoO_2$ catalyst film containing Nafion® illustrating instability caused by film delamination over prolonged electrolysis at 10 mA cm^{-2} due to bubble formation. (b) Overnight stability @ 10 mA cm^{-2} on pellet electrodes shows catalyst stability over the normal lab scale long-term stability. Dashed red line is thermodynamic limit.

2.2.4 Discussion:

Pristine HT-$LiCoO_2$ (layered) and LT-$LiCoO_2$ (cubic) exhibit distinctly different OER electrocatalytic activity and electrochemical responses, confirming that these structurally distinct compounds of identical composition have electronically distinct Co environments and inherently different rates for water oxidation. However, upon close inspection of the surface structure with HRTEM, a structural convergence between the two phases occurs upon Li removal and oxidation of the bulk, which produces the spinel $LiCo_2O_4$. Starting from cubic $LiCoO_2$, this transformation requires relatively minor rearrangement of the remaining Li^+ cation from octahedral to tetrahedral site at the four O corners of the cubane $[Co_4O_4]^{4+}$. The same cubic cobalt oxide sublattice is shared by cubic $LiCoO_2$ and spinel $LiCo_2O_4$ phases. The cubic phase can tolerate the electron loss associated with oxidation/OER catalysis without large structural rearrangement of the Co-O sublattice. By contrast, layered $LiCoO_2$ is built around incomplete cubanes, $[LiCo_3O_4]^{2+}$, and requires major rearrangements to form the stable spinel phase.

As established for lithium ion batteries, layered $LiCoO_2$ has the ideal structure type for facile cation deintercalation(*35*, *93*, *94*). However, multiple reports(*27*, *28*, *82*) have now established that the relative thermodynamic stability of layered $LiCoO_2$ is affected by lithium removal and Co oxidation and thus the structure can become kinetically determined. These phenomena have been mostly observed in organic electrolyte(*29*, *80*) (ethylene/propylene carbonate) and partly in aqueous electrolyte when used for oxygen evolution reaction catalysis(*75*, *77*). It is observed in the majority of cases that after overcharging or repeated cycling, layered $LiCoO_2$ particles have substantial surface and subsurface restructuring, with the resulting phase being assigned to either spinel $LiCo_2O_4$ or cubic $LiCoO_2$. This leads to degradation in performance. In support of this finding is the observation that the low-temperature synthesized cubic $LiCoO_2$ and delithiated Li_xCoO_2 ($0<x<1$) have poorer performance as intercalation compounds, with a lower amount of extractable Li and higher operating voltages with multiple voltage plateaus. In fact, with lithium extraction it is observed that some O_2 is liberated and the transformation of layered to spinel is assisted by such a reaction(*29*, *34*, *95*). By comparison, we observe, in aqueous electrolytes under electrolytic O_2 evolution conditions, removal of 70% of the Li content from HT-$LiCoO_2$ in conjunction with the formation of the spinel phase at the surface and partly in the interior, where the stoichiometry at the bulk level is close to $Li_{0.3}CoO_2$. XPS also shows broadening of the $Co2p_{3/2}$ peak toward greater binding energy, indicative of higher valence of Co. The resulting phase is an active and compositionally stable catalyst nearly mirroring that which forms from LT-$LiCoO_2$, in which less than half as much Li can be removed, and its starting structure is already a more active catalyst than HT-$LiCoO_2$.

Theoretical calculations have predicted that for Li_xCoO_2 ($0 \leq x \leq 1$) at intermediate lithium compositions (i.e. $Li_{0.5}CoO_2$), the thermodynamically favored structure is the spinel $LiCo_2O_4$, where Li would migrate to tetrahedral sites and 25% of the Co would be in the Li layers(*82*, *96*). We observe that this is the preferred structure that forms during OER catalysis, evidenced both by the structural change and by the loss of Li content.

A minimal requirement for catalysis of O_2 evolution from water by these materials is oxidation of Co^{3+} to Co^{4+} at a potential at or above eqn (1a) or (1b). Recent electronic structure calculations along with *in situ* X-ray spectroscopy have shown that the process of Li deintercalation from layered $LiCoO_2$ is charge balanced by not only $Co^{3/4+}$ oxidation, but also electron loss from a lower lying oxide band in the most highly charged samples of $LiCoO_2$(*97*, *98*). Some reports suggest that this larger intermixing of Co 3d states and O 2p states yields higher conductivity and that is the source of greater OER activity(*69*, *78*). This condition alone is insufficient for the four-electron concerted oxidation reaction. We suggest an alternative explanation.

By comparison, among molecular Co oxide clusters, it has been found that only in molecules containing $[Co_4O_4]^{4+}$ cubes is the Co^{4+} oxidation state accessible at reasonable potentials, while the di- and tri-nuclear analogues (containing $[Co_2O_2]^{2+}$ and $[Co_3O_4]^{+}$ cores, respectively) cannot be oxidized in this same window (> 1 V difference) and actually decompose at higher potentials where water oxidation by cubanes begins(*99*). The explanation for the accessible potential of $[Co_4O_4]^{4+/5+}$ is due to resonance delocalization of electron holes around the cube, as established by ESR spectroscopy which found comparable spin density on Co *and* O centers(*100*). Among these molecular

Co clusters only the cubes were found to be active water oxidation catalysts at potentials just above the $[Co_4O_4]^{4+/5+}$ couple(*99*, *101*).

Taken together with the observations of this study, it is apparent that the individual cubical $[Co_4O_4]^{4+}$ core, such as present in cubic $LiCoO_2$, spinel $LiCo_2O_4$ and molecular clusters provides exceptional energetic stabilization of the HOMO which facilitates oxidation from electronic levels comprised of mixed O 2p and Co 3d(t_{2g}) orbitals. This stabilization arises from hole delocalization in the symmetrical cube that is absent in incomplete cubes comprised of $[Co_3O_4]^{+}$ cores and in layered $LiCoO_2$ where $[LiCo_3O_4]^{2+}$ incomplete cubes exist. Instead, hole delocalization in layered $LiCoO_2$ occurs macroscopically within the individual CoO layers, due in part to favorable entropy. Macroscopic charge delocalization is necessary for charge storage devices such as batteries, but detrimental to water oxidation catalysis which requires concerted four-electron oxidation and O-O bond formation localized on two water molecules bound to one or two adjacent Co centers. These considerations rationalize the distinct catalytic performance of the two polymorphs of $LiCoO_2$.

Validation of the unique water oxidation capability of the cubical metal-oxo cluster motif has been verified across multiple examples of molecular(*99*, *102–104*) and solid-state transition metal-oxo compounds(*14*, *68*, *105*). Prediction of this potential originated from consideration of the water oxidation site found in photosynthetic organisms where a similar core type is found(*30*).

Finally, to test actual commercial relevance, we have tested whether the observed activity in a flooded electrochemical cell can be realized in a solid electrolyte membrane-based electrolyzer stack, where operating current densities far exceed those normally

probed at the lab scale. In **Figure 2.25a**, the polarization curve of a cell using cubic $LiCoO_2$ as the anode catalyst illustrates higher electrochemical efficiency than a cell using an iridium oxide catalyst at comparable loading. This performance improvement extends up to 500 mA/cm^2 (at least), and the activity is reproducible across different batches of catalyst. **Figure 2.25b** shows the operation of such a cell at various current densities for 1000 hours without failure. The Co2p XPS and the PXRD of sample gathered from the anode after electrolysis presented in **Figure 2.22a,b** are additional proof of catalyst durability. These experiments demonstrate that the $LiCoO_2$ is a highly efficient and robust catalyst for alkaline water electrolysis and has potential for displacement of noble metal catalysts used in commercial electrolyzers.

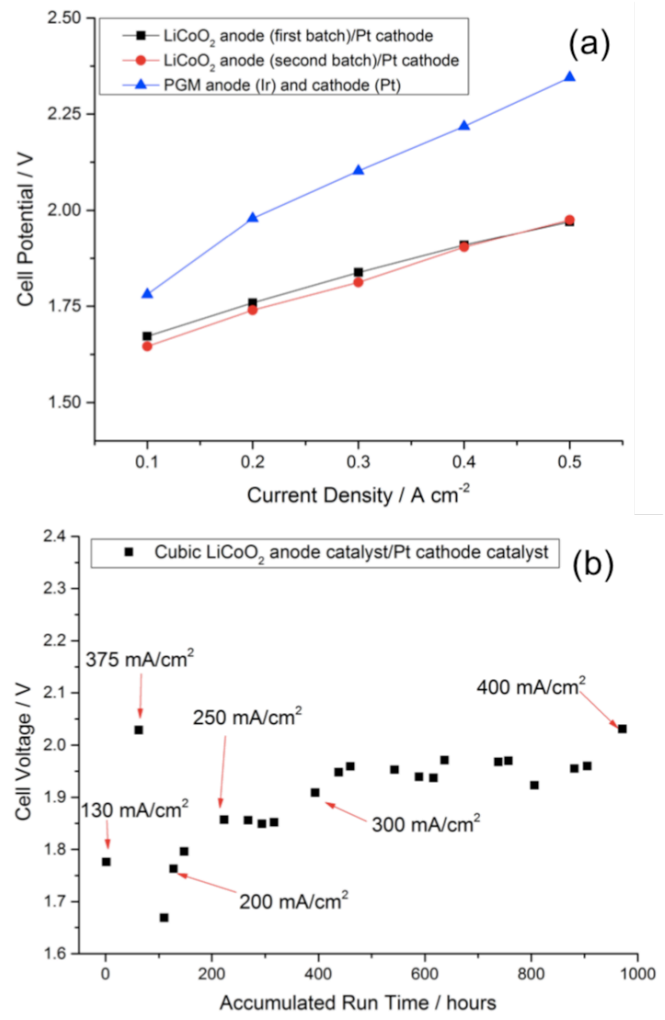

Figure 2.25 (a) Polarization curve and (b) long-term stability test of LT-$LiCoO_2$ in an alkaline exchange membrane-based water electrolyzer (AEMWE) The performance is compared to platinum-group-metal (PGM) catalysts IrO_x (anode) and PtC (cathode) – blue curve in (a), illustrating a 0.3 V lower operating potential at 500 mA/cm^{-2}.

2.2.5 Conclusions

In combination with electrochemistry, corrosion analysis, and surface sensitive HRTEM, we were able to probe precisely the distinguishing characteristics of the complex $LiCoO_2$ system during aqueous OER electrocatalysis. Starting from the pristine structures, both the layered and the cubic phases of $LiCoO_2$ form the same structure type during catalysis, the cubic spinel phase, $LiCo_2O_4$. We have temporally resolved this transformation and identified its origin stemming from Li^+ deintercalation. In addition,

we have demonstrated excellent electrocatalytic efficiency for the OER and long-term stability of the resulting spinel phase in comparison to the best noble metal catalyst used in commercial membrane-based electrolyzers (5 nm iridium). This was realized at both the lab-scale and in a membrane-based electrolyzer relevant for commercial applications. Further reduction in particle size of $LiCoO_2$ (20-100 nm) is possible and additional efficiency benefits can be anticipated.

2.2.6 Acknowledgements

This research was funded in part by the National Science Foundation, Division of Chemical Bioengineering, Environmental, and Transport Systems (CBET), and the U.S. Department of Energy, Office of Energy Efficiency and Renewable Energy, Fuel Cell Technologies Office, award number CBET-1433492. Research was also funded by DOE Small Business Innovation Research (SBIR), award number DE-SC0013179. We would like to thank Shinjae Hwang for obtaining XPS data, and Ryan BU for assistance in obtaining the ICP-OES data.

2.2.7 References

1. R. Brimblecombe, A. Koo, G. C. Dismukes, G. F. Swiegers, L. Spiccia, Solar Driven Water Oxidation by a Bioinspired Manganese Molecular Catalyst. *J. Am. Chem. Soc.* **132**, 2892–2894 (2010).

2. M. M. Najafpour, T. Ehrenberg, M. Wiechen, P. Kurz, Calcium Manganese(III) Oxides (CaMn 2O 4· x H 2O) as Biomimetic Oxygen-Evolving Catalysts. *Angew. Chem. Int. Ed.* **49**, 2233–2237 (2010).

3. N. S. McCool, D. M. Robinson, J. E. Sheats, G. C. Dismukes, A Co 4O 4"Cubane" Water Oxidation Catalyst Inspired by Photosynthesis. *J. Am. Chem. Soc.* **133**, 11446–11449 (2011).

4. J. S. Kanady, E. Y. Tsui, M. W. Day, T. Agapie, A Synthetic Model of the Mn3Ca Subsite of the Oxygen-Evolving Complex in Photosystem II. *Science*. **333**, 733–736 (2011).

5. M. Hara, C. C. Waraksa, J. T. Lean, B. A. Lewis, T. E. Mallouk, Photocatalytic Water Oxidation in a Buffered Tris(2,2‘-bipyridyl)ruthenium Complex-Colloidal IrO 2System. *J. Phys. Chem. A*. **104**, 5275–5280 (2000).

6. N. D. Morris, M. Suzuki, T. E. Mallouk, Kinetics of Electron Transfer and Oxygen Evolution in the Reaction of [Ru(bpy) 3] 3+with Colloidal Iridium Oxide. *J. Phys. Chem. A*. **108**, 9115–9119 (2004).

7. A. T. Marshall, R. G. Haverkamp, Electrocatalytic activity of IrO2â€“RuO2 supported on Sb-doped SnO2 nanoparticles. *Electrochimica Acta*. **55**, 1978–1984 (2010).

8. P. C. K. Vesborg, T. F. Jaramillo, Addressing the terawatt challenge: scalability in the supply of chemical elements for renewable energy. *RSC Adv.* **2**, 7933 (2012).

9. M. W. Kanan, D. G. Nocera, In Situ Formation of an Oxygen-Evolving Catalyst in Neutral Water Containing Phosphate and Co2+. *Science*. **321**, 1072–1075 (2008).

10. S. E. S. El Wakkad, A. Hickling, The anodic behaviour of metals. Part VI. Cobalt. *Trans. Faraday Soc.* **46**, 820–824 (1950).

11. Y. Surendranath, S. Y. Reece, D. G. Nocera, Highly active cobalt phosphate and borate based oxygen evolving catalysts operating in neutral and natural waters. *Energy Amp …* (2011).

12. O. Suzuki, M. Takahashi, T. Fukunaga, J. Kuboyama, (1968).

13. B. S. Brunschwig, M. H. Chou, C. Creutz, P. Ghosh, N. Sutin, Mechanisms of water oxidation to oxygen: cobalt (IV) as an intermediate in the aquocobalt (II)-catalyzed reaction. *J. Am. Chem. Soc.* **105**, 4832–4833 (1983).

14. D. M. Robinson, Y. B. Go, M. Greenblatt, G. C. Dismukes, Water Oxidation by λ-MnO 2: Catalysis by the Cubical Mn 4O 4Subcluster Obtained by Delithiation of Spinel LiMn 2O 4. *J. Am. Chem. Soc.* **132**, 11467–11469 (2010).

15. F. Jiao, H. Frei, Nanostructured cobalt and manganese oxide clusters as efficient water oxidation catalysts. *Energy Amp Environ. Sci.* **3**, 1018 (2010).

16. J. Y. C. Chen, J. T. Miller, J. B. Gerken, S. S. Stahl, Inverse spinel NiFeAlO 4 as a highly active oxygen evolution electrocatalyst: promotion of activity by a redox-inert metal ion. *Energy Amp Environ. Sci.* **7**, 1382–1386 (2014).

17. M. Hamdani, R. N. Singh, P. Chartier, Co3O4 and Co-based spinel oxides bifunctional oxygen electrodes. *Int J Electrochem Sci* (2010).

18. F. Jiao, H. Frei, Nanostructured Cobalt Oxide Clusters in Mesoporous Silica as Efficient Oxygen-Evolving Catalysts. *Angew. Chem. Int. Ed.* **48**, 1841–1844 (2009).

19. Arthur J. Esswein, Meredith J. McMurdo, Phillip N. Ross, Alexis T. Bell, T. Don Tilley, Size-Dependent Activity of Co3O4 Nanoparticle Anodes for Alkaline Water electrolysis. *J Phys Chem C*. **113**, 15068–15072 (2009).

20. J. Yang *et al.*, A novel preparation method for NiCo2O4 electrodes stacked with hexagonal nanosheets for water electrolysis. *J. Appl. Electrochem.* **36**, 945–950 (2006).

21. B. Chi, H. LIN, J. LI, N. WANG, J. YANG, Comparison of three preparation methods of NiCo2O4NiCo2O4 electrodes. *Int. J. Hydrog. Energy*. **31**, 1210–1214 (2006).

22. P. Rasiyah, A. C. C. Tseung, A Mechanistic Study of Oxygen Evolution on Li-Doped Co3O4. *J Electrochem Soc*. **130**, 365–368 (1983).

23. P. Rasiyah, A. C. C. Tseung, The role of the lower metal oxide/higher metal oxide couple in oxygen evolution reactions. *J. Electrochem. Soc.* **131**, 803 (1984).

24. C. Bocca, Oxygen evolution on Co3O4 and Li-doped Co3O4 coated electrodes in an alkaline solution. *Int. J. Hydrog. Energy*. **24**, 699–707 (1999).

25. R. SINGH, J. SINGH, A. Singh, Electrocatalytic properties of new spinel-type MMoO4 (M=Fe, Co and Ni) electrodes for oxygen evolution in alkaline solutions. *Int. J. Hydrog. Energy*. **33**, 4260–4264 (2008).

26. N. K. Singh, J. P. Singh, R. N. Singh, Sol-gel-derived spinel Co3O4 films and oxygen evolution: Part II. Optimization of preparation conditions and influence of the nature of the metal salt precursor. *Int. J. Hydrog. Energy*. **27**, 895–903 (2002).

27. Y. Shao-Horn, S. A. Hackney, C. S. Johnson, A. J. Kahaian, M. M. Thackeray, Structural Features of Low-Temperature LiCoO2and Acid-Delithiated Products. *J. Solid State Chem.* **140**, 116–127 (1998).

28. Y. Shao-Horn, S. A. Hackney, A. J. Kahaian, M. M. Thackeray, Structural Stability of LiCoO2 at 400°C. *J. Solid State Chem.* **168**, 60–68 (2002).

29. H. Gabrisch, R. Yazami, B. Fultz, Hexagonal to Cubic Spinel Transformation in Lithiated Cobalt Oxide. *J. Electrochem. Soc.* **151**, A891 (2004).

30. G. C. Dismukes *et al.*, Development of Bioinspired Mn 4O 4−Cubane Water Oxidation Catalysts: Lessons from Photosynthesis. *Acc. Chem. Res.* **42**, 1935–1943 (2009).

31. S. Vivekanandhan, M. Venkateswarlu, N. Satyanarayana, Novel urea assisted polymeric citrate route for the synthesis of nanocrystalline spinel LiMn2O4 powders. *J. Alloys Compd.* **441**, 284–290 (2007).

32. S. Vivekanandhan, M. Venkateswarlu, N. Satyanarayana, Ammonium carboxylates assisted combustion process for the synthesis of nanocrystalline LiCoO2 powders. *Mater. Chem. Phys.* **109**, 241–248 (2008).

33. J. Suntivich, H. A. Gasteiger, N. Yabuuchi, Y. Shao-Horn, Electrocatalytic Measurement Methodology of Oxide Catalysts Using a Thin-Film Rotating Disk Electrode. *J Electrochem Soc*. **157**, B1263 (2010).

34. S. Choi, A. Manthiram, Chemical Synthesis and Properties of Spinel Li1−xCo2O4−δ. *J. Solid State Chem.* **164**, 332–338 (2002).

35. R. J. Gummow, D. C. Liles, M. M. Thackeray, Spinel versus layered structures for lithium cobalt oxide synthesised at 400° C. *Mater. Res. Bull.* **28**, 235–246 (1993).

36. B. Garcia *et al.*, The structure of low temperature crystallized LiCoO< sub> 2</sub> *Solid State Ion.* **80**, 111–118 (1995).

37. V. Petricek, M. Dusek, L. Palatinus, *Jana2006* (2006).

38. J. A. Turner, A realizable renewable energy future. *Science*. **285**, 687–689 (1999).

39. N. S. Lewis, D. G. Nocera, Powering the planet: chemical challenges in solar energy utilization. *Proc Natl Acad Sci U A*. **103**, 15729–35 (2006).

40. Michael Ball, Martin Wietschel, *The Hydrogen Economy: Oppurtunities and Challenges* (Cambridge University Press, New York, NY USA, 2010).

41. Fuel Cell Technologies Office, Multi-Year Research, Development and Demonstration Plan (2012), (available at http://energy.gov/eere/fuelcells/downloads/fuel-cell-technologies-office-multi-year-research-development-and-22).

42. Department of Energy, *DOE Hydrogen Program: 2008 Annual Progress Report* (2008).

43. Y. Matsumoto, E. Sato, Electrocatalytic Properties of Transition Metal Oxides for Oxygen Evolution Reaction. *Mater. Chem. Phys.* **14**, 397–436 (1986).

44. C. C. L. McCrory, S. Jung, J. C. Peters, T. F. Jaramillo, Benchmarking Heterogeneous Electrocatalysts for the Oxygen Evolution Reaction. *J. Am. Chem. Soc.* **135**, 16977–16987 (2013).

45. C. C. L. McCrory *et al.*, Benchmarking hydrogen evolving reaction and oxygen evolving reaction electrocatalysts for solar water splitting devices. *J. Am. Chem. Soc.* **137**, 4347–4357 (2015).

46. J. O. Bockris, T. Otagawa, Mechanism of oxygen evolution on perovskites. *J. Phys. Chem.* **87**, 2960–2971 (1983).

47. J. O. M. Bockris, T. Otagawa, The electrocatalysis of oxygen evolution on perovskites. *J. Electrochem. Soc.* **131**, 290 (1984).

48. D. Seley, K. Ayers, B. A. Parkinson, Combinatorial Search for Improved Metal Oxide Oxygen Evolution Electrocatalysts in Acidic Electrolytes. *ACS Comb. Sci.* **15**, 82–89 (2013).

49. Ø. Ulleberg, Modeling of advanced alkaline electrolyzers: a system simulation approach. *Int. J. Hydrog. Energy*. **28**, 21–33 (2003).

50. J. O. Jensen *et al.*, *Pre-investigation of Water Electrolysis* (2008).

51. L. Trotochaud, J. K. Ranney, K. N. Williams, S. W. Boettcher, Solution-Cast Metal Oxide Thin Film Electrocatalysts for Oxygen Evolution. *J. Am. Chem. Soc.* **134**, 17253–17261 (2012).

52. R. D. L. Smith *et al.*, Photochemical Route for Accessing Amorphous Metal Oxide Materials for Water Oxidation Catalysis. *Science*. **340**, 60–63 (2013).

53. S E S El Wakkad, A Hickling, The Anodic Behavior of Metals. Part VI. Cobalt. *Trans. Faraday Soc.* **46**, 820–824 (1950).

54. M. E. LYONS, The oxygen evolution reaction on passive oxide covered transition metal electrodes in aqueous alkaline solution. Part 1-Nickel (2008).

55. M. E. LYONS, The oxygen evolution reaction on passive oxide covered transition metal electrodes in alkaline solution. Part 2-Cobalt. (2008).

56. M. E. LYONS, The oxygen evolution reaction on passive oxide covered transition metal electrodes in alkaline solution. Part III-Iron. (2008).

57. M. E. G. Lyons, M. P. Brandon, Redox switching and oxygen evolution electrocatalysis in polymeric iron oxyhydroxide films. *Phys. Chem. Chem. Phys.* **11**, 2203 (2009).

58. M. S. Burke, L. J. Enman, A. S. Batchellor, S. Zou, S. W. Boettcher, Oxygen Evolution Reaction Electrocatalysis on Transition Metal Oxides and (Oxy)hydroxides: Activity Trends and Design Principles. *Chem. Mater.* **27**, 7549–7558 (2015).

59. M. Risch *et al.*, Structural Changes of Cobalt-Based Perovskites upon Water Oxidation Investigated by EXAFS. *J. Phys. Chem. C*. **117**, 8628–8635 (2013).

60. Alexis Grimaud *et al.*, Double perovskites as a family of highly active catalysts for oxygen evolution in alkaline solution. *Nat. Commun.* (2013).

61. J. B. Gerken *et al.*, Electrochemical Water Oxidation with Cobalt-Based Electrocatalysts from pH 0–14: The Thermodynamic Basis for Catalyst Structure, Stability, and Activity. *J. Am. Chem. Soc.* **133**, 14431–14442 (2011).

62. M. Risch *et al.*, Cobalt-Oxo Core of a Water-Oxidizing Catalyst Film. *J Am Chem Soc*. **131**, 6936–6937 (2009).

63. M. W. Kanan *et al.*, Structure and Valency of a Cobalt−Phosphate Water Oxidation Catalyst Determined by in Situ X-ray Spectroscopy. *J. Am. Chem. Soc.* **132**, 13692–13701 (2010).

64. A. Harriman, I. J. Pickering, J. M. Thomas, P. A. Christensen, Metal oxides as heterogeneous catalysts for oxygen evolution under photochemical conditions. *J. Chem. Soc. Faraday Trans. 1*. **84**, 2795 (1988).

65. A. J. Esswein, M. J. McMurdo, P. N. Ross, A. T. Bell, T. D. Tilley, Size-Dependent Activity of Co 3O 4Nanoparticle Anodes for Alkaline Water Electrolysis. *J. Phys. Chem. C*. **113**, 15068–15072 (2009).

66. B. Cui *et al.*, Core-Ring Structured NiCo2O4 Nanoplatelets: Synthesis, Characterization, and Electrocatalytic Applications. *Adv. Funct. Mater.* **18**, 1440–1447 (2008).

67. B. Chi, Effect of temperature on the preparation and electrocatalytic properties of a spinel NiCo2O4/Ni electrode. *Int. J. Hydrog. Energy*. **29**, 605–610 (2004).

68. G. P. Gardner *et al.*, Structural Requirements in Lithium Cobalt Oxides for the Catalytic Oxidation of Water. *Angew. Chem. Int. Ed.* **51**, 1616–1619 (2012).

69. T. Maiyalagan, K. A. Jarvis, S. Therese, P. J. Ferreira, A. Manthiram, Spinel-type lithium cobalt oxide as a bifunctional electrocatalyst for the oxygen evolution and oxygen reduction reactions. *Nat. Commun.* **5 SP -**, 3949 (2014).

70. Y. Yamada, K. Yano, D. Hong, S. Fukuzumi, LaCoO 3 acting as an efficient and robust catalyst for photocatalytic water oxidation with persulfate. *Phys. Chem. Chem. Phys.* **14**, 5753–5760 (2012).

71. Y. Matsumoto, H. Manabe, E. Sato, Oxygen Evolution on LaSrCoO Electrodes in Alkaline Solutions. *J. Electrochem. Soc.* **127**, 811 (1980).

72. Bryan M. Hunter *et al.*, Highly Active Mixed-Metal Nanosheet Water Oxidation Catalysts Made by Pulsed-Laser Ablation in Liquids. *J. Am. Chem. Soc.* **136**, 13118–13121 (2014).

73. Fang Song, Xile Hu, Exfoliation of layered double hydroxides for enhanced oxygen evolution catalysis. *Nat. Commun.* **5** (2014).

74. M. Gong, H. Dai, A mini review of NiFe-based materials as highly active oxygen evolution reaction electrocatalysts - Springer. *Nano Res.* **8**, 23–39 (2015).

75. S. W. Lee *et al.*, The Nature of Lithium Battery Materials under Oxygen Evolution Reaction Conditions. *J. Am. Chem. Soc.*, 121008131804005 (2012).

76. Z. Lu *et al.*, Electrochemical tuning of layered lithium transition metal oxides for improvement of oxygen evolution reaction. *Nat. Commun.* **5**, 4345 (2014).

77. N. Colligan, V. Augustyn, A. Manthiram, Evidence of Localized Lithium Removal in Layered and Lithiated Spinel Li 1– xCoO 2(0 ≤ x≤ 0.9) under Oxygen Evolution Reaction Conditions. *J. Phys. Chem. C*, 150126162959004 (2015).

78. H. Liu *et al.*, Correlations among Structure, Electronic Properties, and Photochemical Water Oxidation: A Case Study on Lithium Cobalt Oxides. *ACS Catal.*, 3791–3800 (2015).

79. H. Gabrisch, R. Yazami, B. Fultz, A transmission electron microscopy study of cycled LiCoO2. *J. Power Sources*. **119-121**, 674–679 (2003).

80. S. Hwang *et al.*, Investigation of Changes in the Surface Structure of Li xNi 0.8Co 0.15Al 0.05O 2Cathode Materials Induced by the Initial Charge. *Chem. Mater.* **26**, 1084–1092 (2014).

81. N. Pereira, J. F. Al-Sharab, F. Cosandey, F. Badway, G. G. Amatucci, Thermodynamically Induced Surface Modification for the Stabilization of High-Capacity LiCoO2. *J. Electrochem. Soc.* **155**, A831–A838 (2008).

82. C. Wolverton, A. Zunger, Prediction of Li intercalation and battery voltages in layered vs. cubic LixCoO2. *J. Electrochem. Soc.* **145**, 2424–2430 (1998).

83. S. S. Kocha, Y. Garsany, D. Myers, Testing Oxygen Reduction Reaction Activity with the Rotating Disc Electrode Technique (2013), (available at https://www1.eere.energy.gov/hydrogenandfuelcells/webinars.html).

84. Y. Il Jang *et al.*, LiAl y Co1 − y O 2 (R 3̄m) Intercalation Cathode for Rechargeable Lithium Batteries. ... *Electrochem.* ... (1999).

85. G. C. Dismukes *et al.*, Nanocrystalline Ni 5P 4: A hydrogen evolution electrocatalyst of exceptional efficiency in both alkaline and acidic media. *Energy Amp Environ. Sci.* (2015), doi:10.1039/C4EE02940B.

86. D. R.G. Mitchell, Difftools: Software Tools for Electron Diffraction in Digital Micrograph. *Microsc. Res. Tech.* **71**, 588–593 (2008).

87. J. Parrondo *et al.*, Degradation of anion exchange membranes used for hydrogen production by ultrapure water electrolysis. *RSC Adv.* **4**, 9875–9879 (2014).

88. Y. Lee, J. Suntivich, K. J. May, E. E. Perry, Y. Shao-Horn, Synthesis and Activities of Rutile IrO 2and RuO 2Nanoparticles for Oxygen Evolution in Acid and Alkaline Solutions. *J. Phys. Chem. Lett.*, 399–404 (2012).

89. N. Pereira *et al.*, Stoichiometric, Morphological, and Electrochemical Impact of the Phase Stability of LixCoO2. *J. Electrochem. Soc.* **152**, A114–A125 (2005).

90. G. G. Amatucci, J. M. Tarascon, L. C. Klein, CoO2, The End Member of the LixCoO2 Solid Solution. *J. Electrochem. Soc.* **143**, 1114–1123 (1996).

91. Ermete Antolini, LiCoO2: formation, structure, lithium and oxygen nonstoichiometry, electrochemical behavior and transport properties. *Solid State Ion.* **170**, 159–171 (2004).

92. J. C. Dupin, D. Gonbeau, H. Benqlilou-Moudden, XPS analysis of new lithium cobalt oxide thin-films before and after lithium deintercalation. *Thin Solid Films*. **384**, 23–32 (2001).

93. R. J. Gummow, D. C. Liles, M. M. Thackeray, W. I. F. David, A reinvestigation of the Structures of lithium-cobalt-oxides with neutron-diffraction data. *Mater. Res. Bull.* **28**, 1177–1184 (1993).

94. M. Stanley Whittingham, Lithium Batteries and Cathode Materials. *Chem. Rev.* **104**, 4271–4301 (2004).

95. Y. Ozawa, R. Yazami, B. Fultz, An XRD Study of Chemical Self-Discharge in Delithiated Cobalt Oxide. *Electrochem. Solid-State Lett.* **8**, A38–A41 (2004).

96. A. Van der Ven, G. Ceder, Electrochemical properties of spinel LixCoO2: A first-principles investigation. *Phys. Rev. B*. **59**, 742–749 (1999).

97. D. Ensling, A. Thissen, S. Laubach, P. C. Schmidt, W. Jaegermann, Electronic structure of LiCoO2 thin films: A combined photoemission spectroscopy and density functional theory study. *Phys. Rev. B*. **82** (2010), doi:10.1103/PhysRevB.82.195431.

98. D. Ensling *et al.*, Nonrigid Band Behavior of the Electronic Structure of LiCoO2 Thin Film during Electrochemical Li Deintercalation. *Chem. Mater.* **26**, 3948–3956 (2014).

99. P. F. Smith *et al.*, What determines catalyst functionality in molecular water oxidation? Dependence on ligands and metal nuclearity in cobalt clusters. *Inorg. Chem.* **53**, 2113–2121 (2014).

100. J. Gregory McAlpin *et al.*, Electronic Structure Description of a [Co(III)3Co(IV)O4] Cluster: A Midel for the Paramagnetic Intermediate in Cobalt-Catalyzed Water Oxidation. *J. Am. Chem. Soc.* **133**, 15444–15452 (2011).

101. G. La Ganga *et al.*, Light-driven water oxidation with a molecular tetra-cobalt(III) cubane cluster. *Faraday Discuss.* **155**, 177–190 (2012).

102. R. Brimblecombe, G. F. Swiegers, G. C. Dismukes, L. Spiccia, Sustained Water Oxidation Photocatalysis by a Bioinspired Manganese Cluster. *Angew. Chem. Int. Ed.* **47**, 7335–7338 (2008).

103. M. Yagi, K. V. Wolf, P. J. Baesjou, S. L. Bernasek, G. C. Dismukes, Selective Photoproduction of O2 from the Mn4O4 cubane core: A structural and functional model for the photosynthetic water oxidizing complex. *Angew Chem Int Ed*. **40**, 2925–2928 (2001).

104. W. Ruettinger, M. Yagi, K. Wolf, S. Bernasek, G. C. Dismukes, O 2Evolution from the Manganese−Oxo Cubane Core Mn 4O 46+: A Molecular Mimic of the Photosynthetic Water Oxidation Enzyme? *J. Am. Chem. Soc.* **122**, 10353–10357 (2000).

105. D. M. Robinson *et al.*, Photochemical Water Oxidation by Crystalline Polymorphs of Manganese Oxides: Structural Requirements for Catalysis. *J. Am. Chem. Soc.* **135**, 3494–3501 (2013).

The first section of Chapter 3 titled "Tuning the Electrocatalytic Water Oxidation Properties of AB_2O_4 Spinel Nanocrystals: B (Mn, Co) Site Variants of $LiMn_2O_4$" is adapted from the following publication(*1*)

Cady, Clyde W.; Gardner, Graeme; Maron, Z.M.; Retuerto, M.; Go, Y.B.; Segan, S.; Greenblatt, M.; Dismukes, G.C. "Tuning the Electrocatalytic Water Oxidation Properties of AB_2O_4 Spinel Nanocrystals: A (Li, Mg, Zn) and B (Mn, Co) Site Variants of $LiMn_2O_4$". *ACS Catalysis*, 2015, 5, 3403-3410.

Chapter 3. Chemical Substitution of B-sites of the spinel LiM_2O_4 and related cubic $LiMO_2$ compounds and effects on oxygen electrocatalysis

3.1 Tuning the Electrocatalytic Water Oxidation Properties of AB_2O_4 Spinel Nanocrystals: B (Mn, Co) Site Variants of $LiMn_2O_4$

3.1.1 Introduction

As previously established in chapter 2, spinel-type oxides (AB_2O_4) have been studied for many years for the oxygen evolution (OER) half-reaction in water splitting(*2*–*4*) and when synthesized in high-surface forms, demonstrate low overpotentials and high efficiency (mostly in alkaline electrolyte). Although many studies exist on making these compounds from several different late 3d transition metals (Mn, Fe, Co, Ni, Cu) in high-surface area morphologies, fewer studies have tried to elucidate the effects of the crystalline(*5*–*8*) and electronic(*9*, *10*) structure on OER catalysis.

In the preceding chapter, we saw the correlation of activity for OER with a particular structural subunit, namely the M_4O_4 cubic cluster in lithium cobalt oxides. This

correlation has been seen before with both molecular(*11–14*) and heterogeneous water oxidation catalysts(*6*, *7*, *15–17*) of cobalt and manganese. Spinel-type compounds have this structural feature at their core (see **Figure 3.1**), normally with different cubes of 3d TM's being interconnected through oxo-bridges with alkali(ne) Earth metals that sit at tetrahedral sites within a cubic close-packed (ccp) anion lattice. The lithium manganate spinel, $LiMn_2O_4$, is a compound that has been studied for more than 30 years as a cathode for lithium ion batteries(*18–20*) and has already been commercially implemented quite successfully for that purpose due to its low toxicity, cost, and overall design flexibility(*21*). Compared to other compounds of manganese and oxygen, the Mn-O bonds tend to be longer and weaker (>2 Å), which may present a lower barrier to O-O bond formation in $LiMn_2O_4$. This characteristic is something somewhat unique to spinels, where the high charge density of the cubic $[M_4O_4]^{n+}$ core leads to significant Coulombic repulsion. In addition, the Mn has mixed valence at the B-site ($Mn^{3/4+}$), which means it is partially Jahn-Teller (JT) active because of the $t_{2g}^3e_g^1$ electronic configuration in an octahedral ligand field. The result is a tetragonal distortion to remove the degeneracy in the antibonding e_g orbitals, producing two long and 4 short bonds, that results in a distorted cube(*22*). In the case of Co^{3+}, which is expected to be low-spin in the 3+ state, the electronic configuration is completely different – $t_{2g}^6e_g^0$ – with a fully filled non-bonding t_{2g} set, but no antibonding electrons, which creates a very symmetrical ligand field, higher charge density, and an increased M-O core bond strength in the M_4O_4 cube. This can be seen in the low-temperature cubic phase of $LiCoO_2$, where all the Co is in the 3+ state, the core is very symmetrical, all Co-O bonds 1.97 A(*23*, *24*), which are still long for typical Co-O bonds. In the following study, the effect on OER activity of the B-site

TM replacement of Mn for Co, starting from the $LiMn_2O_4$ spinel, with up to 3 Co atoms per M_4O_4 cube, is presented.

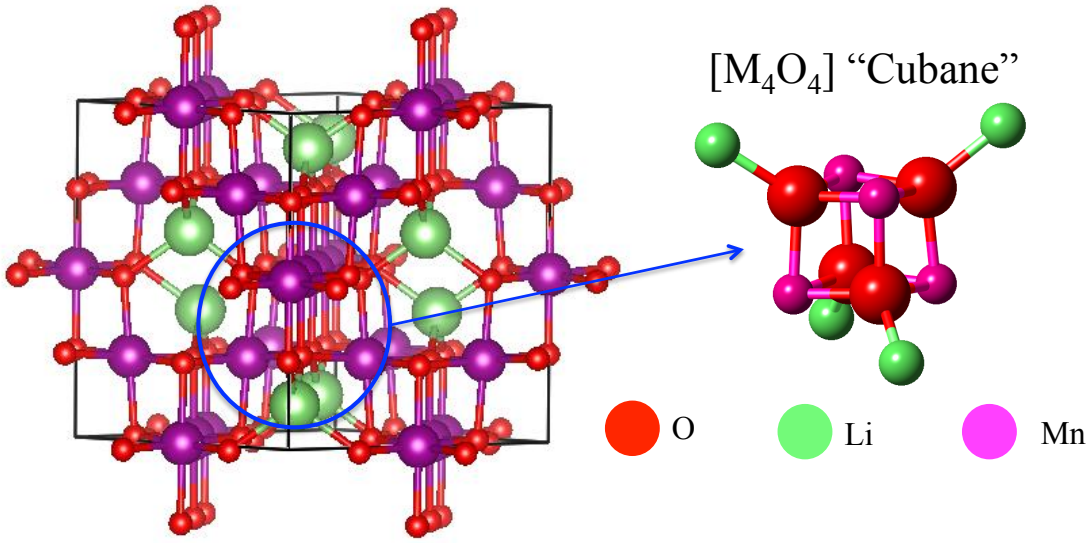

Figure 3.1 Ball and stick representation of spinel-type $LiMn_2O_4$. The picture on the left shows the core M_4O_4 subunit that exists within the framework.

3.1.2 Experimental

The comprehensive experimental details can be found in the full publication from Cady et al. (reference (*1*)).

The synthesis of the $LiMn_{2-x}Co_xO_4$ ($0 \leq x \leq 1.75$, spaced at intervals of 0.25) series was accomplished with a straightforward sol-gel procedure adapted from a previous publication(*6*). Stoichiometric amounts of acetate salts ($MnOAc_2 \bullet 4H_2O$, $LiOAc \bullet 2H_2O$, and $CoOAc_2 \bullet 4H_2O$) were dissolved in water (~20 mL) and mixed with citric acid and urea as well as 2 mL nitric acid. The molar ratio of Li:citric acid:urea was 1:6:6. The sol was stirred and dried at 80 °C to form gel, which was partially decomposed to a xerogel product at 170 °C overnight. This material was calcined at 350 °C for 6 hours, forming

the final crystalline product. The products were characterized for structure (PXRD) with a Bruker D8 Advance Diffractometer (Cu Kα = 1.5406 Å), and were refined using the Rietveld method(*25*) on the Fullprof refinement program(*26*). Catalyst morphology was characterized by scanning electron microscopy (Zeiss Sigma FESEM), and the elemental composition, which was used in the refinements was determined using ICP-OES (Perkin Elmer Optima 7300 ICP-OES).

Electrochemical characterization of catalyst performance was evaluated using a 3-electrode electrochemical cell configuration in 1 M NaOH (Sigma Aldrich, reagent grade ≥98%). Cyclic voltammograms (10 mV/sec for activity, varied scan rates for double layer capacitance determination) were obtained on a CHI 700C electrochemical workstation. The working electrode catalyst film was fabricated by drop-casting 6 μL of an ink containing catalyst, conductive carbon (acetylene black, 50% compressed, STREM Chemicals), and neutral Nafion (5% Nafion solution with 0.1 M NaOH in a 2:1 volume ratio, respectively) onto a homemade glassy carbon working electrode (0.196 cm^2) and drying at room temperature and then 120 °C to remove any residual water. The composition of the catalyst ink was 5 mg catalyst, 1.5 mg carbon, and 0.5 mL neutral Nafion. The final catalyst loading was 300 $\mu g/cm^2$. The reference electrode was a CHI Hg/HgO (140 mV vs NHE) and the counter electrode used was a carbon rod.

3.1.3 Results

Catalyst structure and morphology: The PXRD patterns, along with representative SEM images of the $LiMn_{2-x}Co_xO_4$ ($0 \leq x \leq 1.75$) series of compounds are shown in **Figure 3.2.** Consistent with previous observations(*6*, *27*), the morphology of the as-prepared spinel oxides was polydisperse nanoparticulate. The average particle size

(<100 nm) and relative particle agglomeration was consistent across the entire range of chemical compositions synthesized (**Figure 3.2a,b**). In addition, the crystallite size as determined by Scherrer equation using the FWHM of the peaks in the PXRD patterns was 20-30 nm, consistent with SEM observation. As the value for x within the series increased, the 440 peak (~65° 2θ) shifted to slightly higher values (**Figure 3.2c**), indicative of a smaller d-spacing for that plane, which would be expected for cobalt substitution obeying Vegard's Law(*28*). The ionic radius of Co^{3+}(0.545 Å) should be smaller than that of Mn^{3+}(0.645 Å)(*29*). However, a more detailed analysis for confirmation of phase was performed with Rietveld refinments of the PXRD patterns obtained.

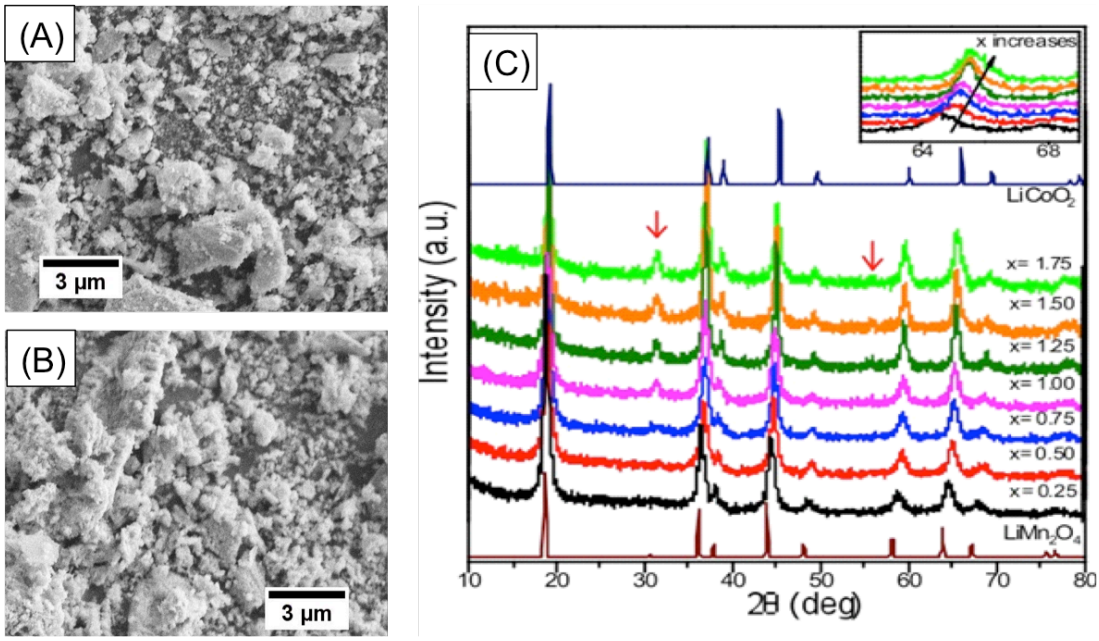

Figure 3.2 SEM images (A and B) and PXRD patterns (C) for the $LiMn_{2-x}Co_xO_4$ ($0.25 \leq x \leq 1.75$) series of spinel compounds. Inset shows lattice parameter decrease with increasing Co content.

A true solid solution B-site substitution of the ternary $LiMn_2O_4$ can be difficult, because Co^{2+} and Mn^{2+} have some finite probability of A-site occupancy if the synthesis

and stoichiometry is not properly controlled(*30*, *31*). Secondary phases like Co_3O_4 or $LiCoO_2$ may also be formed. Still, the synthesis conditions and cutoff intervals (0.25 mol) were very carefully controlled and the samples were also dissolved in acid and checked for metal stoichiometry by ICP-OES. The resulting refined stoichiometries and site occupancies, along with an example refinement are given in **Table 3.1 and Figure 3.3**. The refinement was performed starting with the $LiMn_2O_4$ Fd-3m space group, where Li occupies the tetrahedral sites (8a Wyckoff position), Mn at the octahedral site (16d Wyckoff position) and oxygen at tetrahedral anion sites (32e Wyckoff position). The resulting refinements showed that at low Co concentrations, good phase purity and clean site-substitutions were achieved. However, with increasing Co content, reflections at 2θ = ~32°, and 2θ = ~56° (as indicated in **Figure 3.2c**), begin to emerge. These are indicative of either Co or Mn going into the tetrahedral A-site (indistinguishable by X-ray). Taken together with the ICP-OES results, and the fact that the peaks are seen at high Co concentrations, the refinements were performed assuming Co was partially occupying that site, thus producing the "true" stoichiometries presented in **Table 3.1**. This result is in line with previous observations that the spinel $LiCo_2O_4$ is difficult to directly synthesize, yielding significant Co^{2+} tetrahedral site occupancy(*32–34*).

Table 3.1 Calculated Stoichiometries obtained from the PXRD Refinements using the elemental compositions as measured by ICP-OES

As Synthesized	Mn/Co	Calculated Stoichiometry
$LiMn_{1.75}Co_{0.25}O_4$	9.9	$LiMn_{1.8(3)}Co_{0.18(3)}O_4$
$LiMn_{1.50}Co_{0.50}O_4$	4.2	$LiMn_{1.62(2)}Co_{0.38(2)}O_4$
$LiMn_{1.25}Co_{0.75}O_4$	2.3	$(LiCo_{0.15(3)})(Mn_{1.50(3)}Co_{0.45(3)})O_4$
$LiMn_{1.0}Co_{1.0}O_4$	1.3	$(LiCo_{0.22(1)})(Mn_{1.28(1)}Co_{0.72(1)})O_4$
$LiMn_{0.75}Co_{1.25}O_4$	0.80	$(LiCo_{0.25(3)})(Mn_{1.00(3)}Co_{1.00(3)})O_4$
$LiMn_{0.50}Co_{1.50}O_4$	0.44	$(LiCo_{0.34(1)})(Mn_{0.71(1)}Co_{1.29(1)})O_4$

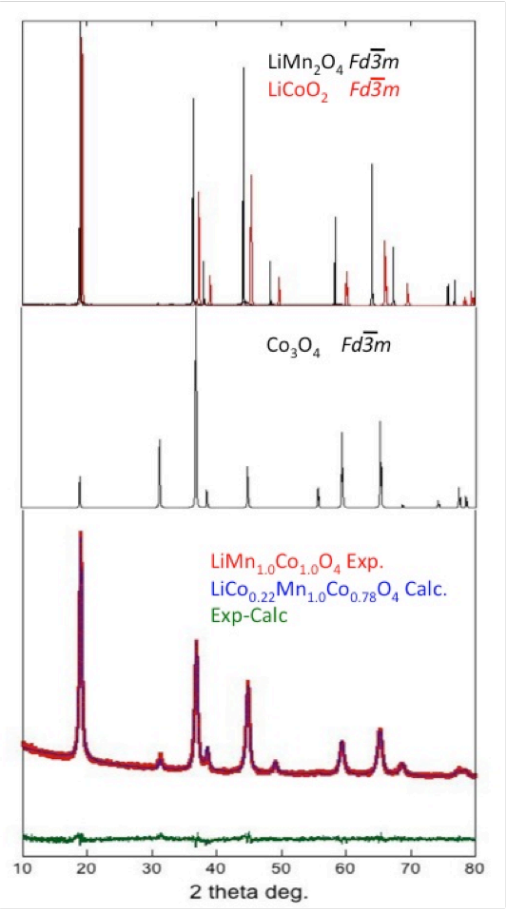

Figure 3.3 Rietveld refinement of $LiMn_{2-x}Co_xO_4$ (x = 1) in the series of substituted spinels, showing the reference patterns for the series endpoints (top) and the reference for Co_3O_4 spinel, where Co occupies the A-site.

Electrocatalytic activity for the oxygen evolution reaction (OER): The electrochemical activity of the different spinel compounds was evaluated in pH 14 electrolyte (1 M NaOH) by performing both slow scan (10 mV/sec) cyclic voltammetry (CV) (**Figure 3.4a**) and double layer capacitance measurements (C_{dl}) (**Figure 3.5**). The summary of the important metrics obtained from these experiments are illustrated graphically in **Figure 3.4b** and listed in **Table 3.2**.

For the slow scan CV's, the data are presented in **Figure 3.4** and are both iR-compensated and capacitance-corrected, to reflect true catalyst activity. Since the synthesis conditions for all compounds were kept the same, and crystallite size and particle morphology were determined to be uniform across all samples, the catalyst mass loading on the working electrode was kept the same across the series (300 μg cm^{-2}). It can be seen that almost monotonically, the activity of spinel $LiMn_{2-x}Co_xO_4$ ($0 \leq x \leq 1.75$) increases with increasing Co content. The dominant trend is that the onset of OER current occurs at lower overpotential (V above the equilibrium 1.23 V vs RHE required for water oxidation) and the curves illustrate more severe exponential behavior. This is often characterized by taking the log of the current density, j (mA cm^{-2}), and plotting it against overpotential. The linear slope thus obtained is called the Tafel slope, and follows the following relation(*35*):

$$\eta = a + b \log j$$

Where η is the overpotential, a is the intercept related to the exchange current density, j_0, and b signifies the Tafel slope. The slope is related to the mechanism of the electrocatalytic reaction(*36*, *37*), but many conditions must be met for that relation to be explicit(*37–40*), and therefore, it is often calculated and utilized to demonstrate the

efficiency of a catalyst, as it is a simple way of presenting how much more energy in volts is needed to produce an order of magnitude increase in reaction rate. It should be as low as possible. In the case of the substituted spinels, the Tafel slope generally decreases with increasing Co content (**Figure 3.4b** and **Table 3.2**). In addition, a subtler trend is overlaid on the general increase in activity, and that is that the Mn-containing spinels at intermediate Co substitution levels (x = 0.33-1) have earlier onset potentials, noted by a discontinuity in graph of Tafel slope and η with Co substitution.

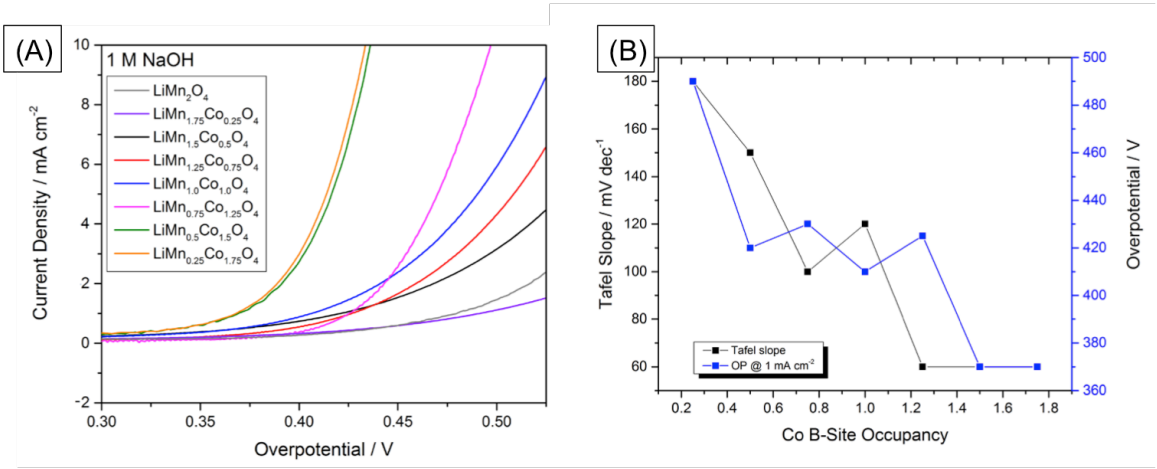

Figure 3.4 (A) Slow scan (10 mV sec^{-1}) CV's of $LiMn_{2-x}Co_xO_4$ series of compounds in alkaline electrolyte (iR-corrected, capacitance corrected) and (B) summary of OER performance metrics as a function of Co composition.

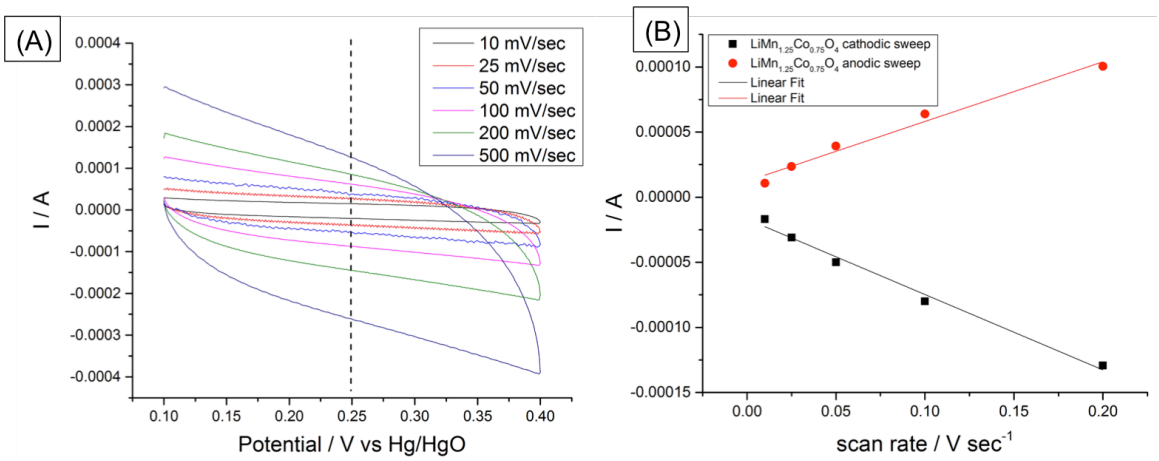

Figure 3.5 (A) Double layer capacitance CV measurements for $LiMn_{1.25}Co_{0.75}O_4$ catalyst illustrating increasing non-Faradaic charging current with increasing scan rate. (B) Plot of charging current versus scan rate to obtain C_{dl} values from the slope, which are given in Table 3.2

Electrochemical capacitance measurements of the catalyst double-layer were also performed for the series, with the values of C_{dl} presented in **Table 3.2**. These values are obtained by varying the scan rate in a CV experiment in a potential range where no Faradaic current is detected (no $M^{n/n+1}$ redox, no OER), and the current values (on cathodic and anodic sweeps) thus obtained are plotted against scan rate. An example of the scan rate dependence is shown for $LiMn_{1.25}Co_{0.75}O_4$ in **Figure 3.5**. The slope of this curve yields a capacitance value in units of Farads that corresponds ideally to the size of the double layer and therefore is related to electrochemically active surface area(*39*, *41*, *42*). However, once again, in the case of nanoparticulate oxide catalysts, this behavior is not always ideal, and the values can be related to other phenomena, including conductivity changes and pseudo-capacitive processes (most notably, in Li intercalation materials)(*43*, *44*), as well as change in the character of active sites which may involve one or more surface exposed metals to perform the OER. In the case of the spinel series, C_{dl} increases with increasing Co, which likely means an increasing conductivity in the samples, given the surface area and particle size are the same. This is consistent with

what is observed in mixed metals compounds of lithium ion battery cathodes(*45*, *46*), and is likely responsible for some, but not all, the observed increases in activity, since a conductive carbon additive is in the catalyst films to normalize for those effects.

Table 3.2 Summary of all the important OER catalyst metrics as well as values for C_{dl}.

	Tafel Slope, mV dec^{-1}	Overpotential @ 1 mA cm^{-2}	Mass Activity, @ η=400 mV (A g^{-1})	Overpotential @ 10 mA cm^{-2}	Mass activity, @ η=500 mV (A g^{-1})	Double Layer Capacitance (mF cm^{-2})
Mn2.0, Co0.0	140	550	1.1	-	2.0	2.6
Mn1.75, Co0.25	180	490	1.1	-	3.6	1.0
Mn1.5, Co0.5	150	420	2.3	-	9.8	2.2
Mn1.25, Co0.75	100	430	1.75	-	13.9	2.9
Mn1.0, Co1.0	120	410	2.76	530	18.4	4.7
Mn0.75, Co1.25	60	425	1.22	500	34.3	5.6
Mn0.5, Co1.5	60	370	8.8	440	150	7.7
Mn0.25, Co1.75	60	370	9.6	430	150	7.9
Cubic LiCoO2	50	370	30	410	160	12.7

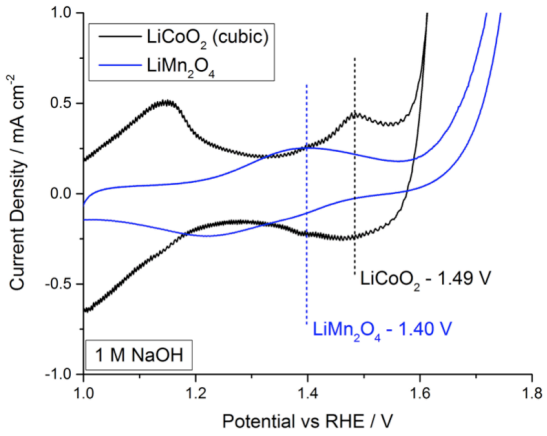

Figure 3.6 CV's showing 100 mV difference in oxidation potential for $M^{3+/4+}$ in pure $LiMn_2O_4$ (blue) and cubic $LiCoO_2$ (black).

3.1.4 Discussion and Conclusion

It is clear that introduction of Co^{3+} via the B-site of $LiMn_2O_4$ spinel causes the catalytic activity toward OER to change drastically. It seems that the contraction and symmetrization of the $M_4O_4^{n+}$ core with the more spatially uniform ligand field of $Co^{3+}(t_{2g}^6e_g^0)$ (and Mn^{4+}, $t_{2g}^3e_g^0$) as opposed to the JT-active Mn^{3+} ($t_{2g}^3e_g^0$) ion causes the binding energy for substrate *O (where * represents a surface site) to be closer to ideal. Previous theoretical work implicates a universal scaling relation in all oxygen evolution catalysis that states the binding energy of the 2 e^- apart *OH and *OOH intermediates ($\Delta E = 3.2$ eV) is fixed and limits lowering the overpotential(*47*, *48*). In order to tackle this problem, mixed metal systems have been proposed to break the scaling relation. Indeed, in looking at the redox behavior of the compositionally pure extremes $LiMn_2O_4$ and $LiCoO_2$, the oxidation potential for $M^{3+/4+}$ increases by ~100 mV for cobalt vs manganese (**Figure 3.6**). The increase in oxidation potential is expected for a Co^{4+} species based upon pourbaix diagrams and molecular complexes, and recent theoretical and experimental work suggests that the deeply oxidizing hole that can be stabilized by resonance around multiple metal centers such as those in a cube can perform water oxidation readily via a Co^{3+}-O• intermediate(*49*, *50*). The preceding analysis implicates a strongly coupled, symmetrical core catalytic unit as important for effective water oxidation. Unfortunately, the mixed manganese-cobalt spinel presented in this study does not produce a synergistic enhancement that has greater activity than both compositional endpoints, but the effect of the mixed metal B-site on reversible oxygen electrocatalysis (i.e. oxygen reduction) is not known. In the next section, a study on the effect of Mn^{3+} substitution in the cubic phase $LiCoO_2$ on reversible oxygen electrocatalysis is examined.

3.1.5 Acknowledgements

This work was funded by AFOSR grant FA9550-11-1-0231 and a postdoctoral fellowship supported by NATCO Parma. We would like to thank Paul Smith for discussions.

3.2 Influence of Chemical Substitution of Mn on B-site of Cubic $LiCoO_2$ for Reversible Oxygen Electrocatalysis: Oxygen Evolution and Reduction

3.2.1 Introduction

In the previous section, it was discovered that the charge density of the cubic core of the spinel $LiMn_2O_4$ could be modified in such a way to increase the catalytic activity for water oxidation. The replacement of Mn(III) with Co(III), which forms shorter M-O bonds due to the low-spin electronic configuration containing no anti-bonding electrons $3d^6$ ($t_{2g}^6e_g^0$) contracted the core and increased the oxidizing potential, resulting in faster kinetics for O_2 evolution. However, somewhat in contrast, in several papers on manganese oxides, the correlation between either extensive di-μ-oxo Mn bridging(*51*), longer inter Mn distances(*7*), or ultimately, higher Mn(III) content(*52–54*), the catalytic activity for water oxidation is increased. In fact, many studies have now appeared citing the role of a near-unity e_g orbital occupation for late-first row transition metals in octahedral coordination environments present in perovksites is very well-correlated with both OER (e_g~>1)(*55*) and ORR (e_g~<1)(*56*) electrocatalysis. Of course, it is perhaps too simplistic to say that approximated electronic configuration is the absolute desired property, but the correlations are importing for guiding future catalyst design. Later these trends were clarified in the context of metal-3d/oxygen-2p orbital hybridization within

the oxide, and it seems that increasing covalency correlates very well with activity in the late first-row TM series of perovskites(*57*, *58*). These issues will be elaborated on within the context of the results I the discussion section below.

In the following study, we chose to synthesize the low-temperature cubic [$A_2B_2O_4$] phase of lithium cobalt oxide ($LiCoO_2$) with partial substitution of cobalt for manganese on the B-site. The cubic phase, as discussed in the previous chapter, crystallizes in the same space group as spinel $LiMn_2O_4$ (Fd-3m) but the structure should be thought of as an ordered rock-salt structure, with Li occupying octahedral sites instead of tetrahedral sites(*59*, *60*). Incorporating Mn into the cubic structure can avoid mixed valency that was present in the $LiMn_{2-x}Co_xO_4$ spinel (Section 3.1). Maintaining Mn^{3+} is critical to elucidating its effect on reversible oxygen electrocatalysis in the cubic $LiMO_2$ phase, as it has been reported for a number of manganese-based catalysts that Mn^{3+} correlates with activity for both OER and ORR(*54*, *61–63*). We will probe that effect as well as its role in the M_4O_4 cubane motif below.

3.2.2 Experimental

The synthesis of cubic phase $LiCo_{1-x}Mn_xO_2$ ($0 \leq x \leq 0.5$) was accomplished via the traditional sol-gel route used for pure cubic $LiCoO_2$(*5*, *64*) described in detail in previous sections. Briefly, nitrate salts of cobalt, $Co(NO_3)_2 \bullet 6H_2O$, and manganese, $Mn(NO_3)_2 \bullet 4H_2O$, in stoichiometric amounts were dissolved in aqueous solution (20 mL) at intervals of x = 0, 0.1, 0.2, 0.3 etc… Citric acid and urea were added in the molar ratio of Li:C:U 1:2:2. A small amount (2 mL) of HNO_3 was used for Mn concentration $x>0.2$ to keep Mn oxides from prematurely precipitating during the initial heating phases. The

decomposition proceeded in the following way: 80 °C to form gel, 170 °C to form xerogel, 450 °C calcination to form crystalline product. Note that the calcination temperature is higher than previously reported to synthesize pure cubic phase oxides as it was apparent that some amorphous material was present when Mn was introduced to the synthesis, requiring higher temperature to make a fully crystalline product. We also synthesized a nanoscopic form of α-Mn_2O_3 (bixbyite) as a control for bifunctional oxygen electrocatalysis. The procedure for making this form of Mn_2O_3 has been published previously(*7*), but briefly, involves dissolving and recrystallizing $MnCO_3$ hydrothermally in a Teflon-lined stainless steel bomb at 150 °C for 12 hours. This light-brown precipitate is then collected and calcined at 550 °C to produce a phase-pure product. Finally, we used a Pt standard from Premetek as a control for oxygen reduction activity (10% Pt @ Vulcan Carbon).

The crystalline phase and elemental composition of the $LiCo_{1-x}Mn_xO_2$ compounds were characterized by PXRD (Philips Xpert, Cu Kα) and ICP-OES (Perkin Elmer Optima 7300 ICP-OES). Catalyst morphology and elemental composition was also examined by scanning electron microscopy (FESEM, Zeiss Sigma) equipped with Oxford energy dispersive X-ray spectroscopy (EDS).

The electrochemical characterization was performed on a CHI 700C Bipotentiostat, in a 3-electrode cell configuration, using a rotating ring-disk electrode (RRDE, Pine Instruments). The electrolyte was 0.1 M NaOH saturated with O_2 via bubbling. The working electrode was prepared by drop-casting 10 μL an ink containing catalyst, neutralized Nafion, and acetylene black in a 1:1 by volume mixture of H_2O and EtOH. The electrochemical cell used for all experiments consisted of a 3 part system

where the working electrode was submerged in a 3-necked round-bottom flask, the reference electrode was in a separated container connected to the working compartment via an electrolyte bridge (PFA tubing), and the counter electrode was placed in a tube separated from the working compartment by an anion-exchange membrane (AEM, Selemion). The reference electrode used was a homemade alkaline Mn-oxide ($Mn^{3+/4+}$ couple) electrode(*65*), and the counter electrode was a Ti-mesh. The somewhat elaborate setup is important for conducting measurements of oxygen reduction because of the risks of contamination-effects on the observed activity (especially not using Pt counter electrode).

3.2.3 Results

Performance of standard cubic $LiCoO_2$ and α-Mn_2O_3 as a bifunctional oxygen electrocatalysts: We first evaluated the catalytic activity of the standard cubic $LiCoO_2$ and α-Mn_2O_3 for reversible oxygen electrocatalysis by cycling between potentials relevant to OER and those for ORR (**Figure 3.8a,b**). This is a distinctly different procedure than that used for many "bifunctional" catalyst studies(*66–68*) as one can assess the effect that oxidative potentials have on the catalysts' activity for oxygen reduction or vise versa. Indeed, the cubic $LiCoO_2$ catalyst has distinctly different behavior before and after oxidation at potentials above 1.2 V vs RHE. The activity initially improves, and subsequently decays after repeated cycling over both electrochemical regimes. On the other hand, the nanoscopic α-Mn_2O_3 (Phase confirmed by PXRD, **Figure 3.7**) catalyst behaves quite reversibly, where after 50 cycles the activity for both reactions does not diminish significantly, and the electrochemical profile

does not change much other than a small capacitive change noted by the forward and reverse sweeps being closer together. The stability of the Mn catalyst toward potential cycling is remarkable and has been noted elsewhere(*61*, *69*, *70*). The origins and possible structure relationships will be discussed more below, in the context of the results on the substitution of the cubic phase.

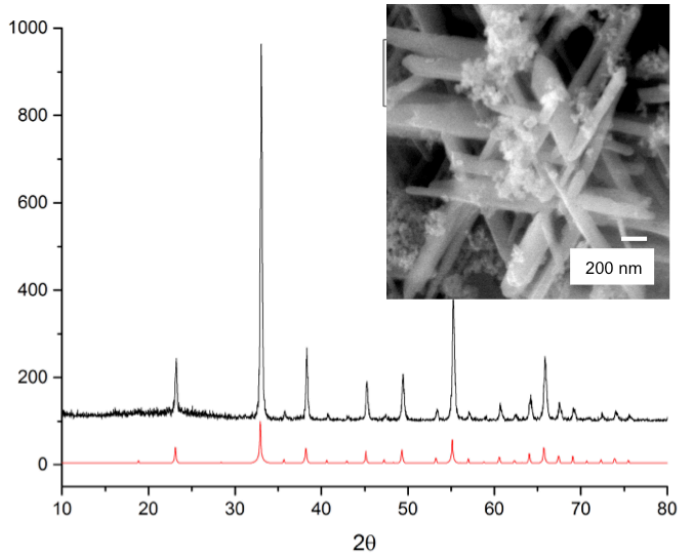

Figure 3.7 PXRD and SEM image of bixbyite α-Mn_2O_3 synthesized via hydrothermal recrystallization followed by heat treatment at 550 °C to produce highly crystalline nanorods (reference X-ray pattern in red). White bar in the inset is 200 nm.

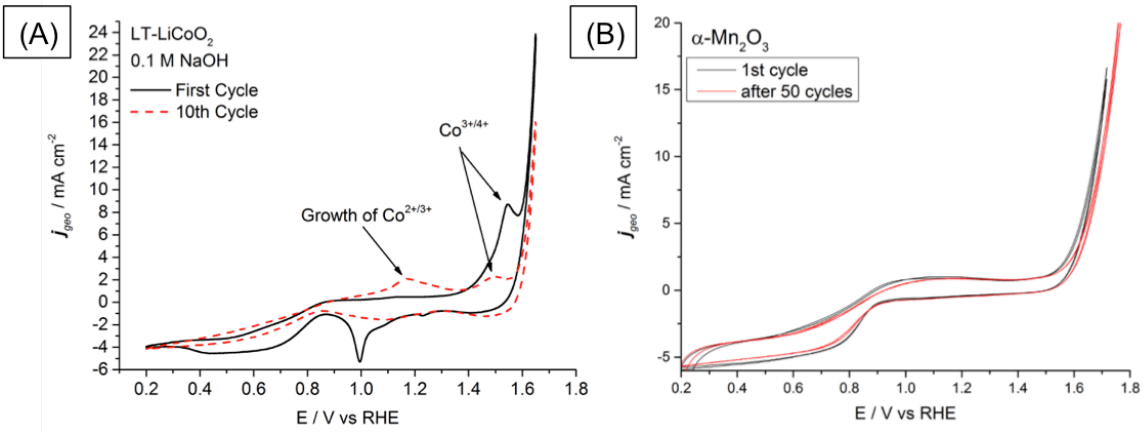

Figure 3.8 CV's of (A) cubic LT-$LiCoO_2$ and (B) α-Mn_2O_3 showing the evolution over repeated cycles between OER and ORR potentials. The red traces are after 10 cycles for $LiCoO_2$, and after 50 cycles for α-Mn_2O_3. CV's were performed on RDE (1600 rpm) in 0.1 M NaOH saturated with O_2.

Characterization of Structure and Composition of cubic $LiCo_{1-x}Mn_xO_2$ ($0 \leq x \leq 0.5$) series: The powder X-ray diffraction patterns, along with the compositional information determined by ICP-OES is given in **Figure 3.9, 3.10** and **Table 3.3**. We also show the morphology (SEM) for a select example in the series ($LiCo_{0.7}Mn_{0.3}O_2$) (**Figure 3.9c** inset). From the analysis, we find that pure cubic phase $LiMO_2$ can be synthesized with Mn substitution successfully through the series with stoichiometries that match very well to the nominal. A consistent shift of the [111] peak ($2\theta = \sim 19°$) toward larger d-spacing is expected for the replacement of the Co^{3+} with Mn^{3+}, which has a larger ionic radius(*29*). However, the limit of the solid solution appears to be at ~x=0.5, where we start to see the appearance of reflections at $2\theta = 32°$ and 56°. This trend is in agreement with the previously determined limit for substitution in the $LiMn_2O_4$ spinel, where a 50% mixture of Co and Mn at the B-site becomes unstable and occupancy of the A-site starts to occur (section 3.1 in this chapter). The elemental composition was confirmed by EDS and ICP-OES (Li cannot be detected in EDS, but can be in ICP). A small Li deficiency exists for most of the samples in the series, and two of the samples contain significant deviations from 1:1 Li:Mn (at x = 0.1 and x = 0.5). Since the trend of Li deficiency does not correlate with increasing Mn content, the solid solution limit of Mn reached at x = 0.5 is assumed to be from the interactions of Mn and Co and their site preferences rather than a Li deficiency.

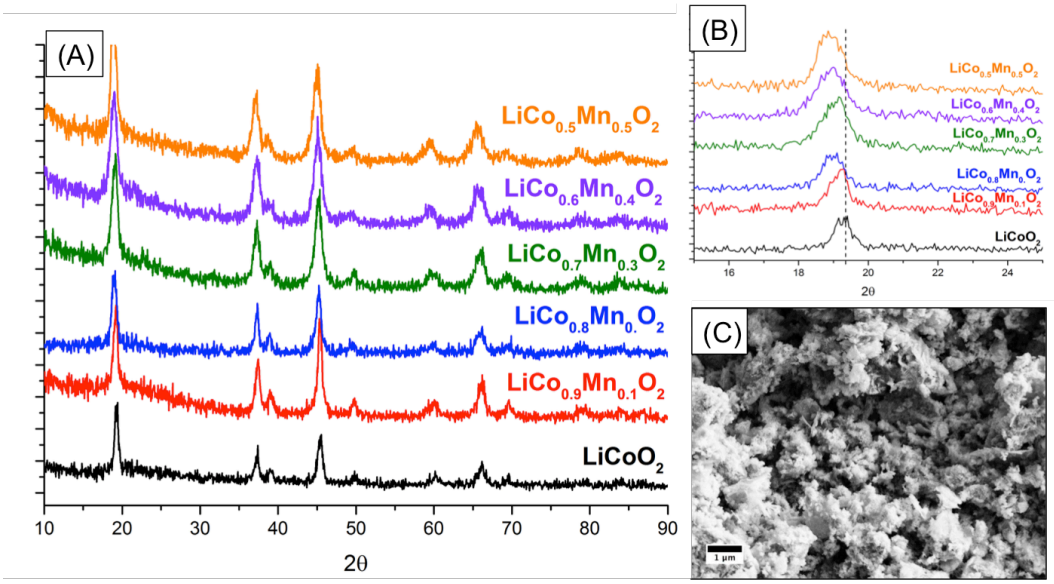

Figure 3.9 (A and B) PXRD patterns and (C) SEM of cubic phase $LiCo_{1-x}Mn_xO_2$ series. The shift of 111 peak (2θ = 19°) toward larger d-spacing is shown in (B). The morphology of the samples was consistent throughout the series and a representative SEM image ($LiCo_{0.7}Mn_{0.3}O_2$) is shown in (C).

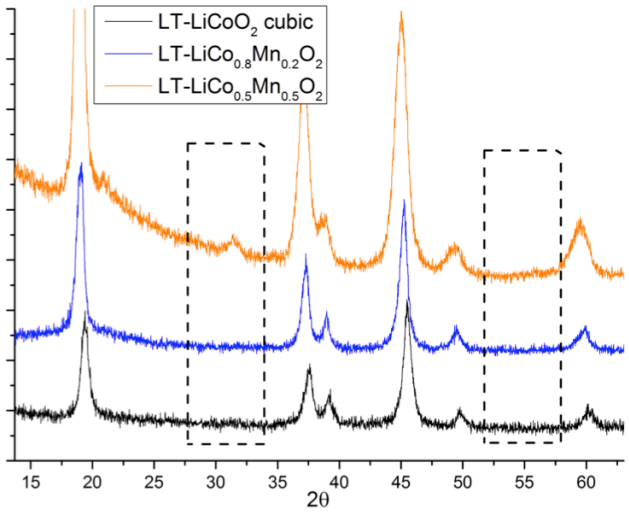

Figure 3.10 Long scan PXRD patterns of cubic $LiCo_{1-x}Mn_xO_2$ series showing appearance of small peaks at 2θ = ~32 and 56° for higher Mn content (x = 0.5) consistent with a solid solution limit where a small impurity Co_3O_4 or Mn_3O_4 phase would begin to appear.

Table 3.3 Elemental composition of cubic $LiCo_{1-x}Mn_xO_2$ as determined by ICP-OES and EDS techniques

Nominal Composition	Measured by ICP-OES	Measured by EDS
$LiCo_{0.9}Mn_{0.1}O_2$	$Li_{0.83}Co_{0.92}Mn_{0.08}O_2$	$LiCo_{0.93}Mn_{0.07}O_2$
$LiCo_{0.8}Mn_{0.2}O_2$	$Li_{0.94}Co_{0.82}Mn_{0.18}O_2$	$LiCo_{0.81}Mn_{0.19}O_2$
$LiCo_{0.7}Mn_{0.3}O_2$	$Li_{0.91}Co_{0.73}Mn_{0.27}O_2$	$LiCo_{0.72}Mn_{0.28}O_2$
$LiCo_{0.6}Mn_{0.4}O_2$	$Li_{0.93}Co_{0.61}Mn_{0.39}O_2$	$LiCo_{0.59}Mn_{0.41}O_2$
$LiCo_{0.5}Mn_{0.5}O_2$	$Li_{0.88}Co_{0.53}Mn_{0.46}O_2$	$LiCo_{0.55}Mn_{0.45}O_2$

Electrochemical activity of cubic $LiCo_{1-x}Mn_xO_2$ series: The oxygen evolution and reduction activity for the series of Mn-substituted compounds was examined in O_2-saturated alkaline electrolyte using a rotating ring-disk (RRDE) setup (**Figure 3.11**). The advantages of using RRDE techniques for examining oxygen electrocatalysis are that maximum mass-transport limited reduction currents and H_2O_2 formation can be obtained and characterized(*71–73*). The Pt ring surrounding the working electrode is poised at 1.15 V vs RHE in order to oxidize H_2O_2 without reducing product O_2 (in alkaline solution the current corresponds to HOO^- oxidation, collection efficiency 15%). The catalytic activity follows the trend of decreasing activity with increasing Mn content for both the ORR and OER. In addition, the oxidation and reduction features in the polarization curves that precede catalytic current show lower peak current values for higher Mn-content as well. The redox peak associated with pre-OER is presumed to be due to $M^{3/4+}$ transition – often concomitant with Li deintercalation – and the peak prior to ORR is presumed to be $M^{2/3+}$. The decrease in peak current with subsequent decrease in electrocatalytic current is correlated, and thus likely related to catalyst active surface area, which will be discussed below. Finally, increasing Mn content also induces a higher affinity for peroxide

formation (albeit extremely low currents), as shown in **Figure 3.12**. The ring current increases with increasing overpotential for the ORR, and with increasing Mn substitution into the cubic structure. This is typical for Mn-oxides, especially at high overpotentials for ORR(*74*). However, there is some dispute to that claim, and an alternate explanation will be offered in conjunction with the interpretation of the other data below.

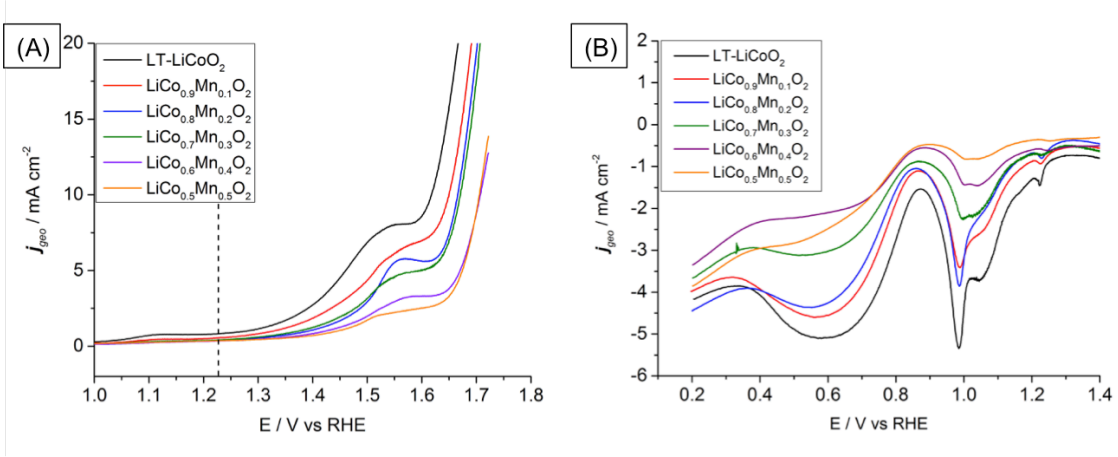

Figure 3.11 Polarization curves of $LiCo_{1-x}Mn_xO_2$ series in the OER (A) and ORR (B) potential windows. These curves were extracted from slow scan CV's (10 mV sec^{-1}) performed in 0.1 M NaOH saturated with O_2 in an RDE configuration (1600 rpm). The oxidation peaks at ~1.55 V vs RHE are due to Co^{3+} to Co^{4+} oxidation, and the reduction feature at ~1.0 V vs RHE is a Co^{3+} to $^{2+}$ transition. The current measured at >1.6 V is due to OER, and that measured <0.9 V is ORR.

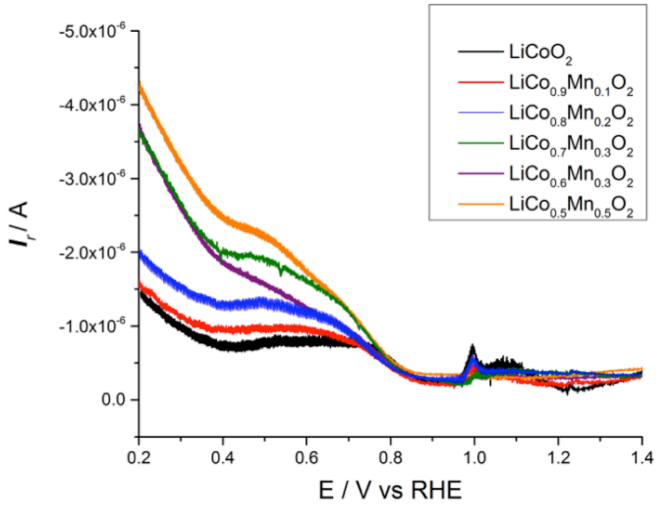

Figure 3.12 Absolute current due to peroxide oxidation measured on a Pt ring for the $LiCo_{1-x}Mn_xO_2$ series in a RRDE configuration, corresponding to the curves in Figure 3.11b (ring potential is 1.15 V vs RHE, collection efficiency, *N*, is 15%, 1600 rpm).

3.2.4 Discussion

The above analysis shows that although Mn^{3+} can be substituted into the B-site of cubic $LiCoO_2$, it does not produce a more active catalyst for either OER or ORR. It seems that the Mn that is introduced into the lattice does not result in active centers. Instead, the amount of oxidizable and reducible centers that correlate with activity decreases. This apparent lack of electrocatalytically active centers is striking given the similarity in morphology (thus physical surface area) and double-layer capacitance ("electrochemical" surface area). In some cathode materials for lithium ion batteries, similar effects are observed when Mn is substituted for Co in layered $LiCoO_2$(*75*). The capacity decreases on the order of ~30%, meaning Mn^{3+} is not readily oxidized in that environment. Similar effects are observed in $LiFeO_2$ and Fe-substituted layered $LiNiO_2$, where the addition of Fe reduces the capacity as a result of Fe^{4+} not being accessible in the rigid $Fe^{3+}O_6$ octahedra(*76*). The Jahn-Teller induced ligand environment likely remains inflexible in this structure, where edge-shared MO_6 octahedra are tightly interconnected. In the case of pure $LiCoO_2$, where the oxidation of low-spin Co^{3+} does not require large rearrangements of coordination environment (lattice parameter left virtually unchanged(*33*)), the structure is able to accommodate the incoming hole and delocalize over the Co_4O_4 cubes, whereas the transition from Mn^{3+} to Mn^{4+} is associated with a significant change in ligand environment preference (distorted tetragonal D_{4h} to octahedral O_h) which is enough to overcome the crystal field stabilization energy of removing an electron from the antibonding e_g orbitals(*77*).

However, this still does not explain the lack of activity from the Mn-substituted compounds, because according to the literature, Mn^{3+} content is essential for higher activity, as was introduced earlier in this section. The preceding discussion explains the inability to oxidize Mn^{3+} to $^{4+}$, which seems like it would actually favor higher activity by preventing the formation of inert Mn^{4+}, rather than correlate with a decrease in activity. To reconcile the apparent contradictory effects, the following explanation is proposed.

The coordination environment of the active TM and the degree of covalency in the lattice have both been correlated with activity in several catalysts, ranging from Fe/Co perovskites(*57*, *78*, *79*), to Mn oxides(*7*, *8*, *80*, *81*). In fact, to justify the high OER activity seen in Mn_2O_3, where the types of MnO_6 coordination environments vary greatly within the structure, it was suggested that the bent nature of surface exposed MnO_6 can bring two oxide O^{2-} quite close to each other, lowering activation for O-O bond formation(*62*). A recent study from Dismukes and coworkers that reexamined the correlation of activity with Mn^{3+} content uncovered a better explanation for the observed activity(*81*). It was predicted and confirmed that the corner-shared MnO_6 octahedra present in structural analogues β-MnO_2 and γ-MnOOH would result in only the latter being active because of the presence of Mn^{3+}. Indeed this is the case, and it also holds true for hexagonal vs triclinic birnessite $(K^+,Na^+)_xMnO_2$, where the corner-shared $Mn^{3+}O_6$ octahedra are only present in the layers of the former (and thus, why that structure-type is active). Extending this concept further, it was postulated that the trigonal antiprismatic (D_{3d}) site in bixbyite Mn_2O_3 is also unique and likely responsible for the significant OER activity in that phase because the JT-distortion is suppressed by an atypical ligand environment where the O^{2-} ligands lie along the direction of the d_{yz} and

d_{xz} orbitals. The result is Mn-O bonds of intermediate length, and a O-Mn-O angle <90°, once again raising the possibility for more facile O-O bond coupling due to somewhat weak and close-proximity bonds. The structural motif of corner-shared MnO_6 octahedra is important to recognize because of the similarity to the dangling Mn in the $CaMn_4O_x$ oxygen-evolving complex (OEC) of photosystem II. It is widely implicated as one of the principle binding sites for the substrate waters in multiple models(*82*, *83*), and the coordination environment resemblance to those of avtice Mn-oxides is unlikely a coincidence. The structure of cubic $LiCoO_2$ (and substituted variants), has closely packed edge-shared MO_6 octahedra. This favors the Co oxidation, as explained previously, where a hole can be partially delocalized around the cube, but not Mn oxidation. In addition, the oxygen bond flexibility imparted by the corner-shared or trigonal antiprismatic sites cannot be realized. For this reason, the Mn^{3+} remain sequestered in the lattice as non-electrocatalytically active sites, thus explaining the decrease in activity with increasing substitution. This also coincides with increased peroxide formation, as the decomposition of a peroxide surface intermediate often requires adjacent active sites to split the O-O bond(*84*). With a uniform replacement of Co for Mn in $LiCo_{1-x}Mn_xO_2$ ($0 \leq x \leq 0.5$), the active sites on the surface will be disrupted, making peroxide intermediates hang around longer.

3.2.5 Conclusions

In summary, although the electrocatalytic activity for OER/ORR on many Mn^{3+} containing oxides seems to be very attractive, it should be noted that a distinct structure type is needed to actually elicit good performance. By incorporating Mn into the B-site of

cubic $LiCoO_2$, we preserved the oxidation state of Mn and the parent structure of $LiCoO_2$, but the result is a decrease in catalytic activity with increasing Mn content, corresponding to a decrease in effective electrochemically active sites (Co^{3+}). We conclude that cobalt ($Co^{3+/4+}$) is responsible for all of the observed activity because it resides in ideal crystallographic positions, whereas Mn serves to render those sites inactive, because they are not the coordination environments needed to make Mn^{3+} active. For future catalyst development, hybridizing the electronic properties of two elements in order to make an active catalyst should only be performed if they are likely to operate with similar mechanisms or have proven to be active with similar coordination environments. This study emphasizes the effect of structure is more important than composition for many catalysts.

3.2.6 Acknowledgements

This work was supported by DOE Small Business Innovation Research (SBIR), award number DE-SC0013179. We would also like to acknowledge support from an National Science Foundation Integrative Graduate Education and Research Traineeship NSF-IGERT award number 0903675 fellowship, Sustainable Fuel Solutions for the 21st century (G.G.). We would like to thank Karin Calvinho and Ryan Bu for their help in obtaining ICP-OES measurements.

3.3 References:

1. C. W. Cady *et al.*, Tuning the Electrocatalytic Water Oxidation Properties of AB2O4 Spinel Nanocrystals: A (Li, Mg, Zn) and B (Mn, Co) Site Variants of LiMn2O4. *ACS Catal.* **5**, 3403–3410 (2015).

2. V. N. Parmon, G. L. Elizarova, T. V. Kim, Spinels as heterogeneous catalysts for oxidation of water to dioxygen by tris-bipyridyl complexes of iron (III) and ruthenium (III). *React. Kinet. Catal. ….* **21**, 195–197 (1982).

3. M. Hamdani, R. N. Singh, P. Chartier, Co3O4 and Co-based spinel oxides bifunctional oxygen electrodes. *Int J Electrochem Sci* (2010).

4. F. Cheng *et al.*, Rapid room-temperature synthesis of nanocrystalline spinels as oxygen reduction and evolution electrocatalysts. *Nat. Chem.* **3**, 79–84 (2011).

5. G. P. Gardner *et al.*, Structural Requirements in Lithium Cobalt Oxides for the Catalytic Oxidation of Water. *Angew. Chem. Int. Ed.* **51**, 1616–1619 (2012).

6. D. M. Robinson, Y. B. Go, M. Greenblatt, G. C. Dismukes, Water Oxidation by λ-MnO 2: Catalysis by the Cubical Mn 4O 4Subcluster Obtained by Delithiation of Spinel LiMn 2O 4. *J. Am. Chem. Soc.* **132**, 11467–11469 (2010).

7. D. M. Robinson *et al.*, Photochemical Water Oxidation by Crystalline Polymorphs of Manganese Oxides: Structural Requirements for Catalysis. *J. Am. Chem. Soc.* **135**, 3494–3501 (2013).

8. C. E. Frey, P. Kurz, Water Oxidation Catalysis by Synthetic Manganese Oxides with Different Structural Motifs: A Comparative Study. *Chem. - Eur. J.* **21**, 14958–14968 (2015).

9. M. García-Mota *et al.*, Importance of Correlation in Determining Electrocatalytic Oxygen Evolution Activity on Cobalt Oxides. *J. Phys. Chem. C*. **116**, 21077–21082 (2012).

10. U. Maitra, B. S. Naidu, A. Govindaraj, Importance of trivalency and the eg1 configuration in the photocatalytic oxidation of water by Mn and Co oxides (2013).

11. R. Brimblecombe *et al.*, Sustained Water Oxidation by [Mn 4O 4] 7+Core Complexes Inspired by Oxygenic Photosynthesis. *Inorg. Chem.* **48**, 7269–7279 (2009).

12. R. Brimblecombe, A. Koo, G. C. Dismukes, G. F. Swiegers, L. Spiccia, Solar Driven Water Oxidation by a Bioinspired Manganese Molecular Catalyst. *J. Am. Chem. Soc.* **132**, 2892–2894 (2010).

13. P. F. Smith *et al.*, What determines catalyst functionality in molecular water oxidation? Dependence on ligands and metal nuclearity in cobalt clusters. *Inorg. Chem.* **53**, 2113–2121 (2014).

14. G. La Ganga *et al.*, Light-driven water oxidation with a molecular tetra-cobalt(III) cubane cluster. *Faraday Discuss.* **155**, 177–190 (2012).

15. F. Jiao, H. Frei, Nanostructured Cobalt Oxide Clusters in Mesoporous Silica as Efficient Oxygen-Evolving Catalysts. *Angew. Chem. Int. Ed.* **48**, 1841–1844 (2009).

16. L.-P. Wang, T. Van Voorhis, Direct-Coupling O 2Bond Forming a Pathway in Cobalt Oxide Water Oxidation Catalysts. *J. Phys. Chem. Lett.* **2**, 2200–2204 (2011).

17. G. Mattioli, M. Risch, A. A. Bonapasta, H. Dau, L. Guidoni, Protonation states in a cobalt-oxide catalyst for water oxidation: fine comparison of ab initio molecular dynamics and X-ray absorption spectroscopy results. *Phys Chem Chem Phys*. **13**, 15437–15441 (2011).

18. M. M. Thackeray, W. I. F. David, P. G. Bruce, J. B. Goodenough, Lithium insertion into manganese spinels. *Mater. Res. Bull.* **18**, 461–472 (1983).

19. M. M. Thackeray, Manganese oxides for lithium batteries. *Prog. Solid State Chem.* **25**, 1–71 (1997).

20. M. M. Thackeray, C. Wolverton, E. D. Isaacs, Electrical energy storage for transportation—approaching the limits of, and going beyond, lithium-ion batteries. *Energy Amp Environ. Sci.* **5**, 7854 (2012).

21. I. Buchmann, *Batteries in a Portable World: A Handbook on Rechargeable Batteries for Non-engineers* (Cadex Electronics Inc., ed. 3rd, 2011).

22. A. S. Wills, N. P. Raju, J. E. Greedan, Low-Temperature Structure and Magnetic Properties of the Spinel LiMn 2O 4: A Frustrated Antiferromagnet and Cathode Material. *Chem. Mater.* **11**, 1510–1518 (1999).

23. R. J. Gummow, D. C. Liles, M. M. Thackeray, Spinel versus layered structures for lithium cobalt oxide synthesised at 400° C. *Mater. Res. Bull.* **28**, 235–246 (1993).

24. R. J. Gummow, D. C. Liles, M. M. Thackeray, W. I. F. David, A reinvestigation of the Structures of lithium-cobalt-oxides with neutron-diffraction data. *Mater. Res. Bull.* **28**, 1177–1184 (1993).

25. H. M. Rietveld, A profile refinement method for nuclear and magnetic structures. *J. Appl. Crystallogr.* **2**, 65–71 (1969).

26. J. Rodriguez-Carvajal, Recent advances in magnetic structure determination by neutron powder diffraction. *Phys. B Condens. Matter*. **192**, 55–69 (1993).

27. S. Vivekanandhan, M. Venkateswarlu, N. Satyanarayana, Novel urea assisted polymeric citrate route for the synthesis of nanocrystalline spinel LiMn2O4 powders. *J. Alloys Compd.* **441**, 284–290 (2007).

28. A. R. Denton, N. W. Ashcroft, Vegard's Law. *Phys. Rev. A*. **43**, 3161–3164 (1991).

29. R. D. Shannon, Revised Effective Ionic Radii and Systematic Studies of Interatomie Distances in Halides and Chaleogenides. *Acta Crystallogr.* **A32**, 751–767 (1976).

30. A. Navrotsky, Thermodynamics of A3O4-B3O4 spinel solid solutions. *J. Inorg. Nucl. Chem.* **31**, 59–72 (1969).

31. M. Yonemura *et al.*, Synthesis, structure, and phase relationship in lithium manganese oxide spinel. *J. Mater. Chem.* **14**, 1948–1958 (2004).

32. S. Choi, A. Manthiram, Synthesis and Electrochemical Properties of LiCoO Spinel Cathodes. *J. Electrochem. Soc.* **149**, A162 (2002).

33. S. Choi, A. Manthiram, Chemical Synthesis and Properties of Spinel Li1−xCo2O4−δ. *J. Solid State Chem.* **164**, 332–338 (2002).

34. E. Meza, D. Alburquenque, J. Ortiz, J. L. Gautier, LITHIUM COBALT SPINEL OXIDE: A STRUCTURAL AND ELECTROCHEMICAL STUDY. *J. Chil. Chem. Soc.* **53**, 1494–1497 (2008).

35. A. J. Bard, L. R. Faulkner, *Electrochemical Methods: Fundamentals and Applications* (John Wiley & Sons, New York, NY USA, ed. 2nd, 2001).

36. J. O. Bockris, Kinetics of Activation Controlled Consecutive Electrochemical Reactions: Anodic Evolution of Oxygen. *J. Chem. Phys.* **24**, 817 (1956).

37. S. Fletcher, Tafel slopes from first principles. *J. Solid State Electrochem.* (2009).

38. J. O. Bockris, T. Otagawa, Mechanism of oxygen evolution on perovskites. *J. Phys. Chem.* **87**, 2960–2971 (1983).

39. C. C. L. McCrory, S. Jung, J. C. Peters, T. F. Jaramillo, Benchmarking Heterogeneous Electrocatalysts for the Oxygen Evolution Reaction. *J. Am. Chem. Soc.* **135**, 16977–16987 (2013).

40. E. J. Coleman, A. C. Co, The Complex Inhibiting Role of Surface Oxide in the Oxygen Reduction Reaction. *ACS Catal.* **5**, 7299–7311 (2015).

41. S. Trasatti, O. A. Petrii, Real surface area measurements in electrochemistry. *J. Electroanal. Chem.* **327**, 353–376 (1992).

42. J. O. M. Bockris, T. Otagawa, The electrocatalysis of oxygen evolution on perovskites. *J. Electrochem. Soc.* **131**, 290 (1984).

43. S. Jung, C. C. L. McCrory, I. M. Ferrer, J. C. Peters, T. F. Jaramillo, Benchmarking nanoparticulate metal oxide electrocatalysts for the alkaline water oxidation reaction. *J. Mater. Chem. A*. **4**, 3068–3076 (2016).

44. G. Gardner *et al.*, Structural basis for differing electrocatalytic water oxidation by the cubic, layered and spinel forms of lithium cobalt oxides. *Energy Amp Environ. Sci.* **9**, 184–192 (2016).

45. M. Kunduraci, J. F. Al-Sharab, G. G. Amatucci, High-Power Nanostructured LiMn2-xNixO4 High-Voltage Lithium-Ion Battery Electrode Materials: Electrochemical Impact of Electronic Conductivity and Morphology. *Chem. Mater.* **18**, 3585–3592.

46. M. S. Whittingham, Lithium batteries and cathode materials. *Chem. Rev.-Columb.* (2004).

47. I. C. Man *et al.*, Universality in Oxygen Evolution Electrocatalysis on Oxide Surfaces. *ChemCatChem*. **3**, 1159–1165 (2011).

48. M. Garcia-Mota *et al.*, Tailoring the Activity for Oxygen Evolution Electrocatalysis on Rutile TiO2(110) by Transition-Metal Substitution. *ChemCatChem*. **3**, 1607–1611 (2011).

49. A. I. Nguyen *et al.*, Mechanistic Investigations of Water Oxidation by a Molecular Cobalt Oxide Analogue: Evidence for a Highly Oxidized Intermediate and Exclusive Terminal Oxo Participation. *J. Am. Chem. Soc.* **137**, 12865–12872 (2015).

50. P. F. Smith *et al.*, Water Oxidation by the [Co4O4(OAc)4(py)4]+ Cubium is Initiated by OH– Addition. *J. Am. Chem. Soc.* **137**, 15460–15468 (2015).

51. I. Zaharieva *et al.*, Electrosynthesis, functional, and structural characterization of a water-oxidizing manganese oxide. *Energy Amp ...* (2012), doi:10.1016/j.ccr.2012.03.031.

52. T. Takashima, K. Hashimoto, R. Nakamura, Inhibition of Charge Disproportionation of MnO 2Electrocatalysts for Efficient Water Oxidation under Neutral Conditions. *J. Am. Chem. Soc.* **134**, 18153–18156 (2012).

53. T. Takashima, K. Hashimoto, R. Nakamura, Mechanisms of pH-Dependent Activity for Water Oxidation to Molecular Oxygen by MnO 2Electrocatalysts. *J. Am. Chem. Soc.* **134**, 1519–1527 (2012).

54. Z. Luo, S. Y. Chen, J. F. Rusling, J. He, S. L. Suib, Robust Mesoporous Manganese Oxide Catalysts for Water Oxidation - ACS Catalysis (ACS Publications). ... *Catal.* (2015).

55. J. Suntivich, K. J. May, H. A. Gasteiger, J. B. Goodenough, Y. Shao-Horn, A Perovskite Oxide Optimized for Oxygen Evolution Catalysis from Molecular Orbital Principles. *Science*. **334**, 1383–1385 (2011).

56. J. Suntivich *et al.*, Design principles for oxygen-reduction activity on perovskite oxide catalysts for fuel cells and metal–air batteries. *Nat. Chem.* **3**, 546–550 (2011).

57. A. Grimaud *et al.*, Double perovskites as a family of highly active catalysts for oxygen evolution in alkaline solution. *Nat. Commun.* **4**, 2439 (2013).

58. J. Suntivich *et al.*, Estimating Hybridization of Transition Metal and Oxygen States in Perovskites from O K-edge X-ray Absorption Spectroscopy. *J. Phys. Chem. C.* **118**, 1856–1863 (2014).

59. Y. Shao-Horn, S. A. Hackney, C. S. Johnson, A. J. Kahaian, M. M. Thackeray, Structural Features of Low-Temperature LiCoO2and Acid-Delithiated Products. *J. Solid State Chem.* **140**, 116–127 (1998).

60. W. Huang, R. Frech, Vibrational spectroscopic and electrochemical studies of the low and high temperature phases of LiCo< sub> 1− x</sub> M< sub> x</sub> O< sub> 2</sub>(< i> M</i>=< i> Ni</i> or< i> Ti</i>). *Solid State Ion.* **86**, 395–400 (1996).

61. Y. Gorlin, T. F. Jaramillo, A Bifunctional Nonprecious Metal Catalyst for Oxygen Reduction and Water Oxidation. *J. Am. Chem. Soc.* **132**, 13612–13614 (2010).

62. A. Ramírez *et al.*, Evaluation of MnO x, Mn 2O 3, and Mn 3O 4Electrodeposited Films for the Oxygen Evolution Reaction of Water. *J. Phys. Chem. C*. **118**, 14073–14081 (2014).

63. K. A. Stoerzinger *et al.*, Oxygen electrocatalysis on (001)-oriented manganese perovskite films: Mn valency and charge transfer at the nanoscale. *Energy Environ. Sci.* **6**, 1582–1588 (2013).

64. S. Vivekanandhan, M. Venkateswarlu, N. Satyanarayana, Ammonium carboxylates assisted combustion process for the synthesis of nanocrystalline LiCoO2 powders. *Mater. Chem. Phys.* **109**, 241–248 (2008).

65. R. C. Massé, J. B. Gerken, Assembly of a Robust and Economical MnO2-Based Reference Electrode. *J. Chem. Educ.* **92**, 110–115 (2015).

66. Y. Liu, D. C. Higgins, J. Wu, M. Fowler, Z. Chen, Cubic spinel cobalt oxide/multi-walled carbon nanotube composites as an efficient bifunctionalelectrocatalyst for oxygen reaction. *Electrochem. Commun.* **34**, 125–129 (2013).

67. K. Zhang *et al.*, Mesoporous Cobalt Molybdenum Nitride: A Highly Active Bifunctional Electrocatalyst and Its Application in Lithium–O2 Batteries. *J. ...* (2013).

68. J. Masa *et al.*, Mnx Oy /NC and Cox Oy /NC Nanoparticles Embedded in a Nitrogen-Doped Carbon Matrix for High-Performance Bifunctional Oxygen Electrodes. *Angew. Chem. Int. Ed Engl.* (2014), doi:10.1002/anie.201402710.

69. J. W. Desmond Ng, Y. Gorlin, T. Hatsukade, T. F. Jaramillo, A Precious-Metal-Free Regenerative Fuel Cell for Storing Renewable Electricity. *Adv. Energy Mater.* **3**, 1545–1550 (2013).

70. Y. Gorlin *et al.*, In Situ X-ray Absorption Spectroscopy Investigation of a Bifunctional Manganese Oxide Catalyst with High Activity for Electrochemical Water Oxidation and Oxygen Reduction. *J. Am. Chem. Soc.* **135**, 8525–8534 (2013).

71. N. M. Markovic, H. A. Gasteiger, P. N. Ross, Oxygen Reduction on Platinum Low-Index Single-Crystal Surfaces in Sulfuric-Acid-Solution - Rotating Ring-Pt(Hkl) Disk Studies. *J. Phys. Chem.* **99**, 3411–3415 (1995).

72. W. Xing, G. Yin, J. Zhang, *Rotating Electrode Methods and Oxygen Reduction Electrocatalysts* (Elsevier, Amsterdam, The Netherlands, 2014).

73. Nenad M Marković, and Hubert A Gasteiger, J. Ross, Oxygen Reduction on Platinum Low-Index Single-Crystal Surfaces in Alkaline Solution: Rotating Ring DiskPt(hkl) Studies. ... *Phys. Chem.* (1996).

74. F. H. B. Lima, M. L. Calegaro, E. A. Ticianelli, Investigations of the catalytic properties of manganese oxides for the oxygen reduction reaction in alkaline media. *J. Electroanal. Chem.* **590**, 152–160 (2006).

75. A. Azahidi *et al.*, Mn as a Substituted Cation in LiCoO2 Cathode Materials. *Advaced Mater. Res.* **545**, 204–208 (2012).

76. C. Delmas, M. Ménétrier, L. Croguennec, Lithium batteries: a new tool in solid state chemistry. *Int. J.* ... (1999) (available at http://www.sciencedirect.com/science/article/pii/S1463017699000034).

77. J. Reed, G. Ceder, Role of electronic structure in the susceptibility of metastable transition-metal oxide structures to transformation. *Chem. Rev.* (2004).

78. S. Yagi *et al.*, Covalency-reinforced oxygen evolution reaction catalyst. *Nat. Commun.* **6**, 8249 (2015).

79. W. T. Hong, R. E. Welsch, Y. Shao-Horn, Descriptors of Oxygen-Evolution Activity for Oxides: A Statistical Evaluation - The Journal of Physical Chemistry C (ACS Publications). *J. Phys.* .... **120**, 78–86 (2016).

80. R. Pokhrel, M. K. Goetz, S. E. Shaner, X. Wu, S. S. Stahl, The "Best Catalyst" for Water Oxidation Depends on the Oxidation Method Employed: A Case Study of Manganese Oxides. *J. Am. Chem. Soc.* **137**, 8384–8387 (2015).

81. P. F. Smith, B. J. Deibert, S. Kaushik, G. Gardner, Coordination Geometry and Oxidation State Requirements of Corner Sharing MnO6 Octahedra for Water Oxidation Catalysis: An Investigation of Manganite (γ-MnOOH) - ACS Catalysis (ACS Publications). ... *Catal.* (2016).

82. D. J. Vinyard, G. M. Ananyev, G. C. Dismukes, Photosystem II: The Reaction Center of Oxygenic Photosynthesis. *Annu. Rev. Biochem.* (2013), doi:10.1146/annurev-biochem-070511-100425.

83. V. Krewald, M. Retegan, N. Cox, J. Messinger, Metal oxidation states in biological water splitting. *Chem.* .... **6**, 1676–1695 (2015).

84. F. Cheng, J. Chen, Metal-air batteries: from oxygen reduction electrochemistry to cathode catalysts. *Chem. Soc. Rev.* **41**, 2172–2192 (2012).

Chapter 4 is adapted from the following manuscript, *in preparation*:

Gardner, Graeme; Hwang, Shinjae; Porter, Spencer; Garfunkel, Eric; Greenblatt, Martha; Dismukes, G. Charles, "Distinguishing Activity and Reversibility for Oxygen Electrocatalysis in Bifunctional Cobalt Molybdenum Nitride", *in prep.*

4.1 Introduction

A closed fuel cycle like the water splitting/water formation reaction negates the detrimental effects of carbon dioxide pollution have on our environment as long as it is predicated on renewable energy. Therefore there exists a critical need for electrolyzers and fuel cells to realize a renewable-energy based economy, where transient sources of energy need to be converted and stored locally and then utilized in convenient ways for stationary and mobile applications. It would seem logical therefore that an electrolyzer would be integrated with a fuel cell in many instances, sometimes denoted unitized regenerative fuel cell (URFC) systems, that could both convert electricity to hydrogen and vice versa[1, 2]. However, as simple as this may sound, URFCs do not exist. Their practical implementation is severely limited because of, not only serious engineering challenges, but also fundamental challenges in the chemistry, even when noble metal catalysts are used[3]. The problems of designing materials based upon non-PGM's that operate both as oxygen evolution and reduction catalysts (for both OER and ORR), or both hydrogen evolution and oxidation (HER/HOR) catalysts is exceeding difficult. Currently, only one example of an entirely non-noble metal catalyst-based URFC has been demonstrated, and the power density reaches only 16 mW/cm^2 [2], far below the 300-1000 mW/cm^2 offered by PEMFC. It is therefore important for the research community

to address this problem by proposing new catalysts based upon rational design principles, perhaps exploring non-conventional compounds that find use in other catalytic applications.

For the purposes of this paper, it may also be important to highlight the difference between bifunctional catalysis and reversible catalysis. Bifunctional catalysts for varying electrocatalytic reactions are reported very frequently, from materials that can catalyze both OER and ORR[4-8], to those that can perform OER and HER[9-11] reactions. Frequently, the activity for both reactions is studied completely independently of one another without mentioning the reversibility of said catalyst. This is somewhat understandable, at least in the case where the catalyst is being examined for the HER and OER reactions, because the optimized experimental conditions can be quite different. However, there are real issues that arise when the concept of bifunctional reversibility is brought up, because the chemistry one reaction will often effectively destroy the activity of the catalyst for the other reaction, typically by irreversible surface modification. This can be understood in the context of softer alloys like the transition metal phosphides and sulfides, which are vulnerable to surface oxidation during OER catalysis, where there is preference for S-O or P-O formation as opposed to H_2O oxidation. If that layer is thick enough, that passivates the catalyst toward the HER/ORR reaction.

The versatility of molybdenum for creating complex compounds has proven to be a particularly advantageous in applications ranging from catalysis to electrochemical energy storage[12-16]. Part of the interest in these materials comes from the fact that there are myriad structural types and virtually limitless compositional possibilities. They have a wide range of possible stoichiometric compounds and phases formed, from oxides to

oxynitrides and nitrides, and typically can be made in high surface area morphology with relatively simple synthetic techniques (at least for the oxides) – e.g. co-precipitation, sol-gel, hydrothermal reaction. In addition, since molybdenum tends to form very stable oxides and is often an additive in corrosion resistant metal alloys, the ternary compounds are expected to have enhanced stability as well[17, 18].

In particular, the oxides of the form M'Mo_xO_y (M' = Mn, Fe, Co, Ni, Cu, Zn, Mg, Cd; x = 1, y = 4; x = 3, y = 8) have been extensively studied for their electrochemical storage properties relevant to lithium, sodium, and magnesium ion batteries[14]. One of the more attractive properties of these materials is the multitude of stable valence states for molybdenum, and the layered, relatively open structure of many of these compounds. As opposed to most oxides studied for lithium ion battery applications, molybdenum-based oxides have been studied as possible anode materials, meaning the reduction of the compound in conjunction with lithium incorporation is associated with the charging process rather than the discharge (i.e. the opposite of the process that occurs in $LiCoO_2$, $LiMn_2O_4$, etc…), meaning Mo in these systems favors losing an electron. Similar to the cathode materials studied extensively for Li batteries mentioned in previous chapters, transition metal molybdates have shown promise as oxygen electrocatalysts[19-22]. OER overpotentials for 10 mA cm^{-2} as low as 300 mV have been reported for nanoflower-like $CoMoO_4$ in alkaline solution, which also exhibited remarkable stability (retention of 100% activity over 16 hours)[19]. High-surface area was absolutely key to the apparent high geometric activity, but electrochemical impedance measurements also seemed to implicate conductivity as playing a role. Low intrinsic resistance and large capacitive values suggesting a high concentration of active sites have been found in other studies of

transition metal molybdates for oxygen evolution in alkaline electrolyte[20, 23, 24]. However, the existence of several polymorphs within a single compositional range, and the poor crystallinity of low-temperature synthesized samples[25] makes definitive assignments of structure-function relationships difficult.

Another class of ternary molybdenum compounds that have garnered great interest, especially in the field of catalysis are the nitrides (and to some extent, oxynitrides[26, 27]). Many groups have studied these compounds for hydroprocessing catalysis of various types – hydrodesulfurazation (HDS)[28, 29], hydrodenitrogenation (HDN)[30], etc… – and even for ammonia synthesis[13]. Of note, the ternary nitride Co_3Mo_3N was predicted, and subsequently experimentally verified to have higher activity for high-temperature ammonia synthesis than the highest activity noble or rare-earth elements known for this reaction, namely Ru and Os[31, 32]. This was ascribed to the complimentary electronic properties of Co and Mo (in simple terms electronegativity and oxophilicity) that put the N binding strength to a bimetallic CoMo compound right at the top of the volcano curve for that reaction. Mo tends to form N bonds that are too strong bonds (relative to MoO) and the limiting factor in ammonia synthesis is therefore thought to be the hydrogenation and desorption of the bound N intermediate. On the other hand, the Co-N bond is fairly weak, shifting the rate-determining step to the dissociation of the dinitrogen bond to form surface bound N atoms. The combination of Co and Mo in Co_3Mo_3N is argued to yield a more favorable balance between the energies of the adsorbed intermediates to affect ammonia synthesis in a facile manner. The implementation of this catalyst is hindered only by the difficulty in manufacturing the nitride as compared to the commercial Co-doped iron catalyst that is being used to

catalyze the Haber-Bosch process today (the use of Ru or Os catalysts has been relatively rare, but has been applied downstream of the main reactor).

The present study aims to investigate the potential benefits on catalytic activity of combining elements that have electropositive with those that have (relatively) electronegative properties within the d-block. Most often, the transition elements with valence electron counts of d^{4-6} form very stable inert oxides with d^0 electronic configurations, whilst those with electron counts if d^{7-11} have lower oxidation states, and will have weaker bonds to oxygen, due to the occupancy of the anti-bonding orbitals (in both 6-coordinate (O_h) and tetrahedral (T_d) ligand fields.

Several other groups have demonstrated this approach to be successful in a number of different catalytic applications, from electrocatalysis of the hydrogen evolution and oxygen reduction reactions (namely, on alloyed platinum and TM phosphide compounds)[33, 34], to the thermal catalysis involved in hydrodesulfurization[26, 35]. In the case of the electrocatalysis of the oxygen evolution reaction, a case could be made that the optimal balance in the iron-nickel oxide series is another example of this phenomenon. The binding energy of oxygen intermediates on $Ni_{1-x}Fe_xOOH$ is predicted to smoothly vary with composition between that of the pure Ni and Fe oxides, and agrees with experiments should distinct trends and peak activity (volcano)[36, 37]. For application in oxygen electrocatalysis, such as the water oxidation half-reaction, the goal is to obtain a catalyst that binds to the intermediates (-OH, -OOH, -OO) with comparable affinities (neither too strong nor too weak)[38, 39].

Herein we have synthesized the ternary compounds $CoMoO_4$ and $CoMoN_x$ and tested them as catalysts for the oxygen evolution and reduction reactions (OER/ORR).

We also tested their reversibility and whether they are susceptible to activity degradation (both chemical and electrochemical) as a result of catalysis. Nitrides and oxynitrides tend to also have better intrinsic conductivity than the corresponding oxides[40], which usually is implicated in better performing electrocatalysts, especially important to the oxygen reduction reaction[41].

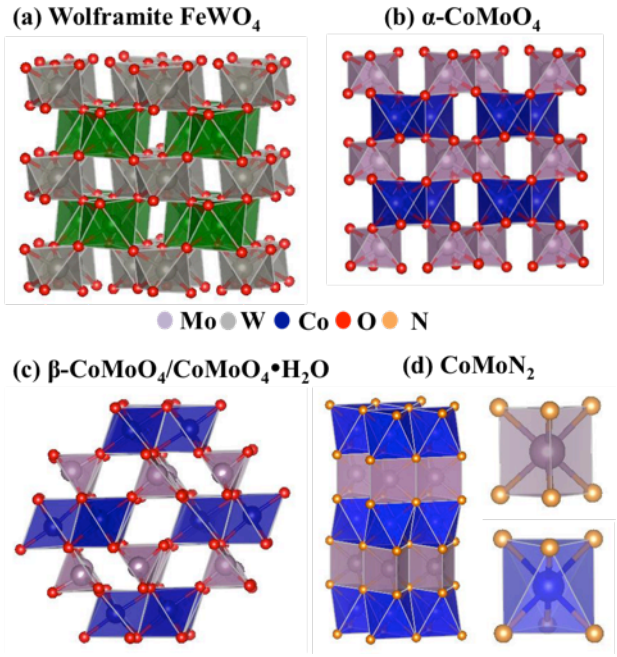

Figure 4.1 Polyhedral crystal structure representations of (a) Wolframite $FeWO_4$, (b) α-$CoMoO_4$, isostructural with Wolframite, (c) β-$CoMoO_4$, where Mo occupies tetrahedral sites, and (d) $CoMoN_2$ where Mo is at trigonal prismatic sites (inset, top), and Co is at trigonal antiprismatic sites (inset, bottom).

Cobalt-molybdenum oxide of the 1:1:4 stoichiometry has 2 polymorphs that are stable at room temperature: α-$CoMoO_4$, where Mo occupies octahedral positions (O_h) and is isostructural with Wolframite ($FeWO_4$), and β-$CoMoO_4$, where Mo is in tetrahedral sites (T_d symmetry) (**Figure 4.1**). The other aspects of the crystal structure do not differ between the two, as the two polymorphs exhibit a layered structure alternating Co and Mo oxide layers, and the coordination of Co remains the same (6-coordinate, distorted octahedral). The structures of the two polymorphs have been under much scrutiny[42-44], but the main conclusions are that the β-$CoMoO_4$ and H_2O-$CoMoO_4$, with similar Mo

coordination environments (T_d), produce better activity for hydroprocessing catalysis[45] and partial oxidation of hydrocarbons[46] than the α polymorph, where Mo is sitting in octahedral sites. We chose to take a representative from both structure types as controls to compare activity to the nitride $CoMoN_2$, which is similar in structure to α-$CoMoO_4$ (Mo O_h) (see **Figure 4.1**). Since the β polymorph is somewhat metastable (mechanical grinding can produce phase change), we used H_2O-$CoMoO_4$ to represent the oxide sample with. We also compared them to another nitride, Co_3Mo_3N, which has more metallic character (higher conductivity), and weaker M-N bonding. The results for performance of these compounds as bifunctional OER/ORR electrocatalysts is presented below.

4.2 Materials and Methods

Synthesis of solid-state $CoMoO_4$: For the synthesis of $CoMoO_4$, we adopted a simple solid-state procedure[26] where stoichiometric quantities of $CoCO_3$ and MoO_3 were ground together for 15 minutes to produce 1 g of powder and subsequently calcined at 780 °C for 6 hours. The resulting product comes out of the furnace as a blue-purple color indicative of the β polymorph. The size of the crystallites was >5 μm and the structure was confirmed by PXRD (**Figure 4.2a**). It was then ground thoroughly to produce the α-polymorph, which has a forest green color. The crystal transformation was investigated by PXRD and shown in **Figure 4.2a (**black and blue traces).

Synthesis of crystalline $CoMoO_4$ hydrate: To produce a higher surface area oxide, an adaptation of hydrothermal procedures from the literature was employed[16, 47]. The precursor for the hydrothermal reaction is made by precipitating 1 mmol $Co(NO_3)_2 \bullet 6H_2O$

with 0.14 mmol $(NH_4)_6Mo_7O_{24}•4H_2O$ or 1 mmol of $Na_2MoO_4•2H_2O$. The starting pH of this solution was typically 8 and was adjusted to between 6 and 7 using HNO_3 or NH_4OH. It is important in this procedure to control the pH and temperature (80 °C) of the precursor solution in order to get a crystalline phase of the appropriate stoichiometry from the hydrothermal treatment, as also found independently[45]. The resulting product was washed repeatedly with water, then ethanol, then dried for 2 hours at 100 °C. The hydrate product is hereby referred to as H_2O-$CoMoO_4$. It is important to not heat the hydrate product too high because the formation of β-$CoMoO_4$ occurs at relatively low-temperature[44].

Synthesis of Co_3Mo_3N and $CoMoN_2$ nitride compounds: Nitride compounds were synthesized via ammonolysis of the oxide hydrate described above. In a typical procedure, the precursor was placed in an alumina boat in the center of a tube furnace fixed with an ammonia flow apparatus. The ramp rate to dwell temperature was kept at a constant 5°C/min. The variables used to control the resulting phases were time, temperature, and NH_3 flow rate. To make Co_3Mo_3N, H_2O-$CoMoO_4$ (as prepared above) was used as a precursor and the reaction parameters were 750 °C for 12 hours with a 50 mL/min NH_3 flow rate[15]. To make $CoMoN_2$, Co_3Mo_3N is the precursor and reaction parameters are 400 °C for 1 hour with 150 mL/min NH_3[48]. The resulting powder was divided and washed in either ultra-pure water or in 2 M HCI to remove Co metal impurities. Both materials were characterized by PXRD and tested for OER/ORR catalysis.

Structural and Morphological Characterization: The structure of the different compounds synthesized was characterized with powder X-ray diffraction (PXRD), on a

Philips XPert diffractometer using Cu Kα radiation with a graphite monochromator, and a sample spinner. The verification of phase was conducted using PANalytical HighScore software with semi-quantitative analysis for identifying if secondary phases were present. Sample morphology was characterized with scanning electron microscopy on a Zeiss Field Emission SEM affixed with Oxford EDS for compositional analysis.

Electrochemical Characterization: Catalysts were characterized for OER and ORR in alkaline (0.1 M NaOH) and acid (0.5 M H_2SO_4) electrolytes with a custom 3-electrode cell where the reference and counter electrodes are separated from the working electrode compartment via a PFA tube bridge and an anion-exchange membrane, respectively. The inks used to make the films were made by ultrasonically mixing catalyst (10 mg), acetylene black (100 μL pipetted from a suspension of 15 mg/mL in ethanol), and neutralized Nafion[49] (100 uL, from a 3.33% by weight solution) in a 1:1 by volume ethanol:water mixture (800 μL) to make a final concentration 10 mg/mL catalyst. The catalyst was immobilized onto the working electrode using a standard drop-caste film technique described in many standard fuel cell/electrolyzer catalyst screening studies[49, 50]. Briefly, following drop-casting 10 μL of the catalyst ink onto the working electrode, it was cured by rotation at 400 rpm in air giving a catalyst loading 510 μg/cm^2. The working electrode was glassy carbon (GC, HTW Sigradur®) disk (0.196 cm^2) mounted on a rotating-disk electrode (RDE, Pine Instruments). We used a Ti counter electrode and a homemade manganese oxide reference for alkaline electrolyte (+210 mV vs NHE), and a homemade Ag/AgCl reference for acid electrolyte (+200 mV vs NHE), both calibrated against NHE. The typical rotation rate used is 1600 rpm unless otherwise indicated (as for Koutecky-Levich analysis). Electrolyte was either saturated with O_2

(bubbled with high-purity oxygen) to quantify activity or N_2 to look at the background electrochemical processes and/or catalyst capacitance. The potentiostats used in all experiments were a CH Instruments 700C or a Gamry Interface 5000E. Cyclic voltammetry (CV) was conducted between 0.05 and 1.0 V vs RHE at a sweep rate of 20 mV/sec for ORR and from 1.0 to 1.8 V vs RHE at a sweep rate of 10 mV/sec for OER. In addition, CV's from 0.05 to 1.8 V vs RHE were performed at 20 mV/sec to look at the effect of sweep direction on the catalyst activity (i.e. catalyst reversibility). All polarization curves shown are corrected for uncompensated resistance (iR-compensated). The double-layer capacitance (C_{dl}) was measured for each electrode/ink in base under N_2-purged conditions. The scan rate was varied between 10-500 mV/sec. We used electrochemical impedance spectroscopy (EIS) to look at the evolution of the catalyst working electrode film before and after excursions to oxidizing potentials (1.8 V vs RHE). The resulting spectra were analyzed in Gamry's Echem Analyst, and fit to a model to extract the film resistance, R_f.

X-ray Photoelectron Spectroscopy (XPS) Characterization: We used X-ray photoelectron spectroscopy to look at the electronic state of the $CoMoN_2$ catalyst surface, along with compositional information both before and after catalysis. To obtain spectra, we used a Thermo K-Alpha spectrometer with charge compensation, and calibrated against adventitious carbon and gold in the case where catalyst was deposited onto gold substrates. To prepare the pristine sample, a suspension of the material in ethanol was dropped onto a gold-sputtered glass slide, and dried at 100 °C overnight. For the post-catalysis samples, the spectra were collected on catalyst films following 500 cycles at either ORR or OER potential regimes. The glassy carbon discs (5 mm diameter, 4 mm

height) that served as the substrate working electrode during OER/ORR experiments was removed from the Teflon shroud of the RDE, rinsed with ultra-pure water, and dried at 100 °C overnight.

Electrochemical Corrosion Studies via ICP-OES: The alkaline electrolyte (0.1 M NaOH) in which samples were tested for activity was evaluated using inductively-coupled-plasma optical emission spectroscopy (ICP-OES) for corrosion products (e.g. Co^{2+} and $[MoO_4]^{2-}$). Standard curves were made using concentrations in the range of 100 ppb to 50 ppm, over which linear behavior was observed. Standard series were made by diluting SPEX CertiPrep standard solutions into 3% HNO_3.

4.3 Results

Characterization of structure and morphology of as-prepared cobalt-molybdenum oxides: The PXRD patterns of the different oxides of $CoMoO_4$ are shown in **Figure 4.2**. The solid-state synthesis method produced the expected majority monoclinic α-$CoMoO_4$ phase, denoted the SS-$CoMoO_4$ sample[51], with a very small (<5%) impurity of the β-$CoMoO_4$ polymorph that is deduced from the peak at $2\theta = 27.5°$. As expected for high temperature solid-state synthesis, the particle size of SS-$CoMoO_4$ is quite large (>5 μm) (**Figure 4.2b**).

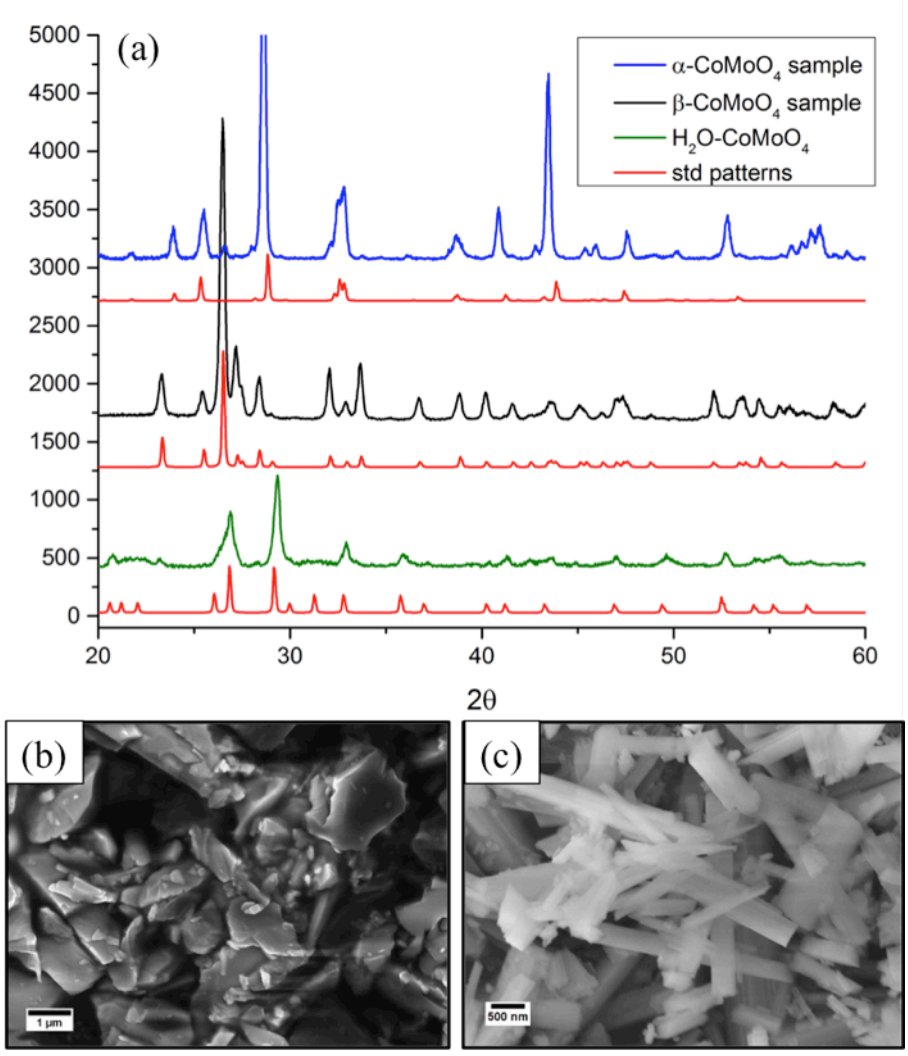

Figure 4.2 (a) PXRD patterns of the 3 polymorphs of cobalt molybdenum oxide α-$CoMoO_4$ (blue) β-$CoMoO_4$ (black) and the hydrate $CoMoO_4$•H_2O (green). Representative SEM images of the (b) α- and (c) hydrate polymorphs.

The PXRD and SEM of the hydrated sample, H_2O-$CoMoO_4$, is shown in **Figure 4.2**. There are a number of different procedures reported for making a crystalline hydrate from the precursor precipitates[1, 16, 19, 25, 47, 52, 53], but most report poor crystallinity or incorrect phases that do not match that of the true $CoMoO_4$•H_2O, the structure of which was relatively recently determined using XANES[44] and single crystal X-ray diffraction[25]. One of these nanoscopic/poorly crystalline morphologies was reported to be more active as OER catalyst than Co_3O_4[19]. But given the ill-defined composition/structure/surface

area, it is ambiguous to conclude what is responsible for the activity. The product produced herein is, by comparison, crystalline with uniform rod-like morphology and distinct sharp facets (**Figure 4.2c**). The rod diameter is of order of 500 nm, which is a significant size reduction from the SS-$CoMoO_4$. The PXRD pattern of the hydrated sample shows multiple small broad peaks not present in the standard pattern, but these could not be definitively assigned to either cobalt or molybdenum oxide phases, and the pattern is the same as that observed by Whittingham et al., who solved the single crystal structure. EDXS scans determined the atomic ratio of Mo:Co in both SS-$CoMoO_4$ and H_2O-$CoMoO_4$ to be very close to 1:1 (1.08 and 0.93, respectively).

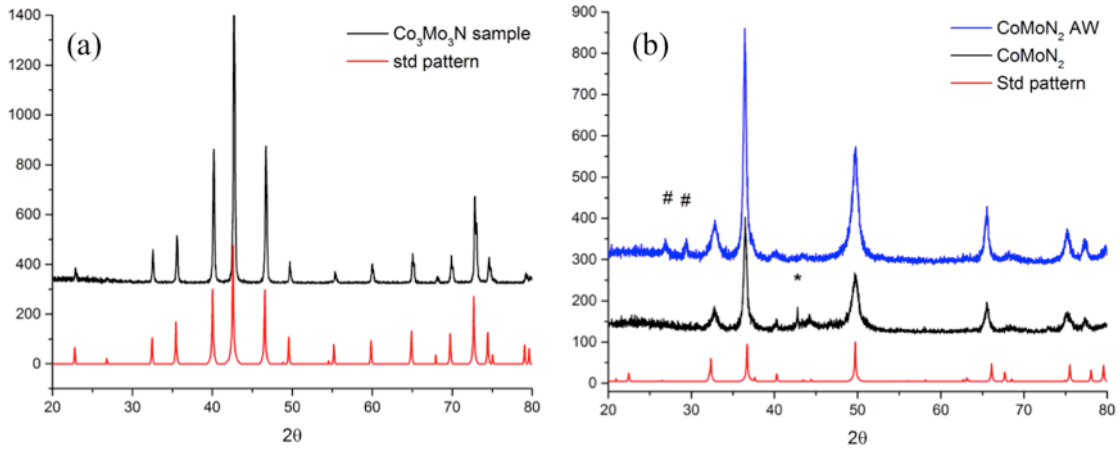

Figure 4.3 (a) PXRD pattern with reference of Co_3Mo_3N synthesized via ammonolysis of H_2O-$CoMoO_4$ and (b) PXRD patterns of the CoMoN2 both as-prepared (black), and acid-washed (blue). The # and * symbols represent CoMoO4 and Co metal impurities, respectively.

Characterization of cobalt molybdenum nitrides: The PXRD patterns of the two nitrides prepared from the oxides are shown in **Figure 4.3**. The synthesis of Co_3Mo_3N starting from the H_2O-$CoMoO_4$ precursor results in a highly crystalline phase pure product with no observable secondary phase (**Figure 4.3a)**. In spite of the high level of crystallinity however, the particle size actually decreases (**Figure 4.4a**), consistent with

previous reports of this synthesis[27, 54]. The rod-like morphology is retained on the order of 200-300 nm in width, but the rods become sintered at this higher formation temperature. The synthesis of $CoMoN_2$ from Co_3Mo_3N was done by ammonolysis at lower temperature – 400 °C for 1 hour. This approach results in further reduction in particle size upon transformation of Co_3Mo_3N to $CoMoN_2$. The as-prepared (crude) product is described first. Comparison of the PXRD to the reference $CoMoN_2$ confirms the crystal phase (**Figure 4.3b, black trace**), while the peak broadening indicates a smaller crystallite domain size than the rod-like morphology of the hydrate precursor (estimate from Scherrer equation ~20 nm). SEM images of the as-prepared and acid-washed $CoMoN_2$ product (**Figure 4.4b-d**) show a narrow range of crystallite sizes (50-100 nm range) that aggregate into an open porous network with sponge-like morphology. SEM of the pristine $CoMoN_2$ sample also reveals very few darker objects of the same size, indicating a more conducting impurity, hence possibly metallic. Consistent with the SEM, PXRD of the as-prepared $CoMoN_2$ indicates a small level of a metallic Co impurity (**Figure 4.3b**, indicated by *). Previous reports suggest that Co does not fully occupy the CoN_6 layers, and some of the Mo goes into the Co sites (regardless of precursor stoichiometry), thus leaving a Co metal impurity[18, 55].

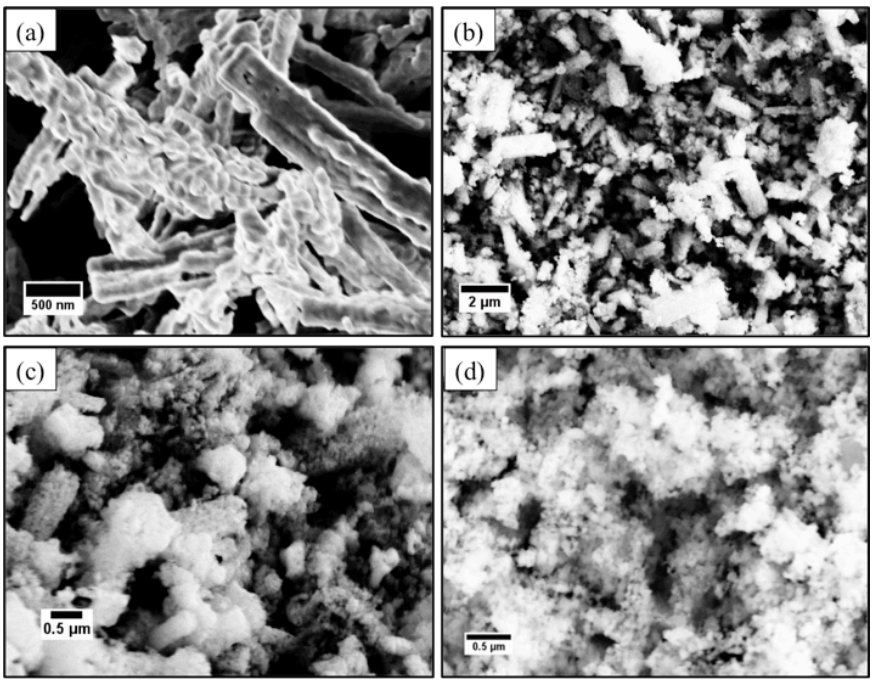

Figure 4.4 SEM images of nitrides prepared from oxide precursors. (a) Co_3Mo_3N exhibiting agglomerated crystallites in nanorod morphology (b) Pristine $CoMoN_2$ nanoparticles retaining some of the rod-like morphology of the precursor, and (c) a zoomed in view of $CoMoN_2$. (d) Acid-washed $CoMoN_2$ sample, named $CoMoN_2$-AW, showing uniform crystallites (50-100 nm range) that aggregate into an open porous network with sponge-like morphology.

Acid-Treatment of $CoMoN_2$ nitride: Because of dispute about the structure and composition of $CoMoN_2$ in the literature[48, 55, 56] (as well as the isostructural $FeMoN_2$[18, 57]), we conducted a washing procedure that consisted of sonicating the as-prepared $CoMoN_2$ sample in 2 M HCl purged with N_2 to dissolve any metallic Co impurities that may be present, as indicated in the PXRD. The resulting material was dubbed $CoMoN_2$-AW (acid wash). The PXRD pattern is shown in **Figure 4.3b,** blue trace. The acid treatment was able to effectively eliminate the metallic Co impurity, but the growth of a small impurity is revealed by peaks at $2\theta = 27$ and 29° (**Figure 4.3b**, blue trace, #). These peaks are likely indicative of the formation of a small amount of H_2O-$CoMoO_4$ that precipitates once the pH of the washing solution is neutralized. Compositional analysis by EDXS also showed a diminished Co content, decreasing the initial Co:Mo ratio from 0.93 to 0.3 –

and quantitative XPS yields 0.1. The effect of the acid-treatment on electrocatalytic activity was assessed and the two $CoMoN_2$ samples are compared below. The acid treatment was not detrimental to the nitride phase (only metallic Co), as molybdenum nitrides are acid-stable, as is the corresponding $FeMoN_2$ structural analogue[18] of $CoMoN_2$.

Electrocatalytic activity toward oxygen evolution/reduction: We compared the electrocatalytic activities of the series of cobalt-molybdenum oxide/nitride compounds in alkaline electrolyte (0.1 M NaOH) using an RDE setup to obtain diffusion-limited O_2 reduction currents and OER currents that are not mass transport limited. The results are graphed in **Figure 4.5**. All polarization curves for ORR have been corrected for background capacitance current (N_2-purged sweep subtracted from O_2-saturated current), and all OER curves are capacitance corrected by averaging forward and reverse sweeps of the CV traces. We ran commercial Pt@C and Ir@C (Premetek Co.) controls for the ORR and OER, respectively, which agreed with literature reports[58, 59]. For oxygen reduction, the best catalyst among the series was $CoMoN_2$, which had a ~100 mV lower onset potential than Pt (i.e. 100 mV *greater* overpotential), and reached a limiting current density of 4.5 mA/cm^{-2}. By contrast, the C_3Mo_3N nitride showed practically no activity for oxygen reduction. The two oxides SS-$CoMoO_4$ and H_2O-$CoMoO_4$ had very comparable onset potentials and limiting current densities between these two, with H_2O-$CoMoO_4$ performing slightly better, likely attributable to the enhanced surface area. With regard to oxygen evolution, three of the four catalysts have indistinguishable activity, reaching 10 mA cm^{-2} at η = ~400 mV. The SS-$CoMoO_4$ shows a later onset potential (50 mV), but similar profile curve, again suggesting the smaller surface area a factor. The

OER Tafel slope was measured for the nitride catalysts to be ~90 mV/dec, and that for the oxides is 60 mV/dec, meaning the initial kinetics for oxygen evolution slows when switching from an oxide surface to a nitride one. The important catalyst metrics, including Tafel slopes, are summarized in **Table 4.1**.

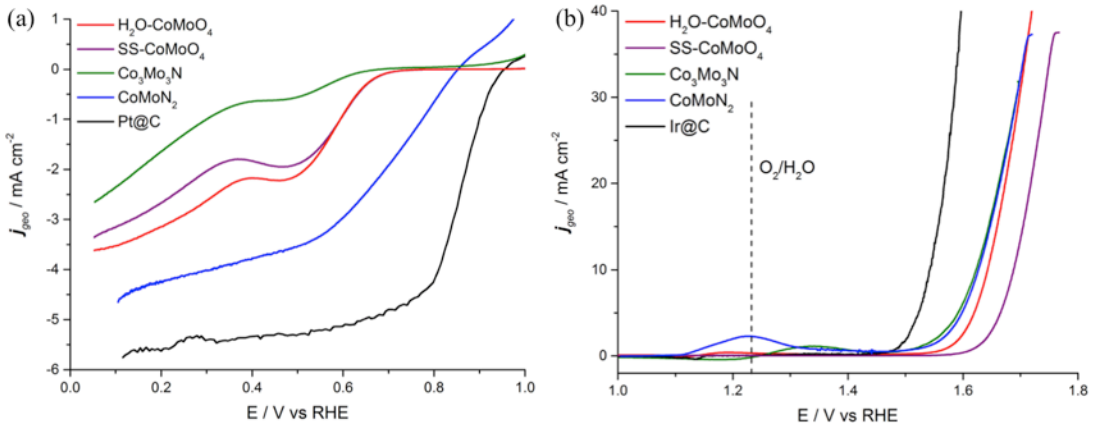

Figure 4.5 (a) ORR polarization curves in 0.1 M NaOH of CoMo(O,N) series of catalysts, 1600 rpm, O_2-saturated, scan rate 20 mV/sec, N_2-background corrected, iR-compensated. (b) OER polarization curves in 0.1 M NaOH, capacitance-corrected by averaging forward and reverse CV sweeps, iR-corrected, 1600 rpm.

To assess whether the surface area had a significant impact on activity, the double layer capacitance (C_{dl}) was measured for all four catalysts in base in a potential window where no Faradaic current was passed. The best potential window was between 0.1-1.0 V vs RHE under N_2-purged conditions, where catalyst instability was not a factor. The scan-rate dependence of the charging current for $CoMoN_2$ is shown in **Figure 4.6**. The C_{dl} values for all four catalysts did not change much, with the exception of Co_3Mo_3N, which had close to twice the value for C_{dl} than the other three (**Table 4.1**). It is interesting to note that the values do not change much given the differences in apparent morphology by SEM. This is most likely due to the intrinsic conductivity differences between the catalysts, notably the oxides and $CoMoN_2$ compound being much more insulating than Co_3Mo_3N, which is metallic[15]. Although C_{dl} can be informative, it should not be used as a

surface area comparison across compounds that differ significantly in composition, structure, or conductivity a sentiment that was cautioned long ago, but is now increasingly recognized in the literature[60-62].

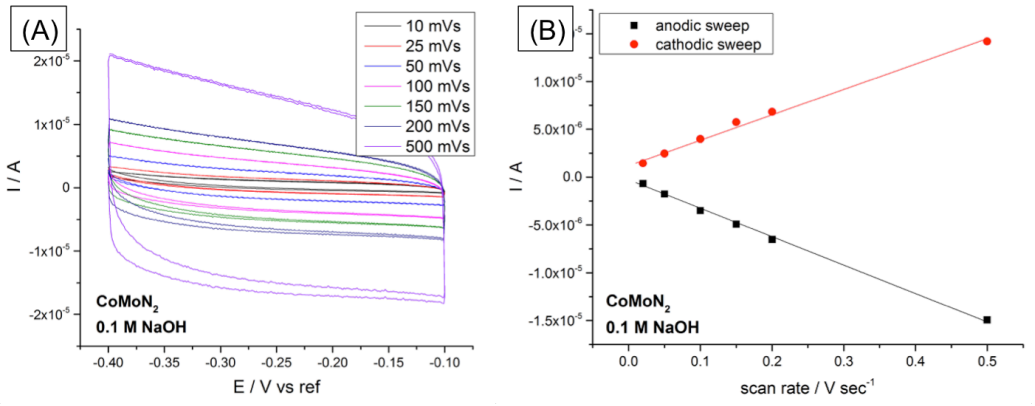

Figure 4.6 Double-layer capacitance (C_{dl}) measurements for $CoMoN_2$ compound in 0.1 M NaOH in N_2-purged electrolyte.

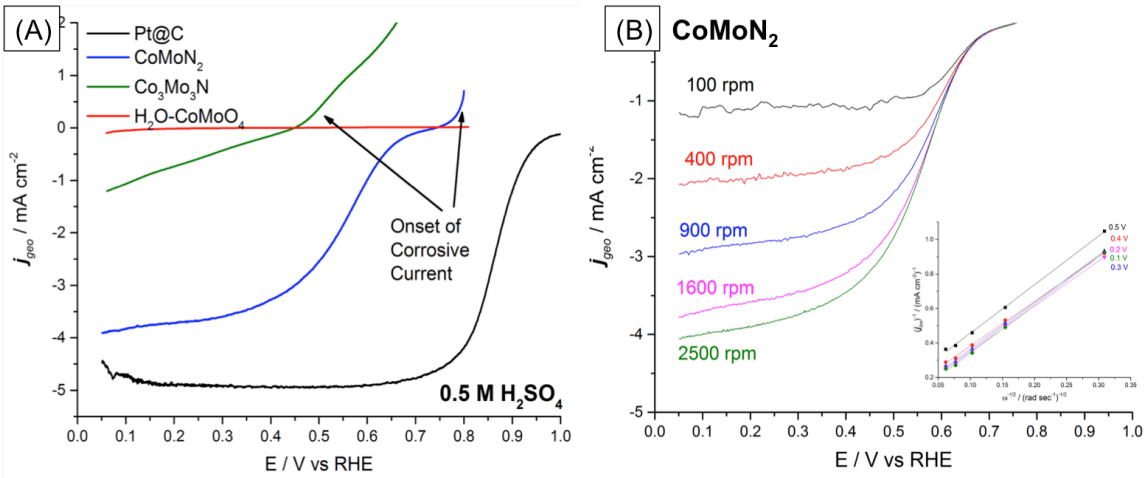

Figure 4.7 (a) ORR polarization curves in 0.5 M H_2SO_4, O_2-saturated, 1600 rpm, N_2-background corrected, iR-corrected. (b) Koutecky-Levich analysis for $CoMoN_2$ in O_2-saturated 0.5 M H_2SO_4 electrolyte (N_2-background corrected, iR-corrected). Inset shows j^{-1} vs $\omega^{-1/2}$ used to determine *n*, number of electrons.

Since $CoMoN_2$ had the best bifunctional performance in alkaline electrolyte ($\Delta E_{orr/oer}$ = 1 V, the potential difference between +10 mA/cm^2 and -3 mA/cm^2), we decided to investigate its performance further. The catalytic activity in acid (0.5 M

H_2SO_4) was tested against Pt and Co_3Mo_3N (the oxides are completely inactive). Once again it showed good performance as an ORR catalyst with an onset potential 300 mV lower than Pt (**Figure 4.7**). A Koutecky-Levich analysis was performed, in which the rotation rate of the RDE is varied and the resulting limiting current (j_L) obtained should vary linearly with the square root of the rotation rate (ω). If the inverse of *j* at a given potential is plotted against $\omega^{-1/2}$ the slope of the line thus obtained can be used to find the number of electrons transferred, which should be 4 for an ideal O_2-reduction catalyst[63]. The relation is the following:

$$\frac{1}{j} = \frac{1}{j_k} + \frac{1}{j_L} = \frac{1}{nFAkC} + \frac{1}{0.62nFAD^{\frac{2}{3}}\upsilon^{-\frac{1}{2}}C\omega^{\frac{1}{2}}}$$

In the above equation, *n* is number of electrons, *F* is the Faraday constant, A is the electrode area, D is the diffusion coefficient for O_2, υ is the kinematic viscosity for O_2, C is the dissolved O_2 concentration, and ω is the rotation rate. The parameters for the diffusion, concentration, and viscosity of O_2 for a given electrolyte can be obtained from the literature or database[63, 64]. In **Figure 4.7b**, we plot the ORR curves for several rotation rates, and the Koutecky-Levich curves for various potentials are shown in the inset. The number of electrons obtained for $CoMoN_2$ in acid is 3.9±0.14, which is very close to ideal, meaning the 2-electron pathway of H_2O_2 formation is not significant.

Table 4.1 Important catalyst metrics for CoMo(O,N) series of compounds. Activity for OER/ORR in alkaline electrolyte.

Catalyst	$E_{1/2}$ ORR (V vs RHE)[(a)]	Tafel Slope, OER (mV dec^{-1})	η @ 10 mA cm^{-2} (mV)	C_{dl} (uF cm^{-2})	$\Delta E_{ORR/OER}$ (V)[(b)]
H_2O-$CoMoO_4$	0.59	64	410	190	1.41
SS-$CoMoO_4$	0.60	60	460	190	1.55
Co_3Mo_3N	0.53	98	390	390	n/a
$CoMoN_2$	0.70	90	400	144	1.02

(a) $E_{1/2}$ in this case is determined by taking the potential at which *j* is ½ of what is it @ 0.4 V vs RHE.
(b) $\Delta E_{ORR/OER}$ is defined as the difference between the potentials at which OER *j* = 10 $mAcm^{-2}$ and ORR *j* = 3 $mAcm^{-2}$

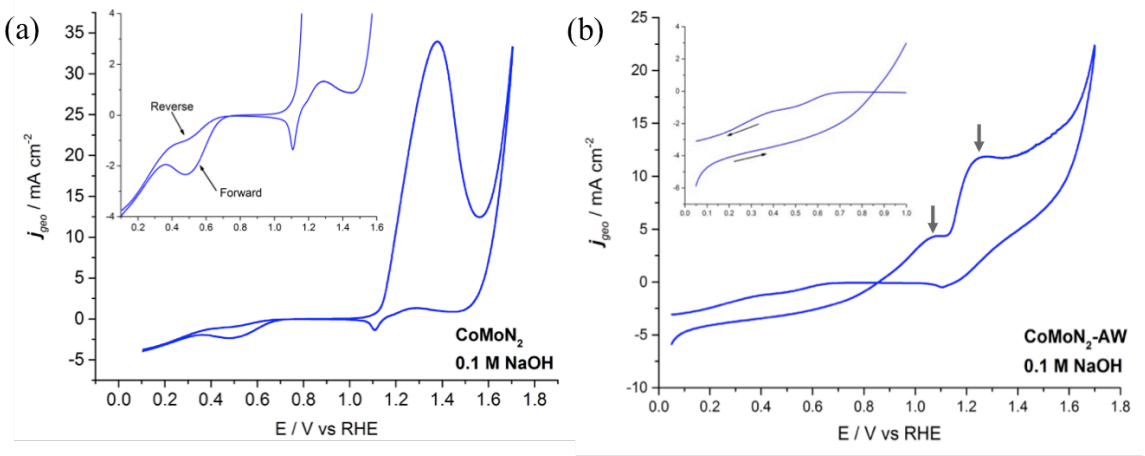

Figure 4.8 ORR ➔ OER CV in alkaline electrolyte that shows the large pre-OER oxidation feature as well as the hysteresis for ORR activity for (a) $CoMoN_2$ (pristine) and (b) $CoMoN_2$-AW. (O_2-saturated, 1600 rpm, 20 mV/sec scan rate)

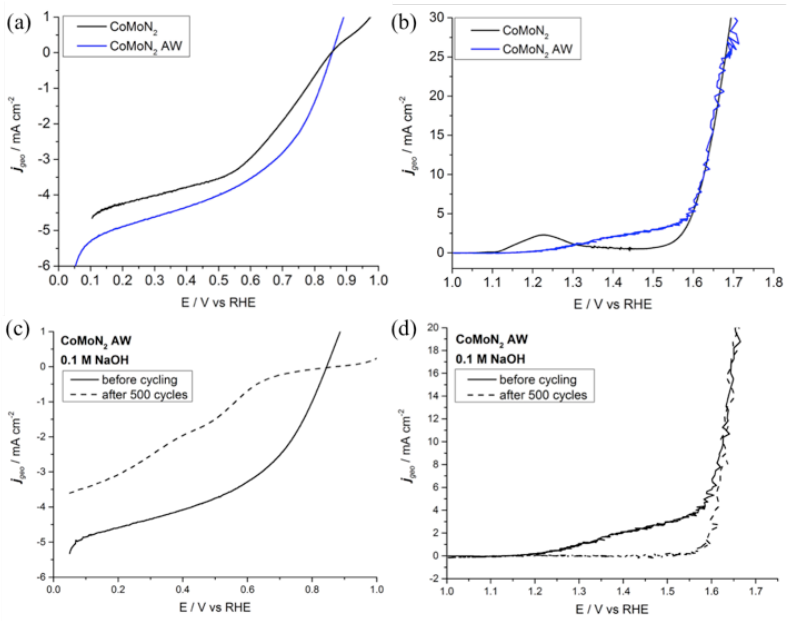

Figure 4.9 Comparison of pristine $CoMoN_2$ catalyst with the acid washed sample $CoMoN_2$-AW (a) ORR and (b) OER polarization curves in 0.1 M NaOH. The cycling stability for $CoMoN_2$-AW before and after 500 cycles in the ORR (c) and OER (d) potential range.

We also investigated the effect of the acid wash to remove metallic Co had on catalysis. The results in alkaline electrolyte are shown in **Figure 4.9a,b**. Interestingly, the activity was not significantly affected by this treatment, but resulted in slightly different outcomes for both ORR and OER catalysis. The onset potential for ORR improved by ~50 mV, and $CoMoN_2$-AW had a higher limiting current density (**Figure 4.9a**). On the OER side, the pre-catalytic oxidation feature was significantly broadened, but the catalytic activity was extremely similar (**Figure 4.9b**). The origins of this effect will be discussed below, in context with the XPS results.

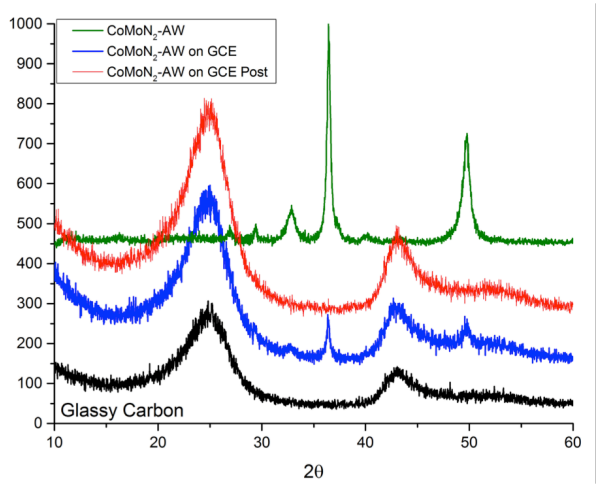

Figure 4.10 PXRD of the electrode film immobilized on a glassy carbon substrate before (blue) and after (red) excursion to oxidizing potential.

XPS Characterization of "before and after catalysis" $CoMoN_2$: The surface of $CoMoN_2$ was characterized before catalysis, and after exposure to ORR potentials, and subsequently, OER potentials in alkaline conditions. The reason this was performed is because the nitride has a very significant pre-OER oxidation feature in the CV profile indicative of either corrosion (loss of surface atoms), or extensive surface and sub-surface oxidation (**Figure 4.8**). When integrated, the oxidative peak yields a charge of 0.3 C/cm^2. This area is equivalent to oxidizing 40% of the total metal content (Co and Mo) by 1 electron, or extracting 6% of the total lattice N^{3-} as N_2. This peak coincides with the appearance of hysteresis in the ORR current, where a significant deactivation is seen following excursions to oxidative potentials (>1.2 V vs RHE). This phenomenon occurs with both the pristine and acid washed samples (**Figure 4.8a,b**). In addition, a significant loss of crystallinity is observed as by PXRD of the electrode (see **Figure 4.10**). Thus, the charge passed is likely leading to an irreversible process that could eliminate ORR active surface sites.

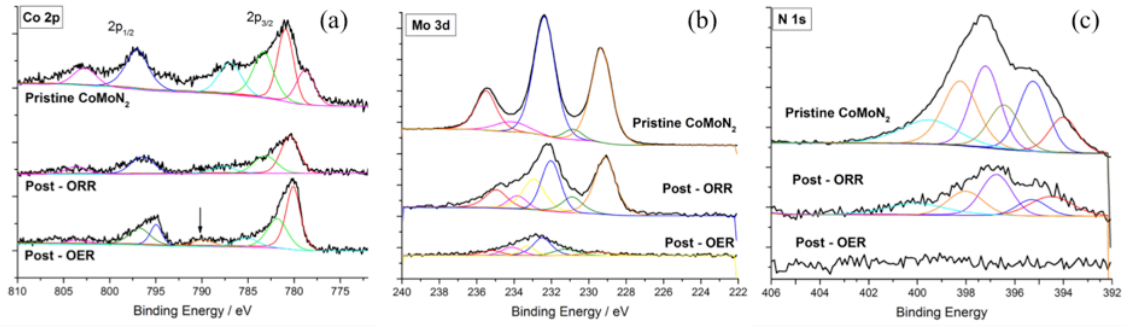

Figure 4.11 XPS spectra of (a) Co 2p (b) Mo 3d and (c) N 1s for $CoMoN_2$-AW before and after ORR/OER. The deconvoluted peaks are color-matched to indicate which species corresponds to which in the different samples. Arrow in (a) indicates formation of well-defined $Co^{3+/4+}$ satellite feature.

The results of the XPS analysis for all three stages (pristine, post-ORR, post-OER) are shown in **Figure 4.11**. The first semi-quantitative trend observed is that the Mo(3d) and the N(1s) signals become less intense after catalysis, and in the case of N, the signal completely washes out after excursion to OER-relevant potentials. The shape of the Co(2p) peaks also change post-catalysis. Of note is the Co($2p^{3/2}$) peak at 779.3 eV, assigned to Co^{2+} [65, 66], which disappears, and the peak at 781.5 eV (Co^{3+}) shifts to 781.0 eV (post ORR) and to 780.6 eV (post OER) (**Figure 4.11a**). The appearance of a more defined satellite peak at B.E. 790.4 eV is indicative of Co oxidation (i.e. mixed valency $3^+/4^+$), as occurs in higher oxidation state cobalt oxides like delithiated $LiCoO_2$[67].

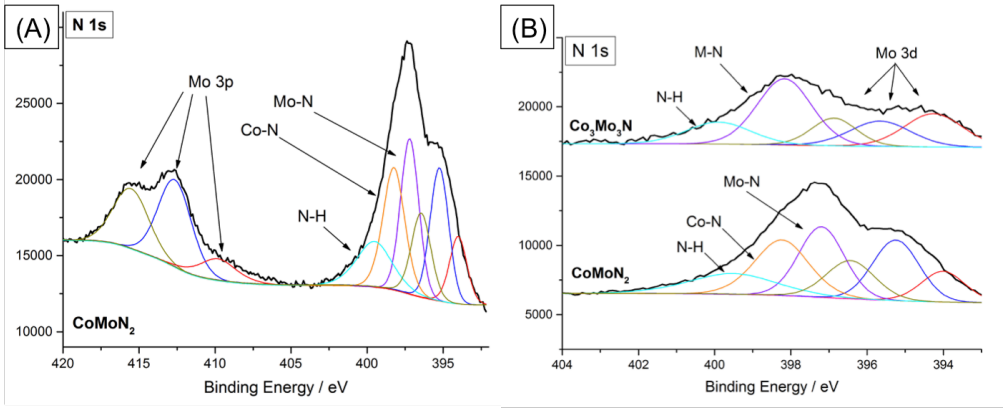

Figure 4.12 (a) Full N 1s spectrum for $CoMoN_2$-AW showing the contributions from Mo 3p peaks (red, blue, brown traces), and (b) N 1s comparison between pristine samples of $CoMoN_2$-AW (bottom) and Co_3Mo_3N (top). $CoMoN_2$ shows 2 M-N species indicative of both Co-N and Mo-N bonding.

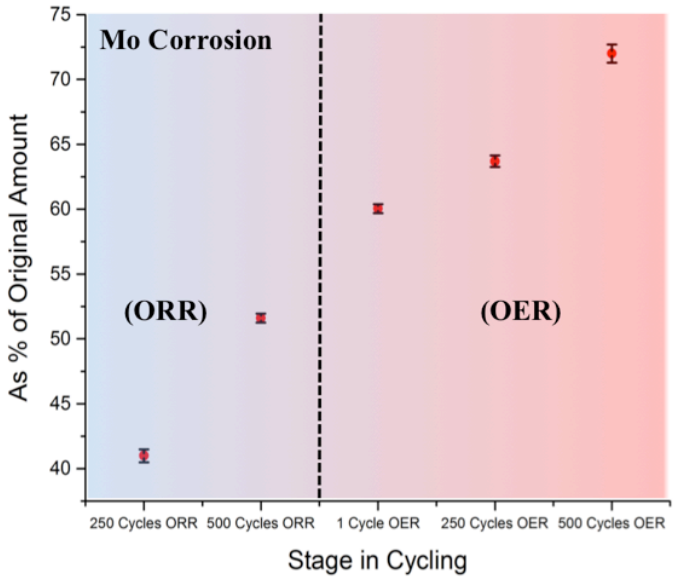

Figure 4.13 Chemical dissolution of molybdenum from the $CoMoN_2$-AW catalyst as measured by ICP-OES at various stages during activity testing – after cycling in ORR/OER regimes. Dissolution is reported as percent of original Mo in catalyst. Error bars are indicated by black markers.

The nitride peaks reveal important information about the evolution of the $CoMoN_2$ surface as well. However, the importance of deconvoluting the spectra in order to account for the Mo(3p) peaks must be stressed[56, 65]. The full N(1s)/Mo(3p) spectrum for $CoMoN_2$ is shown in **Figure 4.12a**. Of note are the 3 peaks at higher binding energy (>405 eV) paired with three peaks in the lower binding energy region, where the N(1s) features are found. Remaining are three additional N features, two of which belong to nitride M-N type bonding, one located at 397.74 eV, and the other at 398.78 eV. Based upon the previous assignments of MoN compounds[56, 68], we assign the peak at lower B.E. to Mo-N, and the higher one to Co-N. This agrees well with the comparison of B.E. in Co_3Mo_3N (spectra compared in **Figure 4.12b**), where almost no direct M-N bonding is possible as seen in the crystal structure (Co-N distance >3 Å). The M-N peak in that sample is at 398.1 eV. These assignments are consistent with the literature on nitride

compounds, where stronger bonding nitrides like TiN tend to have M-N B.E. closer to 397 eV[65, 69].

Corrosion analysis via ICP-OES: We followed up the surface analysis by looking into corrosion products in the electrolyte. It should be noted that catalyst stability can often be obscured when looking into the current-potential relationship with time. Very few studies try to make the link between electrochemical stability, and true chemical stability[70, 71]. In order to fully understand the link, we looked for dissolved Co^{2+} and $[MoO_4]^{2-}$ in the alkaline electrolyte in which activity was examined. The results are shown in **Figure 4.13**. There was no detectable Co leached into solution above the background electrolyte, but there was significant Mo detected. We found that regardless of cycling in ORR or OER regimes, the Mo continually leached into solution, until close to 75% of the total Mo content in the catalyst was observed. We do not observe a potential dependence, and therefore believe that the corrosion is chemical, or the moderately positive potentials at which ORR is tested (i.e. >0.1 V vs RHE), is sufficient to oxidize and hydrolyze molybdenum under alkaline conditions.

Taken together with the XPS spectra of Co and Mo, the $CoMoN_2$ samples undergo extensive surface changes and bulk corrosion upon polarization to both moderate oxidizing potentials (<1.2 V vs RHE) during ORR, and to more severe potentials relevant to OER (>1.2 V vs RHE). The lattice nitrogen (XPS, B.E. 397.7 and 398.8 eV) disappears from the surface concomitant with a large oxidation feature in the CV. The state of Co and Mo change significantly, with a partial Co enrichment relative to Mo, and the formation of a higher valent $Co^{3/4+}$ oxide at the surface, most likely responsible for OER catalysis and deactivating for ORR catalysis.

Electrochemical Impedance Spectroscopy (EIS) of $CoMoN_2$ films: Finally, we conducted EIS of catalyst films to probe the effects of oxidation on the electronic state of the working electrode catalyst films. The results are presented in Nyquist plot format in **Figure 4.14**. EIS can probe the different contributions to the overall impedance of a given system by imposing an AC perturbation of varying frequency on top of an applied DC voltage. This voltage perturbation, elicits responses from different electrical components of a system depending on their resistance and capacitance (RC) properties which give rise to characteristic time constants in the circuit[72]. It can be very useful for analyzing electrocatalyst kinetics[73-75], but also RC time constants of static films[76-78].

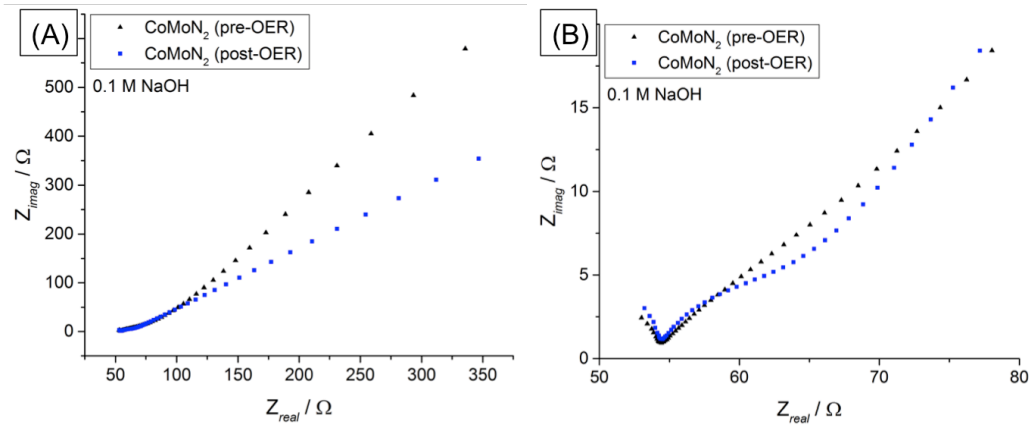

Figure 4.14 EIS spectra of $CoMoN_2$ catalyst taken before (black) and after (blue) excursions to OER-relevant potentials. (a) Zoomed-out view showing full frequency range (100 mHz – 500 kHz) and (b) zoomed-in view showing inflections in the curves indicating different electrochemical responses

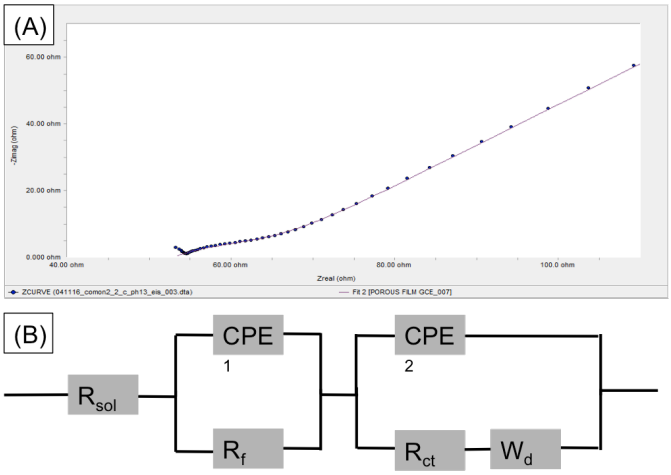

Figure 4.15 (a) Fitting of EIS spectrum of $CoMoN_2$ after excursion to OER potentials of 1.65 V vs RHE (blue trace, **Figure 4.14**) (b) the equivalent circuit for catalyst films immobilized on glassy carbon working electrodes.

Here we looked at the impedance spectra of the $CoMoN_2$ immobilized porous films on a glassy carbon electrode poised at the open circuit potential in the frequency range of 100 mHz - 500 kHz, before and after polarizing to oxidative potentials (>1.2 V vs RHE). We chose a potential where minimal or no catalytic current should be present that could complicate the interpretation. The results show a change in the slope of the spectra, implying a lower overall impedance (Z) for the film post-OER (blue squares, **Figure 4.14a**). This impedance decrease occurs across all voltage frequencies, implying it reflects a feature of the entire film and not a localized defect. Zooming in at higher frequency range (**Figure 4.14b**), one can see that there is a change in the shape of the spectra as well, with the post-OER curve showing an earlier inflection in what appears to be a semicircle. That inflection is also present in the pre-OER curve, but is more gradual.

To make a more quantitative comparison, the spectra were fit to a model that should capture all the important chemical/electronic processes without overfitting the data. The equivalent circuit is shown in **Figure 4.15**, along with the fitted data for the post-OER curve. The model is constructed with a solution resistance, R_{sol}, and two

parallel circuits in series. The first represents the film impedance, with R_f and CPE_1 being the resistance and capacitive elements. The second is a parallel circuit representing the diffuse electrolyte double layer, as well as any residual charge transfer between electrode/electrolyte interface, such as pseudocapacitance (R_{ct}, CPE_2, and W_d). The circuit elements R, CPE, and W correspond to resistors, constant phase elements (non-ideal capacitors), and Warburg diffusion, respectively. The model fits the data well, and the resulting R_f values obtained were 76 and 14 Ω for the pre and post-OER films, respectively. The film resistance was effectively lowered by 5x, while the solution resistance stayed the same (53 Ω).

4.4 Discussion

The evaluation of the electrocatalytic activity of the series of CoMo(O,N) compounds presents an interesting correlation. The apparent activity of these materials for ORR catalysis is dependent on both structure and composition, but less so for OER, where differences in activity seemed to be mostly linked to surface area. The $CoMoN_2$ nitride illustrates by far the best activity for ORR in both alkaline and acid electrolyte, and it can be enhanced when the material is acid-washed to remove Co metal impurities and enrich the surface Mo. Taken together with the compositional data from XPS, as well as the poor ORR activity from Co_3Mo_3N, the determining factors for high ORR activity are having a strong M-N interaction, and higher content of surface Mo atoms that play a direct role in the reduction of O_2. These conclusions are consistent with previous reports regarding oxygen reduction on molybdenum-containing nitrides[27, 55]. A somewhat surprising finding though is the more conductive nitride Co_3Mo_3N shows very poor activity. In addition, the conductivity through the film has an inverse correlation with

ORR activity, where oxidizing potentials caused a permanent decrease in the overall film resistance, and coincided with a significant loss of ORR. Therefore, the effect of nitrogen on the overall catalyst conductivity is not contributing to catalysis of ORR, while its interaction with the active site metal (Mo) through substrate oxygen binding is a descriptor of ORR activity. The detrimental consequences of high intrinsic conductivity of catalysts for multi-electron/proton reactions has been attributed before to the greater losses from charge recombination that occur[79].

For OER catalysis, we see the activity of the series is quite similar with the exception of SS-$CoMoO_4$. Three of the four catalysts show overpotentials for 10 mA cm^{-2} at 400 mV, with Tafel slopes between 60-90 mV/dec^{-1}, and mass activities of ~20 mA mg (η = 400 mV), comparable to the best crystalline unsupported Co-based catalysts[79-81]. The reason for this remarkable activity can be explained by the interesting properties of Co^{2+} in these materials. A recent review of catalytic trends in perovskites has pinpointed a significant property that correlates very well with activity[82-84]. The activity of a large series of perovskite OER catalysts shows that the covalent hybridization of unoccupied metal *3d* orbitals with the filled oxygen *2p* orbitals increases with activity[84]. The trend between bond strength and OER activity is consistent with similar observations implicating metal *3d* e_g orbital occupancy being an important descriptor for activity[85]. The hybridization of O *2p* with M *3d* orbitals can be measured by integrating the O K-edge X-ray absorption spectrum[86], and the integrated area increases with higher d-electron count in metals of the same oxidation state, suggesting more electronegative metals (moving right across the d-block) have greater O 2p-M *3d* orbital hybridization. This trend holds true also when the same metal increases in oxidation state. For example,

in $CoMoO_4$ the Co is in the 2+ O.S., but it is low-spin (t_{2g}^6 e_g^1) [44], and the O K-edge absorption spectrum is more comparable to that of $LaCoO_3$ (Co^{3+}, intermediate spin t_{2g}^5 e_g^1), than it is to CoO[87], where Co^{2+} is high-spin (t_{2g}^5 e_g^2). This indicates that the interaction of the electropositive Mo^{6+} (d^0) alters the electronic state of Co, increasing the hybridization with the O *2p* orbitals resulting in a more active Co^{2+} catalyst for the oxygen evolution reaction.

The catalyst with the best bifunctional activity, $CoMoN_2$ ($\Delta E_{ORR/OER}$ = 1 V vs RHE), also demonstrates high OER activity. However, the nitride influence on activity is less clear, since the XPS characterization of the $CoMoN_2$ catalyst post-OER showed that the surface character is closer to that of an oxide. In fact, characterization of the Co_3Mo_3N material revealed similar results for the nature of the surface. One can deduce from this information that the efficient OER catalysis is accomplished by a thick Co oxide surface layer that is formed via the partial decomposition of the nitride concomitant with Mo corrosion. The oxide contains Co in a relatively high oxidation state ($^{3/4+}$), and contains very little Mo. It also is more conductive *in situ* than the material it original form, which is consistent with previous observation for Co-oxides containing mixed 3/4+ valence like delithiated $LiCoO_2$[88-90]. It has been observed in some nitrides/oxynitrides used in photoelectrochemical water splitting that the valence band holes created in these semiconductors would rather react with nitride N^{3-} to produce N_2 rather than oxidize H_2O[91, 92]. It is apparent that this process cannot be avoided in these intermetallic nitrides as well, and the deactivation for ORR is directly related to this irreversible process.

4.5 Conclusions

In summary, we synthesized and tested a series of cobalt-molybdenum oxides/nitrides to evaluate their performance as bifunctional oxygen electrocatalysts. It was predicted that these materials would posses the ideal properties for catalysis because of the synergy of Co and Mo, as well as the incorporation of lattice nitride to tune the binding affinity for oxygen, making an improved ORR catalyst. The $CoMoN_2$ compound, with strong M-N interactions, as well as nanoparticulate morphology, shows significant activity for both OER and ORR catalysis. However, its reversibility is hampered due to irreversible structural and chemical changes to its surface when exposed to oxidizing potentials, where a substantial cobalt oxide layer is formed. The result is severely diminished ORR activity. To mitigate these effects, new catalysts with increased M-N interaction must be developed that still preserves high activity, or compounds that can be reversibly oxidized/reduced at their surface in the catalytically relevant potential windows such that passivation toward the reverse reaction will not occur, nor bulk corrosion.

4.6 Acknowledgements

This work was supported by DOE Small Business Innovation Research (SBIR), award number DE-SC0013179, and partial support from NSF Chemical, Bioengineering, Environmental, and Transport systems (CBET) award number 1433492. We would also like to acknowledge support from a National Science Foundation Integrative Graduate Education and Research Traineeship NSF-IGERT award number 0903675 fellowship, Sustainable Fuel Solutions for the 21st century (G.G.).

The authors declare no conflict of interest.

4.7 References

References

1. J. Pettersson, B. Ramsey and D. Harrison, *Journal of Power Sources*, 2006, **157**, 28-34.
2. J. W. Desmond Ng, Y. Gorlin, T. Hatsukade and T. F. Jaramillo, *Advanced Energy Materials*, 2013, **3**, 1545-1550.
3. S. Park, Y. Shao, J. Liu and Y. Wang, *Energy & Environmental Science*, 2012, **5**, 9331-9344.
4. M. Hamdani, R. N. Singh and P. Chartier, *Int. J. Electrochem. Sci*, 2010, **5**, 556-577.
5. M. Risch, K. A. Stoerzinger, S. Maruyama, W. T. Hong, I. Takeuchi and Y. Shao-Horn, *Journal of the American Chemical Society*, 2014, **136**, 5229-5232.
6. J. Masa, W. Xia, I. Sinev, A. Zhao, Z. Sun, S. Grutzke, P. Weide, M. Muhler and W. Schuhmann, *Angew. Chem. Int. Ed.*, 2014, **53**, 8508-8512.
7. T. Maiyalagan, K. A. Jarvis, S. Therese, P. J. Ferreira and A. Manthiram, *Nature communications*, 2014, **5**, 3949.
8. W. G. Hardin, D. A. Slanac, X. Wang, S. Dai, K. P. Johnston and K. J. Stevenson, *The Journal of Physical Chemistry Letters*, 2013, **4**, 1254-1259.
9. H. Jin, J. Wang, D. Su, Z. Wei, Z. Pang and Y. Wang, *Journal of the American Chemical Society*, 2015, **137**, 2688-2694.
10. M. Tahir, N. Mahmood, X. Zhang, T. Mahmood, F. K. Butt, I. Aslam, M. Tanveer, F. Idrees, S. Khalid, I. Shakir, Y. Yan, J. Zou, C. Cao and Y. Hou, *Nano Research*, 2015, **8**, 3725-3736.
11. L.-A. Stern, L. Feng, F. Song and X. Hu, *Energy & Environmental Science*, 2015, **8**, 2347-2351.
12. A. B. Laursen, S. Kegnæs, S. Dahl and I. Chorkendorff, *Energy & Environmental Science*, 2012, **5**, 5577.
13. R. Kojima and K.-I. Aika, *Applied Catalysis A: General*, 2001, **219**, 141-147.
14. X. Hu, W. Zhang, X. Liu, Y. Mei and Y. Huang, *Chemical Society Reviews*, 2015, **44**, 2376-2404.
15. S. Alconchel, F. Sapiña, D. Beltrán and A. Beltrán, *Journal of Materials Chemistry*, 1998, **8**, 1901-1909.
16. Y. Ding, Y. Wan, Y.-L. Min, W. Zhang and S.-H. Yu, *Inorganic Chemistry*, 2008, **47**, 7813-7823.
17. D. S. Bem, C. M. Lampe-Önnerud, A. Hans P Olsen and H. C. Zur Loye, *Inorganic Chemistry*, 1996, **35**, 581-585.
18. D. S. Bem, H. P. Olsen and H. C. Zur Loye, *Chemistry of Materials*, 1995, **7**, 1824-1828.
19. M. Q. Yu, L. X. Jiang and H. G. Yang, *Chemical Communications*, 2015, **51**, 14361-14364.
20. R. N. Singh, Madhu, R. Awasthi and A. S. K. Sinha, *Electrochimica Acta*, 2009, **54**, 3020-3025.
21. R. N. Singh, Madhu, R. Awasthi and A. S. K. Sinha, *Journal Solid State Electrochemistry*, 2009, **13**, 1613-1619.

22. V. K. V. P. Srirapu, C. S. Sharma, R. Awasthi, R. N. Singh and A. S. K. Sinha, *Physical Chemistry Chemical Physics*, 2014, **16**, 7385-7393.
23. V. Srirapu, M. Kumar, R. Awasthi and R. N. Singh, *International Journal of ...*, 2013.
24. R. Singh, J. Singh and A. Singh, *International Journal of Hydrogen Energy*, 2008, **33**, 4260-4264.
25. K. Eda, Y. Uno, N. Nagai, N. Sotani and M. Stanley Whittingham, *Journal of Solid State Chemistry*, 2005, **178**, 2791-2797.
26. S. Ramanathan, C. C. Yu and S. T. Oyama, *Journal of Catalysis*, 1998, **173**, 10-16.
27. B. Cao, G. M. Veith, R. E. Diaz, J. Liu, E. A. Stach, R. R. Adzic and P. G. Khalifah, *Angew. Chem. Int. Ed.*, 2013, **52**, 10753-10757.
28. J. A. Cecilia, A. Infantes-Molina, E. Rodríguez-Castellón and A. Jiménez-López, *Applied Catalysis B: Environmental*, 2009, **92**, 100-113.
29. Y. Liu, C. Liu and G. Que, *Energy & Fuels*, 2002, **16**, 531-535.
30. I. K. Milad, K. J. Smith, P. C. Wong and K. a. R. Mitchell, *Catalysis Letters*, 1998, **52**, 113-119.
31. C. J. H. Jacobsen, S. Dahl, B. S. Clausen, S. Bahn, A. Ashildur Logadottir and J. K. Nørskov, *Journal of the American Chemical Society*, 2001, **123**, 8404-8405.
32. C. J. H. Jacobsen, *Chemical Communications*, 2000, **0**, 1057-1058.
33. J. Greeley, I. E. L. Stephens, A. S. Bondarenko, T. P. Johansson, H. A. Hansen, T. F. Jaramillo, J. Rossmeisl, I. Chorkendorff and J. K. Norskov, *Nature Chemistry*, 2009, **1**, 552-556.
34. J. Kibsgaard, C. Tsai, K. Chan, J. D. Benck, J. K. Nørskov, F. Abild-Pedersen and T. F. Jaramillo, *Energy & Environmental Science*, 2015, **8**, 3022-3029.
35. C. C. Yu, S. Ramanathan and S. T. Oyama, *Journal of Catalysis*, 1998, **173**, 1-9.
36. D. Friebel, M. W. Louie, M. Bajdich, K. E. Sanwald, Y. Cai, A. M. Wise, M.-J. Cheng, D. Sokaras, T.-C. Weng, R. Alonso-Mori, R. C. Davis, J. R. Bargar, J. K. Nørskov, A. Nilsson and A. T. Bell, *Journal of the American Chemical Society*, 2015, **137**, 1305-1313.
37. M. S. Burke, L. J. Enman, A. S. Batchellor, S. Zou and S. W. Boettcher, *Chemistry of Materials*, 2015, **27**, 7549-7558.
38. J. K. Norskov, J. Rossmeisl, A. Logadottir, L. Lindqvist, J. R. Kitchin and T. Bligaard, *Journal of Physical Chemistry B*, 2004, **108**, 17886-17892.
39. I. C. Man, H. Y. Su, F. Calle Vallejo, H. A. Hansen, J. I. Martinez, N. G. Inoglu, J. Kitchin, T. F. Jaramillo, J. K. Norskov and J. Rossmeisl, *ChemCatChem*, 2011, **3**, 1159-1165.
40. K. S. Weil, P. N. Kumta and J. Grins, *Journal of Solid State Chemistry*, 1999, **146**, 22-35.
41. Q. He and E. J. Cairns, *Journal of the Electrochemical Society*, 2015, **162**, F1504-F1539.
42. A. W. Sleight and B. L. Chamberland, *Inorganic Chemistry*, 1968, **7**, 1672-1675.
43. H. Ponceblanc, J. M. M. Millet, G. Coudurier, O. Legendre and J. C. Vedrine, *The Journal of Physical Chemistry*, 1992, **96**, 9462-9465.
44. J. A. Rodriguez, S. Chaturvedi, J. C. Hanson, A. Albornoz and J. L. Brito, *Journal of Physical Chemistry B*, 1998, **102**, 1347-1355.

45. J. N. L. Brito and A. L. Barbosa, *Journal of Catalysis*, 1997, **171**, 467-475.
46. J. Zou and G. L. Schrader, *Journal of Catalysis*, 1996, **161**, 667-686.
47. M.-C. Liu, L.-B. Kong, X.-J. Ma, C. Lu, X.-M. Li, Y.-C. Luo and L. Kang, *New J. Chem.*, 2012, **36**, 1713-1716.
48. S. Bhattacharyya, S. Kurian, S. M. Shivaprasad and N. S. Gajbhiye, *Journal of Nanoparticle Research*, 2009, **12**, 1107-1116.
49. J. Suntivich, H. A. Gasteiger, N. Yabuuchi and Y. Shao-Horn, *J Electrochem Soc*, 2010, **157**, B1263-B1268.
50. S. S. Kocha, Y. Garsany and D. Myers, NREL, March 12, 2013, 2013.
51. G. W. Smith and J. A. Ibers, *Acta Crystallographica*, 1965, **19**, 269-275.
52. Z. Yin, Y. Chen, Y. Zhao, C. Li, C. Zhu and X. Zhang, *Journal of Materials Chemistry A*, 2015, **3**, 22750-22758.
53. J. Zhang, R. Zhang, P. Song, J. Zhao, X. Guo, D. Zhang and B. Yuan, *RSC Advances*, 2015, **5**, 84451-84456.
54. R. N. Panda and N. S. Gajbhiye, *Journal of Alloys and Compounds*, 1997, **256**, 102-107.
55. B. Cao, J. C. Neuefeind, R. R. Adzic and P. G. Khalifah, *Inorganic Chemistry*, 2015, **54**, 2128-2136.
56. B. Cao, G. M. Veith, J. C. Neuefeind, R. R. Adzic and P. G. Khalifah, *Journal of the American Chemical Society*, 2013, **135**, 19186-19192.
57. R. N. Panda and N. S. Gajbhiye, *Journal of Crystal Growth*, 1998, **191**, 92-96.
58. U. A. Paulus, T. J. Schmidt and H. A. Gasteiger, *Journal of Electroanalytical Chemistry*, 2001, **495**, 134-145.
59. Y. Lee, J. Suntivich, K. J. May, E. E. Perry and Y. Shao-Horn, *The Journal of Physical Chemistry Letters*, 2012, **3**, 399-404.
60. S. Jung, C. C. L. Mccrory, I. M. Ferrer, J. C. Peters and T. F. Jaramillo, *Journal of Materials Chemistry A*, 2016, **4**, 3068-3076.
61. C. W. Cady, G. Gardner, Z. O. Maron, M. Retuerto, Y. B. Go, S. Segan, M. Greenblatt and G. C. Dismukes, *ACS Catalysis*, 2015, **5**, 3403-3410.
62. S. Trasatti and O. A. Petrii, *Journal of Electroanalytical Chemistry*, 1992, **327**, 353-376.
63. W. Xing, G. Yin and J. Zhang, *Rotating Electrode Methods and Oxygen Reduction Electrocatalysts*, Elsevier, Amsterdam, The Netherlands, 2014.
64. N. M. Markovic, H. A. Gasteiger and P. N. Ross, *Journal of Physical Chemistry*, 1995, **99**, 3411-3415.
65. K. Hada, A. Masatoshi Nagai and S. Omi, *The Journal of Physical Chemistry B*, 2001, **105**, 4084-4093.
66. K. Hada, J. Tanabe, S. Omi and M. Nagai, *Journal of Catalysis*, 2002, **207**, 10-22.
67. J. C. Dupin, D. Gonbeau and H. Benqlilou-Moudden, *Thin Solid Films*, 2001, **384**, 23-32.
68. R. Sanjinés, C. Wiemer, J. Almeida and F. Lévy, *Thin Solid Films*, 1996, **290-291**, 334-338.
69. S. Badrinarayanan, S. Sinha and A. B. Mandale, *Journal of Electron Spectroscopy and Related Phenomena*, 1989, **49**, 303-309.
70. S. H. Chang, J. G. Connell and N. Danilovic, *Faraday Discussions*, 2014, **176**, 125-133.

71. S. H. Chang, N. Danilovic, K.-C. Chang, R. Subbaraman, A. P. Paulikas, D. D. Fong, M. J. Highland, P. M. Baldo, V. Stamenkovic, J. W. Freeland, J. A. Eastman and N. M. Markovic, *Nature communications*, 2014, **5**, 4191.
72. A. Lasia, in *Modern Aspects of Electrochemistry*, 2004, vol. 32, pp. 143-248.
73. P. Ekdunge, K. Juttner, G. Kreysa, T. Kessler, M. Ebert and W. J. Lorenz, *J Electrochem Soc*, 1991, **138**, 2660-2668.
74. T. Kessler, J. R. Vilche, M. Ebert, K. Juttner and W. J. Lorenz, *Chemical engineering & technology*, 1991, **14**, 263-269.
75. M. E. G. Lyons and M. P. Brandon, *Journal of Electroanalytical Chemistry*, 2009, **631**, 62-70.
76. E. Meza, J. Ortiz, D. Ruíz-León, J. F. Marco and J. L. Gautier, *Materials Letters*, 2012, **70**, 189-192.
77. Q. Zhuang, J. Xu, X. Fan, G. Wei, Q. Dong, Y. Jiang, L. Huang and S. Sun, *Science in China Series B: Chemistry*, 2007, **50**, 776-783.
78. M. L. Tremblay, M. H. Martin, C. Lebouin, A. Lasia and D. Guay, *Electrochimica Acta*, 2010, **55**, 6283-6291.
79. G. Gardner, J. Al-Sharab, N. Danilovic, Y. B. Go, K. Ayers, M. Greenblatt and G. C. Dismukes, *Energy & Environmental Science*, 2016, **9**, 184-192.
80. M. Fayette, A. Nelson and R. D. Robinson, *Journal of Materials Chemistry A: Materials for energy and sustainability*, 2015, **3**, 4274-4283.
81. A. Grimaud, K. J. May, C. E. Carlton, Y.-L. Lee, M. Risch, W. T. Hong, J. Zhou and Y. Shao-Horn, *Nature communications*, 2013, **4**, 2439.
82. W. T. Hong, M. Risch, K. A. Stoerzinger, A. Grimaud, J. Suntivich and Y. Shao-Horn, *Energy & Environmental Science*, 2015, **8**, 1404-1427.
83. W. T. Hong, R. E. Welsch and Y. Shao-Horn, *The Journal of Physical Chemistry C*, 2016, **120**, 78-86.
84. J. Suntivich, W. T. Hong, Y.-L. Lee, J. M. Rondinelli, W. Yang, J. B. Goodenough, B. Dabrowski, J. W. Freeland and Y. Shao-Horn, *The Journal of Physical Chemistry C*, 2014, **118**, 1856-1863.
85. J. Suntivich, K. J. May, H. A. Gasteiger, J. B. Goodenough and Y. Shao-Horn, *Science*, 2011, **334**, 1383-1385.
86. F. M. F. De Groot, M. Grioni, J. C. Fuggle, J. Ghijsen, G. A. Sawatzky and H. Petersen, *Physical Review B*, 1989, **40**, 5715-5723.
87. F. M. F. De Groot, M. Abbate, J. Van Elp, G. A. Sawatzky, Y. J. Ma, C. T. Chen and F. Sette, *Journal of Physics: Condensed Matter*, 1993, **5**, 2277.
88. M. Ménétrier, I. Saadoune, S. Levasseur and C. Delmas, *Journal of Materials Chemistry*, 1999, **9**, 1135-1140.
89. S. Choi and A. Manthiram, *Journal of Solid State Chemistry*, 2002, **164**, 332-338.
90. H. Liu, Y. Zhou, R. Moré, R. Müller, T. Fox and G. R. Patzke, *ACS Catalysis*, 2015, **5**, 3791-3800.
91. M. Higashi, K. Domen and R. Abe, *Journal of the American Chemical Society*, 2012, **134**, 6968-6971.
92. K. Maeda, D. Lu and K. Domen, *Chemistry - A European Journal*, 2013, **19**, 4986-4991.